# Modeling the response of thin superconductors to applied magnetic fields and currents

by Guillem Via Rodríguez

under the supervision of

Dr. Carles Navau Ros and Dr. Àlvar Sánchez Moreno
Submitted to obtain the
PhD in Physics

Departament de Física
Universitat Autònoma de Barcelona

Bellaterra, September 2013

Superconductors are one the few systems that exhibit a quantum state extending over distances on the macroscopic scale. This makes them a very interesting topic of research due to the rich variety of phenomena arising from this fact; both from the physics fundamentals point of view and because of their potential for applications. Actually, special and extreme properties have often presented good performance for some particular functioning. In the case of superconductors, among these special properties are their large response under small external perturbations of different kinds and their high generated fields and transport currents with low energy losses. All of these properties have made superconductors useful for devices with very high sensitivity and control in different systems, as well as for the production and transport of energy with high efficiency.

Improving the performance of these materials for the above discussed aims requires a deep understanding of the underlying mechanisms allowing for such behavior. In many of these phenomena, superconducting vortices play an important role. In fact, they do so either by producing undesired effects or by giving useful measurable and/or tunable outputs. This is the reason why the conditions for the nucleation and dynamics of these entities has been a subject of extensive study for many decades. However, in spite of this effort there is still an important lack of knowledge on a wide variety of phenomena involving them.

When dealing with superconductors, sometimes it is very useful to make use of very thin samples. One of the main reasons for this is that some of their properties and responses are highly enhanced in this geometry. For this type of samples there are still many phenomena which are not well understood. Actually, even in the broadly employed London and critical-state theories (the ones we use here), the distribution of an externally fed transport current was not determined theoretically, until very recently, for other geometries than that of a straight strip of uniform width. Thus, only cases in which external magnetic fields are present were fully solved. Moreover, even for this magnetic field case, most of the former studies dealt only with single plates of different

geometries or sets of straight strips.

With the present work we aim at studying some of the still unsolved problems and at filling a few of these remaining gaps. To do so we extend the Magnetic Energy Minimization (MEM) model, used in previously published studies, to account for the applied transport current and other elements within the superconductor system. For example we systematically study the distribution of currents in thin strips of different non-straight geometries within both of the London and the critical-state models. As far as we know, this is the first time such a study for this more general case is done. In fact, we also include the simultaneous application of magnetic fields and transport currents in the samples.

The present thesis is organized as follows. First, in chapter 1 we introduce the superconducting materials, giving a quick overview of some of the most important historical advances on the topic. This is followed by a short review of some of the existing theories to explain their electromagnetic response. Then, we give a more detailed description of the particular distribution of magnetic fields and currents, for different sample geometries, within the London and critical-state approaches. We end the chapter by listing important applications that make use of the principles studied in the remaining part of the thesis.

In chapter 2 we present the theoretical model and numerical procedure we use to simulate the response of the superconducting samples. There we give a detailed description of the problem we seek to solve, as well as of the procedure we will use.

Chapter 3 deals with the first part of the results, where superconductors with different geometries are modeled within the London theory. Hence these results are only valid for low applied fields and currents. In particular we make a systematic study of the distribution of transport currents in different strip geometries involving sharp turns. Then we discuss the effect of these currents on the first nucleation and subsequent behavior of a penetrating vortex near a sharp $\pi$ 2 radiants turn. We end the chapter by studying the response of pairs of parallel non-coplanar plates under perpendicular applied magnetic fields.

The second part of the results is given in chapter 4. In this case the model used for the simulation of the superconducting samples is the critical-state model. Therefore, here the superconductor is assumed to be very hard. We begin the chapter by describing the general behavior of applied transport currents. In this case, this description is made both for situations in which just them are present and for those where a perpendicular external field is also applied simultaneously. We continue by showing some expected new phenomena coming from the highly hysteretic behavior of such currents, for example within a straight strip filled with some antidots. The chapter ends with the extension to the critical-state of the study of the same pair of parallel plates considered in the previous chapter.

We conclude the thesis in chapter 5 by summarizing some of the most significant discoveries and presented results. We also outline some of the possible future research lines to continue from the present work.

# Contents

Introduction

## 1.1 General concepts on superconductivity

The phenomena of superconductivity was first observed in 1911 by Kamerlingh Onnes [1]. He found that the electric resistance of mercury dropped suddenly to zero when it was cooled below a critical temperature $T_c$ of 4 15K. More superconducting metals and alloys with higher $T_c$ were found in the following years until the discovery of $Nb_3Ge$ ($T_c = 23K$) in 1973 [2]. This is the material with highest $T_c$ among the later known as low temperature superconductors (LTS), characterized by low values on their $T_c$. It took 13 more years to discover a new superconductor with a higher critical temperature. It was an oxide of lanthanum, barium and copper with $T_c = 35K$ [3], the first high temperature superconductor (HTS). Another important step in the history of superconductivity came from the discovery of the first superconductors with a $T_c$ above liquid nitrogen, which reduced significantly the cost of the involved cryogenics. These superconductors were among the cuprates, copper oxide compounds superconducting on their CuO planes. Worth to mention are the widely used cuprates $YBa_2Cu_3O_{7-\delta}$ (YBCO) [4] and $Bi_2Sr_2Ca_2Cu_3O_{10+\delta}$ (BSCCO), with $T_c \approx 90K$ and $T_c \approx 120K$, respectively, being the former more common for applications at present [5].

Apart from their zero resistivity, another property characterizing the behavior of superconductors is the complete exclusion and expulsion of the magnetic induction field **B** from their interior, i.e. **B** = 0, when they are cooled below $T_c$. This is the Meissner Ochsenfeld effect (1933) [6], named after its discoverers, that proved superconductivity to be a thermodynamical state. This effect was explained by the London theory (1935) [7], according to which fields and currents decay over a few distances $\lambda$, the London penetration depth, from the superconductor surface.

Superconductors also exhibit flux quantization, as Little and Parks proved experi-

mentally in 1962 [8]. That means the net magnetic flux across any area fully surrounded by superconducting material is a multiple of the fluxoid quanta $\Phi_0 = h\,2e$, with $h$ Planck s constant and $e$ the electron charge. The quantization was found to arise from the coherence in the quantum state of the Cooper pairs, the quasi-particles responsible for superconductivity. These Cooper pairs are bosonic quasi particles consisting of pairs of electrons coupled via phonon interactions. The theory behind this discovery was the microscopic theory by Bardeen, Cooper and Schrieffer (BCS) [9]. However, this theory cannot explain the coupling at the high temperatures involved in HTS, for which the interactions between electrons and phonons are still not well understood.

Another important advance in superconductivity came when Alexei Abrikosov in 1957 [10], found a particular solution of the Ginzburg-Landau (GL) equations. The GL theory was developed by Ginzburg and Landau in 1950 [11] to explain the phenomena taking place near thermodynamic phase transitions of second order. They used a complex function    , the order parameter, which is related to the Cooper pairs density. varies over distances on the order of the coherence length $\xi$. The solution by Abrikosov showed that in superconductors with $\kappa \equiv \lambda\,\xi > 1\quad\overline{2}$ magnetic flux penetrates into the material in the form of flux threads, vortices or fluxoids that distribute in its interior forming a triangular lattice.

The materials with $\kappa > 1\quad\overline{2}$ were called type-II superconductors to distinguish them from the type-I superconductors, with $\kappa < 1\quad\overline{2}$. In the latter, complete flux expulsion takes place in the Meissner state, when the magnetic induction $B$ is below some critical value $B_c$. These materials transit into the normal, non-superconducting, state above $B_c$.

Type-II superconductors present a richer variety of states. For $B$ below a lower critical induction $B_{c1}$, the complete flux expulsion is also present in these materials. However, above this value and below a second larger critical induction $B_{c2}$, i.e. $B_{c1} < B < B_{c2}$, the partial flux penetration happens. In this range of fields, the superconductor is in the mixed state. For $B > B_{c2}$ the vortices fill the whole superconductor and superconductivity vanishes.

## 1.2   Type-II superconductors

The flux vortices present in the mixed state consist of a normal state central core surrounded by circulating supercurrents. Each vortex carries a single flux quantum $\Phi_0$. Fluxoids are driven by a magnetic force in the presence of any other current.

The vortices are straight and aligned with the applied induction $\mathbf{B}$ when it is applied longitudinally to an infinitely long sample. In this case, the force on the vortex per unit length $L$ in the long direction is given by [12]

$$\mathbf{F}_d\,L = \mathbf{J} \times \mathbf{\Phi_0} \tag{1.1}$$

Here $\mathbf{J} = \quad\times\mathbf{H}$ is the local current density, $\mathbf{H}$ the magnetic field vector and $\mathbf{\Phi_0}$ is the vector of modulus $\Phi_0$ pointing in the direction of $\mathbf{B}$. As a result, vortices repel or

attract each other depending on their vorticity, which is defined from the direction of their field. Moreover, they are also pushed or pulled by flowing currents. According to the GL theory, the most stable structure of them, where repulsion forces compensate each other in the absence of transport currents and pinning centers, is a triangular lattice.

However, if defects are present, they often act as pinning centers for the fluxoids [13]. Thus, the vortices interact with them and do not move freely anymore. Then the lattice becomes distorted and the periodicity is broken. Depending on the temperature, the interaction with defects is different and different thermodynamical phases can arise [14]. For example, at large temperature the thermal energy can easily overcome the energy of interaction between different vortices and that between vortices and pinning centers. In this case the vortices are not fixed but can move, behaving as a vortex liquid. This is the thermally activated flux flow (TAFF) regime. At lower non-zero temperatures, defects pin the vortices but some depinning due to thermal activation still occurs. This is the effect known as flux creep. Apart from the lattice relaxation due to thermal energy, fluxoids can also tunnel between different pinning centers [15, 16], which is another cause of relaxation. For large pinning forces, when vortices are strongly trapped and cannot move due to thermal energy and the effect of tunneling can be neglected, the superconductor is said to be in the critical state [12]. The defects acting as pinning centers can be of many types [12, 13, 5, 17], from dislocations or twin boundaries in the matrix to normal and magnetic material inclusions, grain boundaries, or the non-conducting layers in HTS materials, among others.

Many different techniques have been used to visualize and extract information from the vortices and their behavior [18]. The first one, confirming Abrikosov s prediction, was the observation by Cribier *et al* [19] of a weak Bragg peak in small-angle neutron scattering (SANS) experiments in 1964. Just a few years later, in 1967, high-resolution pictures of the lattice were obtained by Essman and Trauble [20] from a decoration method using ferromagnetic crystallites that settled at the places where fluxoids emerged to the surface. Neutron depolarization [21] and muon spin rotation [22] were used to probe the 3D flux distribution inside the superconductor. Other techniques, allowing for the visualization of the lattice of fluxoids, are the scanning tunneling microscope (STM) [23, 24], with spatial resolution of single atoms, and the magnetic force microscope [25]. The motion and pinning of a single flux line in thin films was detected by measuring the diffraction pattern from a Josephson junction [26], and this motion also by its coupling to a 2D electron gas formed at the interface between Si and SiO [27]. Very useful methods giving single vortex resolution at the surface are the microscopic Hall probes [28], scanning electron microscopy [29], field-emission transmission electron microscopy [30] and magneto-optical imaging based on the Faraday effect [31, 32, 33], and with lower spatial resolution but more quantitatively, by scanning Hall probes [34].

Some of the above mentioned techniques proved many of the HTS materials to be layered and thus highly anisotropical, conducting only at some particular layers. The $c$ axis is defined as that normal to the conducting planes, called the *ab* planes [5].

Moreover, the HTS, characterized by a very short $\xi$, are strongly second type (Type-II) superconductors [35].

## 1.3    Modeling of type-II superconductors

The theory by Ginzburg and Landau, although strictly demonstrated only near $T_c$, is been proven very illustrative to understand some of the mechanisms leading the observed behavior of vortices in the whole range of $T < T_c$. According to this theory, the fields and order parameter function in the interior of the superconductor are those which minimize the net energy of the system accounting for three terms [36]: the gain in energy of forming the Cooper pairs, the kinetic energy from the flowing charge carriers, and the magnetic energy from present fields. The formation of a vortex involves a gain of energy from the reduction of $B$ outside it at the cost of sustaining the currents and suppressing the order parameter in its core.

Apart from the theory by Ginzburg and Landau, there are others from which the single or collective vortex structure and behavior have been modeled [18]. The triangular lattice, for example, was also derived from the BCS [37]. The London model, already mentioned above, is obtained as a limiting case of the GL model with $\xi \propto \lambda$ (or $\kappa \to 1$) but seems not to be restricted to temperatures close to $T_c$ [12]. This model, first derived to explain the Meissner effect in the Meissner state, i.e. below $B_{c1}$, was extended to account for a vortex core with $\xi = 0$ and describe how currents distribute in long [38, 39] and thin [40] samples. It is also used for the simulation of the interaction with an edge or surface and for deriving some of the barriers opposing to vortex penetration such as the Bean-Livingston [41] and the geometrical barriers [42]. In the case of intervortex spacings much larger than $\xi$ the solution for many vortices can be obtained from some theories from the linear superposition of those for a single vortex. At large inductions $B$, where the vortex density is high and their cores partially overlap, this approach does not give satisfactory results.

The origin of pinning can be understood from the GL theory. In order for the superconducting vortex core to form, the superconducting order parameter has to be suppressed there. However, since the order parameter does not need to be suppressed inside the defect, the vortex energy is lower there [43]. Thus, the vortex receives an attractive force from this defect. This effect allows for the understanding of pinning at some lattice defects and normal inclusions, but other effects play also a role in other types of defects. This is the case, for example, in magnetic inclusions, where both the field from the magnetic material and the exchange energy also lower the vortex energy [17, 44].

An early theory trying to simulate these effects on a macroscopic scale was a sponge-like model. This model was based on the idea of the remanence of flux inside the material after the removal of the external fields. A few years later, the theory that could explain many of the experiments on Type-II superconductors arrived based on the sponge-like model ideas. It was the critical-state model, presented by Bean in 1962 [45, 46],

describing the behavior of superconductors in the critical state, and hence assuming a strong vortex pinning.

The thermal effects of TAFF and flux creep can be simulated from the theory developed by Anderson [47]. According to this theory the relation $E(J) \equiv \mathbf{E}(J) \cdot \mathbf{J}$, between the electric field $\mathbf{E}$ and the parallel current density $\mathbf{J}$ of unitary vector $\mathbf{J}$, is given by a power law [14] inside of the material. With the power law exponent $n$ ranging from 1 to , different degrees of depinning by thermal excitations could be modeled, including the effects of TAFF and flux creep. In the limit $n$ vortices are strongly pinned and no thermal effects are present. In this case the critical state model is recovered.

In this thesis we restrict our discussion to the London and critical-state models to describe the behavior of type-II superconductors in the Meissner and the critical states, respectively. We will consider both the cases of externally applied magnetic fields (magnetic case) and electric currents (transport case) in both infinitely long and very thin samples, for the two theories.

### 1.3.1 Meissner state: the London model

The London model is based on the assumptions of free moving particles of charge $e^*$, mass $m^*$ and volume density $n_s$ and zero trapped flux far from the superconductor surface. The London equation, relating the magnetic induction $\mathbf{B}$ and the current density $\mathbf{J}$ inside the superconductor, reads [48]

$$\mathbf{B} = -\mu_0 \quad \times (\lambda^2 \mathbf{J}) \tag{1.2}$$

with

$$\mu_0 \lambda^2 = \frac{m^*}{n_s (e^*)^2} \tag{1.3}$$

being $\mu_0$ the vacuum permeability. Note that in an anisotropic and inhomogeneous material, the squared London penetration depth, $\lambda^2$, is a position dependent tensor. Since the superconducting particles are pairs of electrons $e^* = 2e$.

We must bear in mind that assuming a uniform $n_s$ is equivalent to consider $\xi \propto \lambda$ (see Sec. 1.1), and thus not accounting for the space variations of the order parameter.

**Long samples (parallel geometry)**

To illustrate some of the general trends derived from the solution to the London equations, we first consider the simple case of a homogeneous and isotropic superconductor with both infinite length and uniform cross section along the direction of applied field or at least one of the directions perpendicular to applied current. This is the case known as parallel geometry, which deals with long samples.

In particular, we consider the slab geometry. Its shape consists of a flat planar prism of width $W$ that extends to infinity in the two in-plane directions. The slab is

placed perpendicular to the $x$ axis at $x$   $[-W\ 2\ +W\ 2]$. In this case the problem is mathematically 1D.

First we consider the magnetic case, when an external uniform magnetic induction $\mathbf{B_a}$ is applied. If $\mathbf{B_a} = B_a\mathbf{z}$, thus applied along the vertical $z$ direction, the solution for the flux density $\mathbf{B}(x) = B_z(x)\mathbf{z}$ inside the slab is

$$B_z(x) = \frac{B_a \cosh\left(\frac{x}{\lambda}\right)}{\cosh\left(\frac{W}{2\lambda}\right)} \tag{1.4}$$

and $B_z(\ x\ \geq W\ 2) = B_a$ outside it. From Ampere law the current density is found to be

$$J_y(x) = -\frac{B_a \sinh\left(\frac{x}{\lambda}\right)}{\mu_0 \lambda \cosh\left(\frac{W}{2\lambda}\right)} \tag{1.5}$$

Then, for large $W\ \lambda$ the modulus of current also follows a close to exponential decay from its maximum value,

$$J_{max} = B_a\ \left[\mu_0 \lambda \cosh\left(\frac{W}{2\lambda}\right)\right] \tag{1.6}$$

at the sample surface. It flows in opposite directions by the two surface planes.

Under longitudinal applied current per unit height $I_a$, the transport case, similar current and field spatial dependences take place. However, in this case current flows in the same direction by both outer planes and magnetic field has opposite sign at the two slab halves. In particular, the magnetic induction outside the slab is $-\text{sgn}(x)\mu_0 I_a\ 2$, where the function sign, $\text{sgn}(x)$, is $-1$ for $x < 0$ and $+1$ for $x > 0$.

We must note that this state is reversible. That means the field and current distribution depend just on the present values of the applied quantities and not on the previous ones. Moreover, fields and currents are both linear on $B_a$ and $I_a$. Thus, the distribution for any combination of the two of them can be obtained from the linear superposition of the solutions with $I_a = 0$ and $B_a = 0$, respectively.

From the above solutions, we can observe that the limit $\lambda \propto W$ gives very large surface currents confined to very narrow layers close to the two outer planes. Then field and current are almost zero within the sample interior. In the opposite limit, $\lambda \to W$, currents are nearly constant across width in the transport case and close to linear in the magnetic case.

In the magnetic case currents decrease down to zero anywhere within the sample for increasing $\lambda\ W$, but in the transport case net current must always equal the applied one. In both cases the field in the exterior is independent on this ratio.

An infinite cylinder in an axial field would present the same behavior but there currents follow concentric circular paths.

The slab geometry considered above is a simply connected one. When the sample presents some holes, the magnetic fluxoid can be defined from the London theory. In

this case, for any surface $S$ whose contour $\partial S$ runs all along the interior of the super-conducting material

$$\Phi \equiv \int_S \mathbf{B} \cdot \mathbf{n} \mathrm{d}S + \mu_0 \lambda^2 \oint_{\partial S} \mathbf{J} \cdot \mathrm{d}\mathbf{l} = N_f \Phi_0 \tag{1.7}$$

The quantity on the left is the fluxoid, composed of the magnetic flux through $S$ plus $\mu_0 \lambda^2$ times the circulation of $\mathbf{J}$ along $\partial S$. This fluxoid is always a multiple of the quantum fluxoid $\Phi_0$ ($N_f \in \mathbb{Z}$) within any path $\partial S$ in the interior of the superconductor, also when it surrounds some holes.

In particular, when a sample presenting some hole is cooled in a zero external field, or zero field cooled (ZFC), $N_f = 0$. However, when field cooling (FC) the sample, a state with $N_f \neq 0$ is achieved. Since each superconducting vortex carries one quantum of fluxoid, any extra penetration of vortices from the outer edge will increase $N_f$ by one.

**Magnetization and susceptibility of long samples** In magnetic materials, one can define the volume average magnetization as the magnetic moment per unit volume from [49]

$$\mathbf{M} = \left(\frac{1}{V}\right) \frac{1}{2} \int_V \mathbf{R} \times \mathbf{J}(\mathbf{R}) \mathrm{d}^3 \mathbf{R} \tag{1.8}$$

where the integral is taken over the whole sample volume $V$ and $\mathbf{R} = x\mathbf{x} + y\mathbf{y} + z\mathbf{z}$ is the 3D vector position. In long samples under longitudinal applied field $\mathbf{H_a} = H_a \mathbf{z}$ along $z$, the only non-zero magnetization component, $M_z$, can also be obtained from the averaged local currents generated field $H_J = H_i - H_a$ [50], where $H_i$ is the total internal field. Samples presenting a linear magnetic response, as is the case of superconducting samples modeled within the London theory, show a magnetization with constant slope

$$\chi_0 \equiv -M_z / H_a \tag{1.9}$$

in increasing uniform field $H_a$. Here $\chi_0$ is the initial susceptibility, which takes the value $+1$ in the parallel geometry for the small $\lambda$ limit. Actually, this definition corresponds to the external susceptibility [49], which equals the internal susceptibility in long samples.

**Thick samples**

When the far top and bottom end planes of the slab geometry considered in the previous section are separated by a finite distance along the vertical direction, some trends change drastically. We will refer as thick samples to these samples of finite non-zero thickness in the direction of applied field and in the two directions perpendicular to applied current. The reason for this change is the appearance of demagnetizing effects, which enhance the response to applied fields and currents in the case of superconductors. More precisely, the current distribution is not uniform anymore at the lateral planes and currents flow within the entire outer surface, including the top and bottom ones. This distribution results from the need to shield the external and the self-fields.

The particular case of a thick infinitely long tape was solved by Brandt and Mikitik [51] both for zero (complete shielding limit) and finite $\lambda$ and in the magnetic and transport cases. This geometry consists of a prism of rectangular cross section and the field and current are applied along the vertical, perpendicular to axis, direction and along the longitudinal one, respectively. In this case they also found currents to decay from the surface within distances $\approx \lambda$, but not only from the lateral but also from the entire surface at the top and bottom end planes. In the magnetic case currents flow in opposite directions by the two tape halves and the zero current value is only met at the top and bottom surface central line. On the contrary, in the transport case currents penetrate symmetrically from the four outer planes. Moreover, a great enhancement of local field and current was observed at the tape corners, which was larger for lower $\lambda$, and diverged at $\lambda$   0.

**Thin samples (perpendicular geometry)**

Of special interest for applications are thin planar superconducting strips or platelets, in which the above mentioned demagnetizing effects are larger. In this case the behavior described below applies not only for isotropic materials but also for anisotropic ones whose anisotropy is along the out-of-plane direction. This is the case, for example, of HTS materials with the $c$ axis perpendicular to the thin film.

The flux distribution within thin plates of different cross section in the critical state has been observed by many authors both by magneto-optics [52, 53, 32] and Hall probes [28, 34, 54, 55, 56]. These measurements give validation to many of the results described below.

The case considered in this section is the one in which a uniform magnetic field is applied perpendicular to the thin sample or a transport current is applied longitudinal to it. We refer to this case as that of thin samples, also referred to as perpendicular geometry.

In this thin limit it is convenient to work with the thickness, $t$, averaged surface current density

$$\mathbf{K}(x \ y) = \int_{-t/2}^{+t/2} \mathbf{J}(x \ y \ z)\mathrm{d}z \qquad (1.10)$$

without caring on the particular vertical distribution of currents. Then, the dimensionality of the problem is reduced. When $t \leq \lambda$, $K$ decays in the in-plane directions over distances on the order of $\Lambda \equiv \lambda^2 \ t$, the Pearl length. This is the characteristic length for the decay of currents both from a sample edge and from a vortex core [40].

We first deal with the thin strip geometry. It can be thought as the limit of reducing the thickness $t$, of the slab or thick tape geometries considered above, while keeping the finite lateral dimension, the width $W$, constant. In particular the thin strip limit is met when $t \propto W$. This reduction leads to a high enhancement of fields and currents not only at the tape corners but all along the short lateral edges. Also currents and fields are non-zero within the whole top and bottom planes.
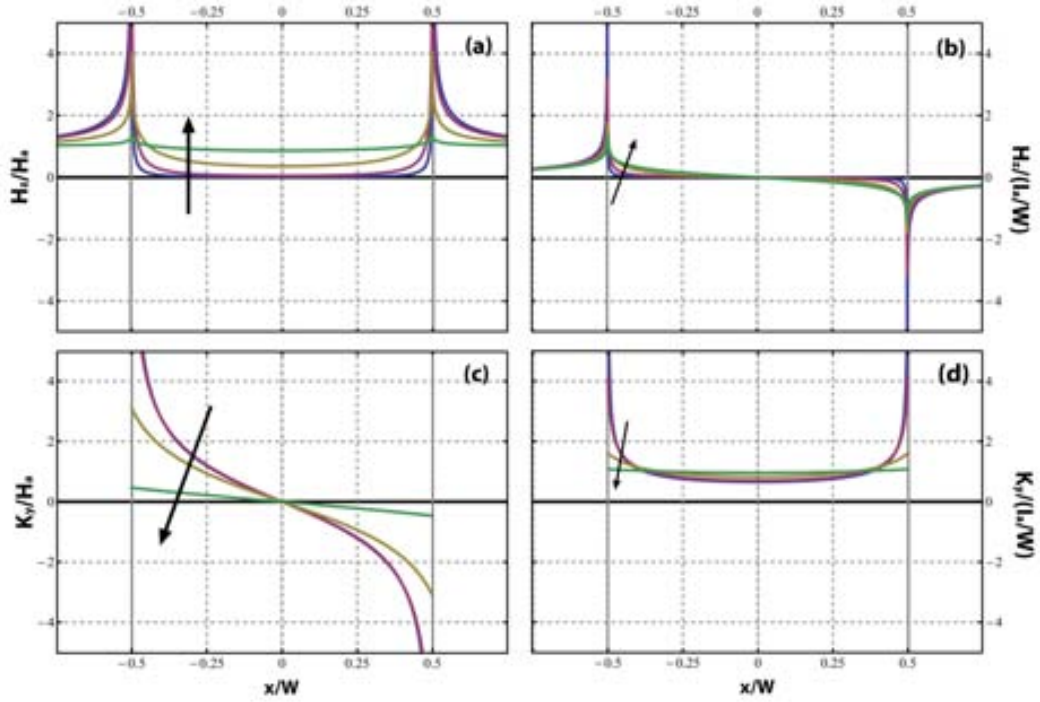
Figure 1.1: Out-of-plane magnetic field $H_z = B_z / \mu_0$ (upper row) and longitudinal sheet current $K_y$ (lower row) for an infinitely long (along $y$) thin planar straight strip of width $W$ and different two-dimensional screening length $\Lambda$ for the magnetic case, in which a uniform magnetic field $H_a = B_a / \mu_0$ is applied along the $z$, perpendicular-to-film, direction (left column) and the transport case of applied longitudinal transport current $I_a$ (right column). Shown are the cases for $\Lambda / W =$ 0.001, 0.01, 0.1 and 1 (increasing in the arrow direction). The field and sheet current components are normalized to $H_a$ in the magnetic case and to $I_a / W$ in the transport case.

The distribution of $\mathbf{K}$ was found for this geometry both under perpendicular $B_a$ and under a longitudinal $I_a$, analytically in the complete shielding limit [57, 58], where $\Lambda \propto W$, and numerically for arbitrary $\Lambda / W$ [59, 60].

In these cases $K$ was found to be different from zero anywhere within the whole strip surface for arbitrary $\Lambda / W$. Moreover, in the limit $\Lambda / W \propto 1$ currents diverge at the strip edges in order to be able to shield the self-field in the sample interior. These infinities, not present for non-zero $\Lambda / W$, are removed when considering a cutoff distance on the order of the smallest among $t$, $\lambda$ and $\Lambda$ from the edge.

The particular distributions obtained in the complete shielding limit for the sheet current and out-of-plane magnetic induction were [57, 58]

$$K_y(x) = -2\frac{B_a}{\mu_0} \frac{x}{\sqrt{(W/2)^2 - x^2}} \qquad x < W/2 \qquad (1.11)$$

$$B_z(x) = \frac{B_a \, x}{\sqrt{x^2 - (W/2)^2}} \qquad x > W/2 \qquad (1.12)$$

for the magnetic case and

$$K_y(x) = \frac{I_a}{\pi\sqrt{(W\ 2)^2 - x^2}} \qquad x\ < W\ 2 \tag{1.13}$$

$$B_z(x) = -\frac{\mu_0}{4\pi}\frac{2\mathrm{sgn}(x)I_a}{\sqrt{x^2 - (W\ 2)^2}} \qquad x\ > W\ 2 \tag{1.14}$$

for the transport case, and $B_z = 0$ for $x\ < W\ 2$ for both cases, where $x$ denotes the absolute value of $x$ regardless of its sign. Here the strip is aligned with the $y$ axis and the field is applied in the vertical $z$ direction. Then in both cases $K_x = 0$ due to the symmetry of the problem. The functions found from fitting the numerical results for finite $\Lambda$ are (see Fig. 1.1) [59, 60]

$$\begin{aligned} K_y(x) &= \frac{I_a}{2\gamma\sqrt{(W\ 2)^2 - x^2 + \delta\Lambda W}} - \\ &\quad - \frac{H_a y}{\sqrt{\alpha[(W\ 2)^2 - x^2] + \beta\Lambda W}} \end{aligned} \tag{1.15}$$

with the definitions $\alpha = 1\ 4 - 0\ 63\ (W\ \Lambda)^{0.5} + 1\ 2\ (W\ \Lambda)^{0.8}$, $\beta = 1\ (2\pi) + \Lambda\ W$, $\delta = 2\ \pi + 8\ 44\ (W\ \Lambda + 21\ 45)$, and $\gamma = \arcsin(1\ \sqrt{1 + 4\delta\Lambda\ W})$. The fields are calculated from these currents and from the Biot-Savart law. The dependence given by equation 1.15 is plotted for different $\Lambda\ W$ together with the limit $\Lambda \propto W$ (complete shielding limit) in figure 1.1. We note that in the narrow limit, where $\Lambda \to W$, this expression tends to

$$K_y(x) = \frac{I_a}{W}\ - \frac{H_a y}{\Lambda} \tag{1.16}$$

where the term coming from the applied magnetic field drops to zero as $\Lambda$ grows to infinity.

This result for the $\Lambda \propto W$ limit is valid for arbitrary $\lambda\ t$ [59]. However the currents distribution across thickness is strongly dependent on this parameter. In particular we find a similar dependence to that in the slab under transport current in section 1.3.1 [58]. Currents follow a close to exponential decay from the surface, which means currents are confined to a thin layer by the top and bottom surface planes in the $\lambda \propto t$ limit and almost uniform across $t$ for $\lambda \to t$.

Analytical expressions are also available for the thin disk [61] geometry in the complete shielding limit and for rings in the complete shielding [62] and narrow limits [63] subjected to perpendicular applied fields. Numerical results were also found and described for the finite $\Lambda$ cases of these geometries [64]. The trends are very similar to those described above for straight strips but currents follow circular paths concentric to the sample.

When the sample is thin and the definition given by 1.10 is used, the quantum fluxoid given by equation 1.7 takes the expression

$$\Phi \equiv \int_S \mathbf{B} \cdot \mathbf{n}\mathrm{d}S + \mu_0\Lambda \oint_{\partial S} \mathbf{K} \cdot \mathrm{d}\mathbf{l} = N_f \Phi_0 \tag{1.17}$$

where $S$ runs in the interior of the superconductor and $S$ may contain holes or vortices. In this case the discussion for the long holed superconductor made in section 1.3.1 also applies and the ZFC and FC conditions lead to the same behavior. Here vortices and antivortices may enter or leave both from the outer or hole edges. For $\Lambda$ much smaller than the sample shortest in-plane dimension $a$, $\Lambda \propto a$, the fluxoid equals the magnetic flux through the area $S$.

It is instructive to mention the solution for the case of a stack of infinite parallel strips arranged periodically along the perpendicular to film direction [65]. Then each strip partially shields the external field at the neighbor ones surface. This partial shielding makes currents and magnetization to be lower when many strips are present and lower for smaller distances between them. Interestingly, this leads the sharp peaks at the edges of the strip to decrease with decreasing distance and to tend smoothly to the distribution of the infinite slab, where the demagnetizing effects disappear. The opposite happens when the strips are in the same plane [65, 66, 67], where each strip enhances the field at other strips regions and currents and magnetization are increased due to their presence.

**Thin planar samples of finite surface**

The currents and fields induced within other single thin planar samples of finite surface were also determined within this theory. In this case the problem becomes mathematically 2D, and the direction of current flow cannot be known a priori. Some examples are the square and rectangular [68], and the washer SQUID [69] geometries, which have been extensively studied. This was possible following the approach by Brandt [69] of making use of the sheet scalar function $g(x\ y)$, defined from the 2D thickness-averaged sheet current $\mathbf{K}(x\ y)$. This definition is given by the relation

$$\mathbf{K}(\mathbf{r}) = \quad \times (g(\mathbf{r})\mathbf{z}) = -\mathbf{z} \times \quad g(\mathbf{r}) \tag{1.18}$$

with $\mathbf{r}$ the in-plane vector position and $\mathbf{z}$ the vertical unit vector along $z$, perpendicular to the sample plane. The use of a real smooth scalar function $g(\mathbf{r})$ ensures the fulfillment of the continuity equation $\quad \cdot \mathbf{K}(\mathbf{r}) = 0$. The $g(\mathbf{r})$ distribution was obtained only for the applied magnetic field case while an applied transport current for thin 2D geometries was only considered for straight strips [65, 66, 70] and for other geometries in the complete shielding [71] and narrow [72, 73, 74] limits.

When considering samples of finite surface some new trends arise. Worth to mention are the currents enhancement near concave corners (lower than $\pi$), and its reduction near convex ones (larger than $\pi$). This effect, which is observed for arbitrary radius of curvature $\rho_c$, arises from the need of currents to follow the edges and to shield the sample surface from $B_z$. Reducing the minimum $\rho_c$ at the corner the effect becomes more pronounced, leading to infinite and zero current in a concave and a convex corner, respectively, in the limit $\rho_c \quad 0$ (sharp corner) and for arbitrary $\Lambda$. Moreover currents were observed to follow the straight edges along them and tend gradually to be circular as the distance from them increases. These trends make the straight edges better

candidates for the vortex nucleation than convex corners. Differently, the nucleation is expected at concave corners rather than at straight edges. Actually, the reduction of the field and current of first penetration at damaged edges may be related to this effect.

In the transport case, Clem and Berggren [73] showed that even in the narrow limit $(\Lambda \rightarrow W)$ currents accumulate at concave corners and diverge when the corner is sharp.

**Magnetization and susceptibility of thin samples**    In the perpendicular geometry under applied field $\mathbf{H_a} = H_a \mathbf{z}$ along $z$, we can make use of the definition given by equation 1.10. Then the magnetization definition in equation 1.8 can be written as

$$\mathbf{M} = M_z \mathbf{z} = \left( \frac{1}{tS} \right) \frac{1}{2} \int_S \mathbf{r} \times \mathbf{K}(\mathbf{r}) \mathrm{d}S \tag{1.19}$$

The external susceptibility $\chi_0$ can be defined from this out-of-plane magnetization and from expression 1.9.

Since $\chi_0$ depends on the demagnetization effects, in this geometry it is very different from the internal susceptibility. Different from what is observed in the parallel geometry, here $\chi_0$ depends on the shape of the perpendicular to field cross section. The large enhancement of this quantity due to the geometry is made clear from the obtained relation $\chi_0 \quad a \ t$ [75].

The particular external susceptibilities were found either analytically or numerically for different thin geometries. Worth to mention are the cases of an infinitely long thin straight strip of width $W$, a thin circular disk of radius $R$ and a square plate of side $a$, for which $\chi_0 = \pi W \ t \ 8R \ 3\pi t$ and $\approx 0 \ 4547a \ t$, respectively [61, 57, 58, 76, 77, 75].

### 1.3.2   Critical state: the critical-state model

This phenomenological model, dealing only with macroscopically averaged quantities, describes very well many of the experiments on hard superconductors in the mixed state. Hard superconductors are the ones exhibiting a wide magnetization curve under cycling applied fields, which results from strong pinning forces within the material. The critical-state model is based on the assumption that [45, 46] *any electromotive force, whatever small, will induce a macroscopic constant current, $J_c$.* Behind this sentence is the assumption that, wherever local current exceeds $J_c$, the vortex distribution will relax, thus decreasing $\mathbf{J}$ until the value $J_c$ is reached [12]. Then, the net magnetic force acting on vortices (see Eq. 1.1), be it from the repulsion or attraction of other vortices or from the driving force exerted by flowing currents, is exactly compensated by the pinning force from the defects. Thus, the critical-state model only describes the equilibrium metastable states where vortices are fixed and not the phenomena taking place during their movement. A further requirement for the critical state to be able to describe these states is that the external magnitudes are varied slowly enough so that these equilibrium states are achieved, i.e. steady-state situations are assumed.

The critical-state model applies only to high-$\kappa$ type-II superconductors in applied and self-fields much larger than $H_{c1} = B_{c1} \ \mu_0$. In this case, the assumption $\mathbf{B} \approx \mu_0 \mathbf{H}$

can be made for the magnetic induction $\mathbf{B}$ and field $\mathbf{H}$ [57, 58]. Another effect observed in type-II superconductors is that the maximum pinning forces that the pinning centers can stand depends on the local flux density. This can be included by the use of an induction dependent critical current density $J_c(B)$ [78, 79, 80, 81, 82, 83], but will be assumed uniform in the present work. Moreover, this model neglects the effects of all type of surface barriers (Bean-Livingston [41] and geometrical barriers [42]), as well as the thermal effects that lead to depinning (see Sec. 1.3). Since intervortex spacings are always assumed much shorter than the sample dimensions $a$, in the critical-state model $a \to \lambda$ is normally met. Extensions to the critical-state model accounting for some of these effects have also been made [84, 85, 86].

In opposition to the London model, the critical-state theory is strongly nonlinear. Actually, it is also hysteretic, and thus information about previously acquired states is necessary in order to determine the present one. Because of this, first one must set which is the state from which to start. In the particular case of a ZFC case the sample is initially in the virgin state, i.e. no field nor current is present anywhere within its interior and there are no externally applied ones.

**Long samples (parallel geometry)**

In the parallel geometry, the fields and currents described within the critical state model can be understood as those coming from the vortex density and their gradient distribution [12], respectively, both averaged over a few intervortex spacings. We consider as an example the case of an infinite slab with the same dimensions and position as in section 1.3.1. Then, if a magnetic field is applied in the vertical $z$ direction or a transport current is applied in the longitudinal $y$ direction, we have

$$B(x) = n(x)\Phi_0 \tag{1.20}$$

$$\mathbf{J}(x) = J_y(x)\mathbf{y} = \quad \times \mathbf{B}(x) = -\frac{\mathrm{d}B_z(x)}{\mathrm{d}x}\mathbf{y} \tag{1.21}$$

where $n(x)$ is the local number of fluxoids per unit area normal to the field direction or longitudinal to that of current, and $\Phi_0$ is the quantum fluxoid.

In the longitudinal slab geometry and for the ZFC case, both the application of a longitudinal uniform magnetic induction $B_a$ or transport current per unit height $I_a$ lead to the penetration of critical regions, where critical currents of modulus $J_c$ flow (see Fig. 1.2) [75]. The critical regions enter the sample from its two lateral plane surfaces at $x = \pm W\ 2$. There, magnetic induction decays linearly from the surface and takes the value zero at their inner boundary. In the sample innermost region between these two filled with critical current, $B = 0$ and $J = 0$. The difference between the magnetic and transport cases is that currents flow in opposite directions by the two outer planes of the slab in the first case while they do in the same one in the second case. This behavior

is given by the equations [45, 46]

$$J_y(x) = \begin{cases} -\text{sgn}(x)J_c & a_{mag} \le x \le W/2 \\ 0 & x < a_{mag} \end{cases} \tag{1.22}$$

$$B_z(x) = \begin{cases} 0 & x < a_{mag} \\ \mu_0(x - a_{mag})J_c & a_{mag} \le x < W/2 \\ B_a & x \ge W/2 \end{cases} \tag{1.23}$$

in the magnetic case, and by

$$J_y(x) = \begin{cases} J_c & a_{tr} \le x \le W/2 \\ 0 & x < a_{tr} \end{cases} \tag{1.24}$$

$$B_z(x) = \begin{cases} 0 & x < a_{tr} \\ -\mu_0(x - \text{sgn}(x)a_{tr})J_c & a_{tr} \le x < W/2 \\ -\text{sgn}(x)\mu_0 I_a/2 & x > W/2 \end{cases} \tag{1.25}$$

in the transport one. Here $a_{mag} = W/2(1 - B_a/B_s)$ is the half-width of the inner flux free region under applied $B_a$ and $a_{tr} = W/2(1 - I_a/I_c)$ that under longitudinal $I_a$, being

$$B_s = \mu_0 W J_c \tag{1.26}$$

and

$$I_c \equiv W J_c \tag{1.27}$$

the applied induction and current of full saturation, respectively. When $B_a = B_s$ is reached the whole sample is saturated with critical currents $J_c$ and there is no room for new currents. Any further increase of $B_a$ cannot be shielded and $B$ will penetrate the entire sample. However, if $I_a$ is increased above that of full saturation, $I_c$, this will cause the vortices to get depinned and move. Then the critical state conditions are not fulfilled and the model cannot be applied anymore.

Reversing the applied field or current will lead to the penetration of critical regions with currents flowing in the opposite direction from the two slab outer planes. There the $B_z$ slope is inverted. In the inner region, where these new currents have not penetrated yet, field and current remain frozen to those attained at the maximum applied $B_a$ or $I_a$ before the reversal started.

The particular cases of $B_a = 0$ and $I_a = 0$ in the reversal curve, known as the remanent states, show how some flux remains trapped into the sample after the removal of the applied magnitudes. We can see from this effect the importance of knowing which was the flux distribution before the application of any of them.

If the field and current are increased simultaneously to the sample in the virgin state the penetration is not symmetric with respect to the slab central plane. In particular
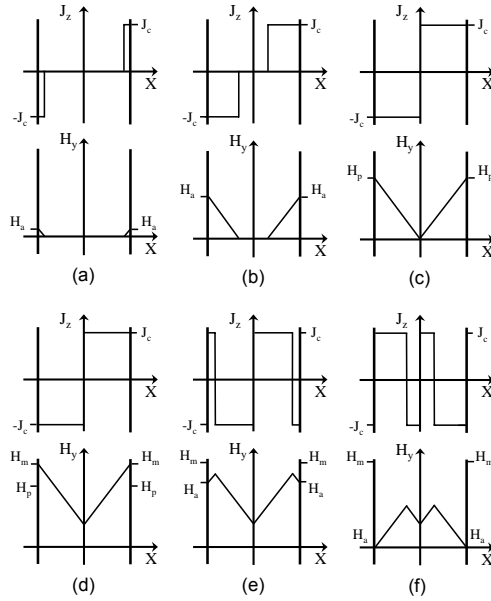
Figure 1.2: Sketch of current (top rows) and field (bottom rows) in an infinite slab, within the critical-state model, for different increasing longitudinally applied magnetic field $H_a$ in the initial curve (a-c) and then decreasing $H_a$ back to zero in the reversal curve (d-f).

the flux front will penetrate deeper where transport and magnetic currents flow in the same direction. Moreover, currents flowing by the opposite lateral planes, can flow in the same direction or in the opposite one depending on the ratio $B_a$ $I_a$.

We have just considered a few cases of applied magnetic field and/or transport current among a rich variety of different sequences of combinations of the two of them. However, in all the cases the profiles can be determined from the same simple ideas: when the varying external magnitude (field, current, or both) or its sign of variation change, currents of constant density $J_c$ either penetrate deeper from the sample surface with the same direction or start penetrating from the outer plane with the opposite one. The former situation takes place where the new variation induces currents of the same direction as that in the previous stage. The latter where they induce currents with opposite direction of flow. Flux and current remain frozen where newly induced currents have not penetrated yet.

When an infinitely long cylinder of radius $R$ is subjected to a uniform magnetic field $B_a$ applied in the axial direction, the behavior of fields and currents is very similar to that of the slab. The difference is that the penetrated region is a cylindrical shell entering from the surface and growing inwards to fill the whole cylinder at $B_a = \mu_0 J_c R$.

Thus, the currents follow circular paths concentric to the sample.

Other infinite geometries in longitudinal applied field can be solved using the above assumptions. This is the case in samples with cross section uniform along the infinite direction whose planes are all tangent to a cylinder. In this case it is only necessary to realize that currents flow parallel to the closest edge [87, 88].

These examples considered the ZFC case. In the FC case [89], the behavior can be easily derived from the above discussion and from the fact that only variations of $B_a$, and not its absolute value, lead to the penetration of new currents $J_c$. Then, in general we can speak of an inner flux frozen region, and not necessarily flux free.

**Magnetization and ac susceptibility of long samples**  The magnetization in long samples can be obtained from equation 1.8 or from the averaged local currents-generated field (see Sec. 1.3.1). In the critical state, superconductors present a highly nonlinear magnetic response and thus magnetization curve. As noted by Gilchrist [90], in this case the curve is very nearly independent on the sample cross section under the normalization $M_z(H_a \ H_s) \ M_s$, where $M_s$ is its saturation value and $H_s = M_s \ \chi_0$ is a field of significant penetration, being $\chi_0$ the low-field-limit susceptibility. This $\chi_0$ coincides with the Meissner complete shielding one for the same geometry. The reversal and return magnetization curves can be obtained from the initial one, by the relations [75]

$$M_{rev}(H_a) = M_{ini}(H_m) - 2M_{ini}\left[(H_m - H_a) \ 2\right] \tag{1.28}$$

and

$$M_{ret}(H_a) = -M_{rev}(-H_a) \tag{1.29}$$

where $H_m$ is the maximum applied field.

In this case of nonlinear response the real and imaginary ac susceptibilities are defined by [91]

$$\chi_n = \frac{}{\pi H_m} \int_0^T M_z(\tau) \cos(n \ \tau)\mathrm{d}t \tag{1.30}$$

and

$$\chi_n = \frac{}{\pi H_m} \int_0^T M_z(\tau) \sin(n \ \tau)\mathrm{d}\tau \tag{1.31}$$

respectively, when a $H_a(\tau) = H_m \cos( \ \tau)$ is assumed for the applied perpendicular field. Here $\tau$ is the time variable and $T$ and $\equiv 2\pi \ T$ the period and the angular frequency of the $H_a(t)$ function, respectively. Often it is only studied the response at fundamental frequency ($n = 1$). The quantities $\chi_1 \equiv \chi$ and $\chi_1 \equiv \chi$ [92] are nearly constant for low $H_m$ and close to $-\chi_0$ and 0, respectively. When increasing $H_m$ the absolute value of $\chi$ smoothly and monotonically decays to 0, following a close to $H_m^{-3/2}$ dependence at large $H_m$. Differently, $\chi$ first grows as $H_m$, at low fields, to reach a maximum value $\chi_m$ at some $H_m \approx H_s$ and decay back to zero as $H_m^{-1}$ at larger fields. These general trends and the particular dependences of their decay are general for all geometries of any thickness and cross section.

**Thick samples**

When the superconducting sample is thick, as is the case of the thick tape considered in the previous section, the demagnetizing effects lead to a significant enhancement of local fields and currents. One of the effects of this enhancement is the reduction of the applied field or current of first vortex nucleation. That makes the exact conditions for the vortex entry hard to be determined. In particular the geometric and edge barriers make it difficult to properly describe the interaction between the vortex and the sample edges [41, 40, 42, 59, 60]. These effects are neglected here, where we assume the first vortices to nucleate at $B_a \sim 0$.

In samples of finite thickness, the relation

$$\mathbf{J}(\mathbf{r}) = \nabla \times \mathbf{B}(\mathbf{r}) = (\nabla \times B(\mathbf{r}))\mathbf{B}(\mathbf{r}) + (\nabla \times \mathbf{B}(\mathbf{r}))B(\mathbf{r}) \qquad (1.32)$$

with $\mathbf{B}(\mathbf{r}) = B(\mathbf{r})\mathbf{B}(\mathbf{r})$, must substitute equation 1.20. Then current arises not only from the vortex gradient but also from its curvature.

Under these assumptions Brandt [93] determined the field and current distribution in a thick tape as the one considered in section 1.3.1 when a uniform perpendicular field is applied in the $z$ direction. In that case, some trends were observed to be identical to these for an infinitely long slab. However, the flux front was observed to penetrate all along the top and bottom end planes of the sample. In the magnetic case, under increasing applied field to the ZFC sample, the flux front penetrates deeper along the corner bisectors and from the lateral edges. Actually, the central flux-free core, elongated along the applied field direction, reaches the top and bottom end planes of the tape at their longitudinal central line. This is observed for all $H_a$ below some characteristic value $H_t$. Under increasing field above $H_t$, this core keeps shrinking both in the vertical and horizontal directions until, at $H_a = H_p$, the sample gets completely filled with currents. The field of full saturation $H_p$ equals the one generated by the uniform currents $J_c$ at the tape longitudinal central line. For decreasing the ratio of height $t$ to width $W$, $t W$, both $H_t$ and $H_p$ increase monotonically and diverge in the $t W$ 0 limit.

Similar behavior is found for the transport case although in this case currents penetrate symmetrically from the four outer planes [94, 95, 96, 97]. Therefore, even for very small applied $I_a \sim 0$ the flux front does not reach the tape external surface as in the magnetic case. The penetration is always deeper from the tape corners and along the cross section diagonals. At applied current $I_a = J_c tW$, the sample gets fully saturated for all $t W$.

Again the FC case can be easily derived from this discussion just by taking into account that the sample in this state reacts to the variations of applied field and current and not to their absolute values.

Also solved where the 2D thick geometries of single tapes with uniform elliptical cross section [98] and arrays of tapes of uniform rectangular cross section, under perpendicular field and longitudinal transport current [49], and only under axially applied magnetic field these for thick disks or cylinders [99, 100, 101] and rings or hollow cylinders [101].

In the case of rings, disks or cylinders the behavior is similar to that of a thick tape but currents follow concentric paths along the azimuthal direction. Worth to mention is that the flux front penetrates from all the surfaces, which includes the inner ones from finite rings and hollow cylinders.

**Thin samples (perpendicular geometry)**

Within the critical state model thin samples with $t\ W\ \ \ \ 0$ as these considered in section 1.3.1 can be dealt with in terms of the thickness-averaged sheet current **K** defined in equation 1.10.

In this case, the exact distribution across $t$ cannot be known but some trends can be grasped from the above discussion when the limit $t \to \lambda$ is met. According to Brandt [58], for the opposite limit, where $\lambda \leq t$, the behavior is rather different. In that case vortices cannot curve within the sample thickness and their cores remain straight and perpendicular to the strip plane. These are the so called Pearl vortices [40], whose currents extend to few $\Lambda \equiv \lambda^2\ t$ distances from the core. The $\Lambda$ can be much larger than $\lambda$ in very thin samples.

Here we deal with the quantity **K** defined in equation 1.10. Therefore, we do not care about the distribution of fields nor currents along the sample thickness. By following this approach an arbitrary value for $\lambda\ t$ can be considered as soon as $W \to \Lambda$ and $W \to t$ are assumed. Thus, the behavior we describe here applies to both the cases of curved Abrikosov vortices ($\lambda > t$) and straight Pearl vortices ($\lambda \leq t$).

When the sample is ZFC the distribution of sheet current and out-of-plane magnetic induction is obtained from assuming that two differentiated regions appear. An inner flux-free one, hence with $B_z = 0$, but with sub critical $\mathbf{K}\ < K_c = J_c t$ and an outer flux-penetrated one with $\mathbf{K(r)}\ = K_c$. When $t \to \lambda$, they can be understood as the one where vortices have not penetrated yet all along the thickness and the one where they have, respectively. However, if $t \leq \lambda$ the first one is filled with Meissner shielding currents while the second one is where Pearl vortices are present. The general equation 1.32 is still fulfilled in this case but the first term becomes comparatively much smaller and current comes solely from a strong flux-line curvature. Actually, as proposed by Zeldov *et al* [57] it is more convenient to think of it as arising from the discontinuity in the tangential **B** across the sample surface.

For the strip placed perpendicular to the $z$-axis and along the $y$-axis, these distributions are given by [57, 58]

$$K_y(x) = \begin{cases} -\frac{2K_c}{\pi} \arctan\left( \frac{2x}{W} \sqrt{\frac{(W/2)^2 - a_{mag}^2}{a_{mag}^2 - x^2}} \right) & x\ < a_{mag} \\ -\mathrm{sgn}(x) K_c & a_{mag} \leq\ x\ < W\ 2 \end{cases} \tag{1.33}$$

$$B_z(x) = \begin{cases} 0 & x\ < a_{mag} \\ B_f \ln \frac{x\ \ \overline{(W/2)^2 - a_{mag}^2} + (W/2)\ \ \overline{x^2 - a_{mag}^2}}{a_{mag}\ \ \ x^2 - (W/2)^2} & a_{mag} \leq\ x \end{cases} \tag{1.34}$$
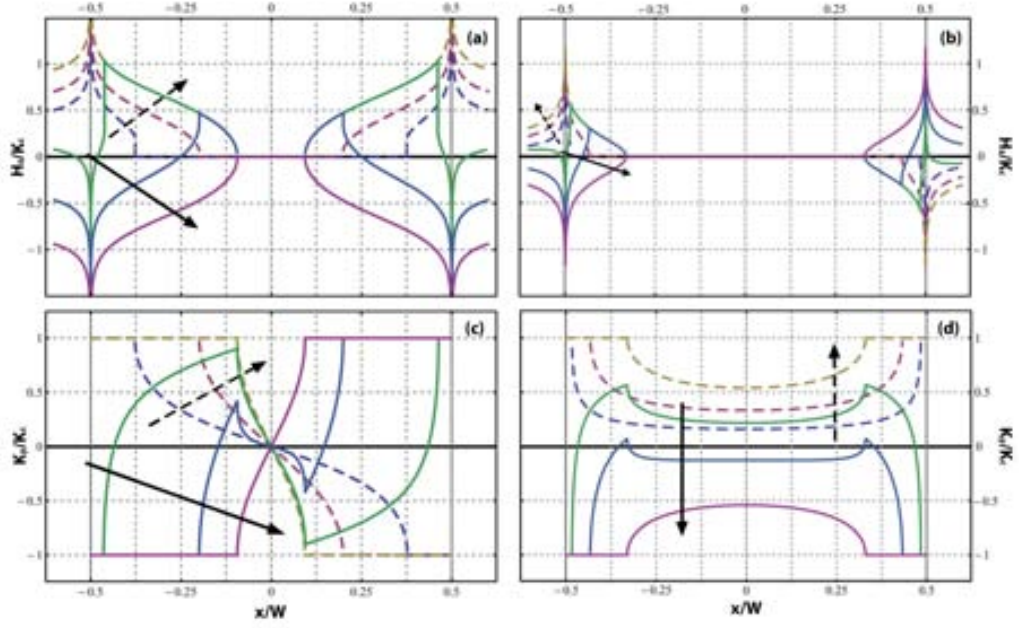
Figure 1.3: Out-of-plane magnetic induction $H_z = B_z \ \mu_0$ (upper row) and longitudinal sheet current $K_y$ (lower row), normalized to $K_c = J_c t$, for an infinitely long (along $y$) thin planar straight strip, of width $W$, critical current density $J_c$ and thickness $t$, in the critical state. Shown are the magnetic case, of perpendicular (along $z$) applied magnetic field $H_a = B_a \ \mu_0$ (left column) for $H_a \ K_c = 0\ 25$ $0\ 50$ and $0\ 75$ (increasing in the arrow direction), in the initial curve (dashed lines), and for $H_a \ K_c = +0\ 25$ $-0\ 25$ and $-0\ 75$ (decreasing in the arrow direction), in the reversal curve (solid lines). The curves for the same values for $I_a \ K_c W$ are plotted for the transport case. In the reversal curve, we note that $H_z$ is frozen where currents $K_y < K_c$.

for the case of applied uniform perpendicular field $B_a$ (see Figs. 1.3a and 1.3c) and

$$
K_y(x) = \begin{cases} \frac{2K_c}{\pi} \arctan\left(\sqrt{\frac{(W/2)^2 - a_{tr}^2}{a_{tr}^2 - x^2}}\right) & x < a_{tr} \\ K_c & a_{tr} \leq x < W\ 2 \end{cases}
\tag{1.35}
$$

$$
B_z(x) = \begin{cases} 0 & x < a_{tr} \\ -\mathrm{sgn}(x) B_f \ln \frac{\overline{(W/2)^2 - x^2}}{(W/2)^2 - a_{tr}^2 - \ \ x^2 - a_{tr}^2} & a_{tr} \leq x \end{cases}
\tag{1.36}
$$

for that of applied longitudinal current $I_a$ (see Figs. 1.3b and 1.3d). Here the half-width of the central flux-free region $a_{mag}$ and $a_{tr}$ for the magnetic and transport cases are, respectively,

$$
a_{mag} = \frac{W\ 2}{\cosh\left(B_a \ B_f\right)}
\tag{1.37}
$$

and

$$
a_{tr} = (W\ 2)\sqrt{1 - (I_a \ I_c)^2}
\tag{1.38}
$$

where $B_f = \frac{\mu_0}{\pi} K_c$ is a field of significant penetration and $I_c = K_c W$ is the full saturation current. These field and current distributions are shown in figure 1.3 for different values of applied field and currents. We observe the behavior is very different from that in long slabs. Here also a flux-penetrated region with critical current $K(\mathbf{r}) = K_c$ penetrates from the two lateral edges and grows inwards as the applied field or current is increased. Note that the central region remains flux free but not current free, as in the slab geometry, for the reasons described above.

The other difference is that $B_z(z = 0)$ is does not decay linearly in the flux-penetrated region but diverges at the sample edges and decays rapidly to reach the zero value, with vertical slope, at the inner boundary of this region. Moreover, demagnetizing effects make the field not to be equal to the applied one anywhere outside the sample but to decay monotonically to that value with increasing distance from the edges. The infinities in the edge field and the flux front field slope disappear when introducing a cut-off within distances on the order of the shortest among $t$, $\lambda$ and $\Lambda$. Then the peaks at the strip edges get rounded off and the slope becomes linear as in the slab case. Also the diverging $H_p$ becomes finite when the same cut-off distance is introduced for the width of the inner flux-free region. While in the slab all the transport current flows in the critical region, in the thin strip a large portion is usually carried by the flux-free region. This effect can be observed from the slow approach of this region width $a_{tr}$, to $W$ 2, with increasing $I_a$ (see Eq. 1.38).

Reversing the applied field or current induces the penetration of new currents of opposite direction but the same space dependence as the initial ones. These new currents, now with a new $K_c = 2K_c$ with respect to the already present ones, must be superposed to them. The result is the penetration of new critical regions of currents flowing in the opposite direction from either of the two sides. Currents are subcritical within the remaining strip width, thus changing anywhere within the sample and only flux remains frozen at the inner region.

Just like in the cases of thick and long samples, also in thin samples the FC case can be considered by assuming that the inner region remains flux frozen and often not flux free. This is because penetrating currents are induced by the variations of $B_a$ and not by its absolute value. Moreover, as far as we know the FC case has not been considered when $t \leq \lambda$, where the Meissner currents must be accounted for in the subcritical region.

Mawatari [65] also gave the solutions for the case of an infinite stack of thin straight strips arranged periodically along the vertical, perpendicular to film, direction. There he considered both the cases of applied perpendicular field and longitudinal current. He found the infinities at the edges and the vertical slope at the flux front to decrease with decreasing distance between the strips. In the limit of very short distances demagnetization effects disappear and the slab solution is recovered.

**Thin planar samples of finite surface**

Analogous behavior to that for the straight strip was found analytically for thin disks under perpendicular applied field [61], but in this case currents followed circular paths concentric to the sample. Other geometries were already solved in this regime numerically, like square, rectangular [76, 102] and cross shaped [68] thin plates in a perpendicular field, and the inclusion of linear or circular holes in the strip [103, 104].
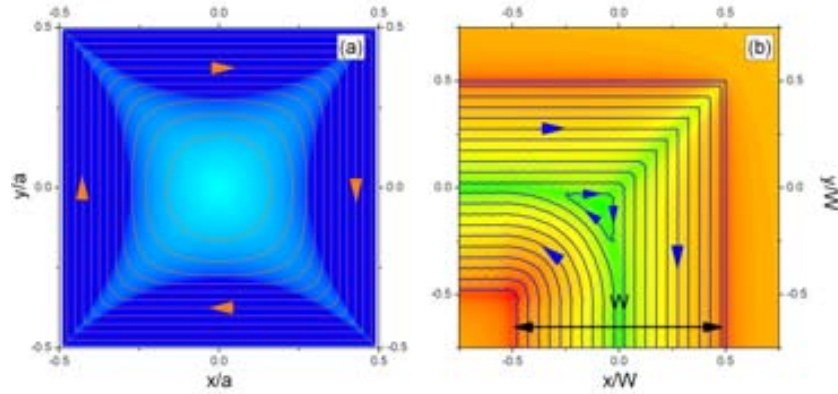


Figure 1.4: (a) Modulus of sheet current, **K** (color) and current stream lines (solid lines) within a thin square plate of side $t$ subjected to a positive perpendicular applied field $H_a \sim 0\ 5K_c$, before full saturation, and (b) out-of-plane magnetic induction $B_z$ (in color) and current stream lines (solid lines) near the sharp $\pi\ 2$ radians turn of a thin strip, subjected to a positive and perpendicular $H_a \to K_c$, where the sample full saturation has been reached. In (a) **K** ranges from 0 (lighter blue) to $K_c$ (dark blue) and in (b) $B_z$ ranges between 0 (green) and $+2\ 5K_c$ (red). Arrows show direction of current. Green regions in (b) show the meeting lines of different flux fronts, like the straight $d^+$-line running along the outer-corner angle bisector (see text).

Penetration of fields and currents in samples of these geometries present some common features with that of a strip. Some of these trends are the penetration of critical currents from the outer edges and the remanence of subcritical and flux-frozen regions at the sample innermost places. Also the infinities in the field at the sample edges and the field slope at the flux front are observed in this case. However, the sharp corners at the plate edges made these regions to penetrate in non-symmetrical ways.

In particular, the flux front was observed to penetrate deeper at the straight edges and far from the corners than at convex corners. The opposite happens at concave corners, where the critical region was found to penetrate deeper. Along the angle bisector of a sharp convex corner the penetration depth of the flux front is always zero. In rectangular plates the result is the cushion or star-like region discussed by Brandt [76, 102] (see Fig. 1.4a). The flux fronts penetrating from two edges forming a convex angle meet assimptotically, when the applied field is very large compared to $K_c$ (this infinity is removed by considering a finite $t$, $\lambda$ or $\Lambda$ as for the case of the straight strip). When they meet a $d^+$-line [12], where currents bend sharply to flow parallel to the closest

edge, develops along the bisector (see Fig. 1.4b). Differently, the critical currents, with modulus $K_c$, follow circular paths near a sharp concave corner. Even small holes within the sample lead to the formation of parabolic $d^+$-lines, extending to infinity [103, 104]. In this case, these lines delimit circular currents around the hole. Besides the infinite length of the $d^+$-lines, also observed were discontinuities and divergences in the electric field modulus $E$ near sharp concave corners. All of these effects are removed by the consideration of a finite $n$ creep exponent in the $E(J)$ power law [105, 106] (see Sec. 1.3).

The general $2D$ problem of determining field and current profiles in thin plates or strips of arbitrary shape, was not solved in the critical state under applied transport currents until recently [107].

**Magnetization and ac susceptibility of thin samples**  When considering thin samples under perpendicular applied fields, demagnetizing effects are very strong and the magnetization is very different from the averaged local self-field. In this case it can be calculated from equation 1.19. This out-of-plane magnetization was also found to follow a very similar dependence on the applied field for all thin shapes under the normalization $M_z(H_a \ H_s) \ M_s$, with $M_s$ and $H_s$ defined as above for the case of long samples [90]. In particular, in the perpendicular geometry this dependence was found to be close to a $\tanh(x)$. Moreover, in this case $\chi_0$ is very large, as discussed in section 1.3.1, but $M_s$ depends only on the sample cross section and not on its thickness [75].

The reversal and return curve can be obtained from equations 1.28 and 1.29, respectively, which are valid for arbitrary sample thickness and shape. Then, also from the initial curve the real and imaginary susceptibilities at fundamental frequency, $\chi$ and $\chi$ , can be obtained from equations 1.30 and 1.31, respectively. The behavior presented by these quantities for thin disks was studied by Clem and Sanchez [91]. In this case the trends described above for long samples also apply although here $\chi \qquad H_m^2$ is observed at low $H_m$.

## 1.4   Applications of thin superconducting films

Many and very different are the applications based on the special properties of superconducting materials. However, most of them are based on the high sensitivity to small external perturbations and on the high involved fields and currents.

In the particular case of thin films many of the applications are based on the critical field and currents to first vortex penetration. These are the cases, for example, of single-photon detectors (SNPDs) [108] and mass spectrometers, the latter using stripline detectors (SLD) as a detecting device [109]. They make use of the high voltage drop that appears when a resistive belt is generated by the incidence of a single photon or massive molecule, respectively. Superconductor-based bolometers like transmission-edge sensors (TES) [110] are radiation detectors also very sensitive, in this case thanks to the high-resistance change near $T_c$ produced by incident photons. Another device widely

used for its high sensitivity, this time to small external flux changes, is the superconducting quantum interference device (SQUID) [111, 112, 113]. Others such as the diodes and rectifiers base its operation in the dependence of this critical current on applied current polarity in asymmetric geometries [114]. Also the ratchet effect [115, 116, 117] arises from the dependence of vortex pinning and flow on the polarity of applied current in asymmetric hole lattices. This one is been proven very useful not only for applications but also to simulate ratchet potentials in biological systems such as step motors. Other electronics applications arise from the highly tunable cold atom trap [118], which appear as potential candidates for quantum simulation [119] and quantum-computing-gate implementation (see for example [120] and [121] and references therein). Making use of the high fields generated by superconductors are devices for particle accelerators such as waveguides [122] and superconducting radio-frequency (SRF) cavities [123]. The tunability of the magnetic response through geometric and other parameters of systems of superconducting thin strips and plates is convenient for the metamaterials design [124, 125, 126] as well.

The above applications make use of the high degree of sensitivity and tunability of involved magnetic fields and electric currents below (Meissner state) and near the conditions for first vortex penetration. However, the high allowed transport currents and large generated magnetic fields at low losses make of superconductors good materials for power and high-field applications as well [5]. In that case they usually operate in the mixed state and more precisely in the critical state (see Sec. 1.2). The reason for this is that high pinning forces are desired to avoid flux motion that would result in large energy losses. Actually, many advances and improvements have been made in the design of materials to get the best performance. The known as 2nd-generation HTS-material tapes or coated conductors [35], made of YBCO, are a good example of these developments. Among the applications making use of coated conductors are [127] the fault-current limiters, which limit the allowed current thanks to the sudden drop in conductivity at some threshold value $I_c$ [128], and also transformers, motors, cables for transportation of large currents with low losses, generators, magnets using the remanent magnetization for high-magnetic-field generation, and energy-storage systems that use either magnetic energy, as is the case of superconducting magnetic-energy-storage systems (SMES), or mechanical energy as in the stable levitation of spinning HTS magnets in flywheels.

In this type of materials the main source of losses comes from the cost in overcoming the pinning potential to move vortices both when varying applied fields and currents. These are the important and widely studied ac losses under ac currents and fields [129]. Moreover, the same effect of vortex pinning allows for the stable levitation of HTS samples in the presence of external fields [130].

# Magnetic Energy Minimization (MEM) model for thin samples

In the present work we will determine the response of thin planar superconducting samples of thickness $t$ and in-plane dimensions $W \to t$ both to applied transverse magnetic fields $H_a = B_a \ \mu_0$ and longitudinal transport currents $I_a$. In particular we seek for the fields and currents distribution, from which other magnetic quantities can be calculated. The material will always be assumed to be a high-$\kappa$ type-II superconductor. Two states will be considered: the Meissner ($B_a < B_{c1}$) and the critical ($B_{c1} \propto \ B_a < B_{c2}$) states. To simulate them we will use the London [7] and the critical-state [45, 46] models, respectively.

Since they were first presented in 1935 and 1964, respectively, these models have been applied to many different geometries and cases and by different analytical and numerical methods [36, 40, 41, 103, 76, 102, 131, 132, 68, 86, 51, 133, 66, 63, 64, 67, 134, 71, 74] (see chapter 1). All of these methods either solve a system of differential equations or minimize a given functional in order to determine this response in the corresponding state. In our case, we minimize a functional that can be interpreted as the Gibbs free energy of the system in some cases, as we will see below. Minimization is performed by the Magnetic Energy Minimization (MEM) model, first presented by Sanchez and Navau [133] and which has been applied to simulate superconducting samples of different geometries in different regimes [135, 136, 137, 70].

The chapter is organized as follows. First we introduce the problem we want to solve within the continuous formulation in section 2.1, defining all the needed involved quantities and the different cases we consider in the following chapters. Then, in section 2.2 we describe the particular discretization and numerical method we use to solve the fields and currents distribution and the other magnetic quantities in the superconducting samples.

## 2.1   Continuous Formulation

### 2.1.1   Geometry

We consider thin planar superconducting samples of uniform thickness $t$ much smaller than the shortest perpendicular dimension $W$, $t \propto W$, placed at $z \in (-t/2, +t/2)$, thus normal to the $z$ axis. These planar samples can be of any shape, including multiply connected geometries (i.e. presenting holes).

In particular, the considered geometries will include plates and sets of plates of different shapes that involve turns, widenings, constrictions, holes, or others. The samples can also be connected to two or more thin straight infinitely long superconducting strips through which some external current can be fed and drained. When this happens the strip is part of the considered sample.

**Twin films**

As an extension to the above situation, we will also consider in some cases a second sample parallel to the first one and located at a different $z$-plane. We shall call this twin plates.

### 2.1.2   Sheet current

The small values of $t/W$ allow to get most of the magnetic information from the thickness-averaged current density or sheet current, defined as (see Sec. 1.3.1):

$$\mathbf{K}(x, y) \equiv \int_{-t/2}^{+t/2} \mathbf{J}(x, y, z)\mathrm{d}z \tag{2.1}$$

The use of $\mathbf{K}$ instead of $\mathbf{J}$ reduces the 3D problem to a 2D one. In some cases this will be done at the cost of ignoring the current distribution across $t$. However, in some cases the current is nearly constant in the $z$ direction, and we can write $\mathbf{K}(x, y) \approx \mathbf{J}(x, y, 0)t$.

### 2.1.3   The sheet function $g(x,y)$

In order to determine the sheet current $\mathbf{K}$ distribution within the planar sample we have to seek for the two components of this vector field. However, provided that the continuity equation must be fulfilled ($\nabla \cdot \mathbf{K} = 0$) the problem can be further simplified.

A convenient way to account for this condition is to follow the approach presented by Brandt by defining the two-dimensional scalar sheet function $g(x, y)$ from

$$\mathbf{K}(\mathbf{r}) = \nabla \times (g(\mathbf{r})\mathbf{z}) = -\mathbf{z} \times \nabla g(\mathbf{r}) \tag{2.2}$$

where $\nabla \equiv (\partial_x)\mathbf{x} + (\partial_y)\mathbf{y}$ is the 2D nabla operator, $\mathbf{r} = x\mathbf{x} + y\mathbf{y}$ is the in-plane vector position and $\mathbf{x}$, $\mathbf{y}$ and $\mathbf{z}$ are the unit vectors along the $x$, $y$ and $z$ axis, respectively.

It is worth to mention that $g(\mathbf{r})$ is constant at regions where $\mathbf{K}(\mathbf{r}) = 0$, which includes the exterior of the superconductor.

Some important properties of the sheet function are [69]:

- The constant $g(\mathbf{r})$ lines correspond to current streamlines. This is why it is some times also called the stream function. In particular $g(\mathbf{r}) = \textbf{constant}$ along all the sample edges.

- The difference in $g(\mathbf{r})$ between two points within the sample plane equals the net current crossing any line connecting both points.

- The quantity $\Phi_0 g(\mathbf{r})$ is the potential of a vortex within the interior of bulk pinning free films.

- $g(\mathbf{r})$ is the local magnetization density or tiny current loops (see Sec. 2.1.6).

- The integral of $g(\mathbf{r})$ over the film area equals the magnetic moment of the film if $g = 0$ on its edge, in the absence of applied currents.

- If the film contains an isolated hole or slot such that magnetic flux can be trapped on it or a current $I$ can circulate around it, then in this hole one has $g(\mathbf{r}) = \text{constant} = I$ if $g(\mathbf{r}) = 0$ is chosen outside the film.

- In a multiply connected film with $N_h$ holes, $N_h$-independent constants $g_1,...,g_{N_h}$ can be chosen for the values of $g(\mathbf{r})$ in each of these holes. The current flowing between hole 1 and hole 2 is then $g_1 - g_2$.

- A vortex moving from the edge of the film into a hole connected to the outside by a slit, at each position $\mathbf{r}$ couples a fluxoid $g(\mathbf{r})\delta_0\, I$ into this hole, where $g(\mathbf{r})$ is the solution that has $g(\mathbf{r}) = I$ in this hole (with a closed slit) and $g = 0$ outside the film.

### 2.1.4   Energy functional terms

In the different cases we consider in the body of this work the distribution of $g(\mathbf{r})$ is obtained from the minimization of a functional $E$. Here we refer to $E$ as the Gibbs free energy of the system although, as we will see below, this equivalence cannot be made in some cases.

In the presence of an external applied field and currents flowing within the thin film, the total energy of the system, written in terms of $g(\mathbf{r})$ and its gradient, takes the form

$$E = E_{int} + E_{ext} \tag{2.3}$$

where

$$\begin{aligned}
E_{int} &= \frac{1}{2}\int_S \mathbf{K}(\mathbf{r}) \cdot \mathbf{A}_K(\mathbf{r})\mathrm{d}S = \\
&= \frac{\mu_0}{8\pi}\int_S \int_S \frac{g(\mathbf{r}) \cdot \quad g(\mathbf{r}\,)}{\mathbf{r} - \mathbf{r}}\mathrm{d}S\mathrm{d}S
\end{aligned} \tag{2.4}$$

is the internal magnetic energy, that accounts for the interaction between induced currents and the stray fields created by themselves, and

$$E_{ext} = \int_S \mathbf{K}(\mathbf{r}) \cdot \mathbf{A}_a(\mathbf{r}) \mathrm{d}S =$$

$$= \mu_0 H_a \int_S g(\mathbf{r}) \mathrm{d}S - \oint_{\partial S} g(\mathbf{r}) \mathbf{A}_a(\mathbf{r}) \cdot \mathrm{d}\mathbf{l} \qquad (2.5)$$

is the external energy, accounting for the interaction between the currents and the external uniform magnetic field applied in the normal to film direction $z$, $\mathbf{H_a}(\mathbf{r}) = H_a \mathbf{z}$ (see Sec. 2.1.5). In these equations $S$ is the outer contour of the sample, $S$ the planar ($z = 0$) surface enclosed in $S$ and $\mathrm{d}\mathbf{l}$ the line differential along it, $\mathrm{d}S = \mathrm{d}x\,\mathrm{d}y$, $\mu_0$ the vacuum permeability, and $\mathbf{A}_K(\mathbf{r})$ and $\mathbf{A}_a(\mathbf{r})$ are the magnetic vector potentials from the induced currents and from the external applied field, respectively. We use the Coulomb gauge and choose $\mathbf{A}_a(\mathbf{r}) = (\mu_0 H_a\ 2)(-y\mathbf{y} + x\mathbf{x})$.

**Twin films**

When there is a second plate near the first one, the total energy must account for three different contributions: the self energy of currents in each plate, that of interaction with the external field and the interaction between currents flowing in different plates.

Then we should take into account the contribution from the two plates, that is:

$$E_{int} \;=\; \frac{\mu_0}{8\pi} \sum_{k,k'=1}^{2} \int_{S_k} \int_{S_{k'}} \frac{g_k(\mathbf{r}) \cdot\ g_{k'}(\mathbf{r})}{\mathbf{r} - \mathbf{r} + (z_k - z_{k'})\mathbf{z}} \mathrm{d}S\mathrm{d}S \qquad (2.6)$$

and

$$E_{ext} = \mu_0 H_a \sum_{k=1}^{2} \left( \int_{S_k} g_k(\mathbf{r}) \mathrm{d}S - \oint_{\partial S_k} g_k(\mathbf{r}) \mathbf{A}_a(\mathbf{r}) \cdot \mathrm{d}\mathbf{l} \right) \qquad (2.7)$$

where subindex $k = 1$ and 2 for the different samples. In this case the plates $k$ are not placed necessarily at $z = 0$ but at $z = z_1$ and $z = z_2$, respectively, and hence still both perpendicular to the $z$ axis.

### 2.1.5   Studied cases

As mentioned above we minimize the functional given by equation 2.3 with respect to $g(\mathbf{r})$ in order to determine the response of the thin samples to applied fields and currents. Moreover, the samples are modeled in the Meissner and the critical states within their common assumptions (see Secs. 1.3.1 and 1.3.2). In this section we describe how these different magnitudes and states are simulated within our model.

**Transport and Magnetic cases**

**Magnetic case: application of a uniform perpendicular magnetic field.** When just a magnetic field but no net current is applied to the sample, $g = 0$ is chosen within the film contour. The applied magnetic field or induction is always assumed uniform and perpendicular to the thin sample surface. Then we can write $\mathbf{B_a}(\mathbf{r}) = \mu_0 H_a \mathbf{z}$. $H_a$ enters the model via the terms of the functional to be minimized through equation 2.5.

**Transport case: application of longitudinal transport currents.** When $H_a = 0$ but an external longitudinal current $I_a$ is applied, $I_a$ is fed and drained through thin infinitely long straight strips connected to the sample. Hence the sample geometry will have to include two or more of these cables.

The condition for no net current normal to the sample edges is set by forcing $g$ to be constant along them. Since the origin of $g$ can be chosen at will without loss of generality, we take $g = 0$ at one of the edges. Then the net current $I_{a,k}$ flowing through the $k$-th cable is set by fixing $g_{top,k} - g_{bottom,k} = I_{a,k}$, where, for simplicity, we name *top,k* and *bottom,k* the two edges of this cable. The direction of flow is determined by the sign of this difference and from the definition of $g(\mathbf{r})$ in equation 2.2.

By following this approach, as many cables as desired can be included in the sample geometry with at least one to feed and one to drain the applied current. Moreover, any net current can enter or leave the sample through each strip as long as the sum over all strips satisfies $\sum_k I_{a,k} = 0$.

Similar conditions for the application of a transport current were used by Sokolovsky *et al* in [71].

**Meissner and critical states**

**Meissner state.** When the sample is assumed to be in the Meissner state the effect of a finite two dimensional screening length $\Lambda \equiv \lambda^2 \ t$ can be accounted for (see Sec. 1.3.1). In this case the kinetic energy of the charge carriers $E_{kin}$ must be added to the magnetic energy given by equation 2.3. When one single plate is considered this energy term takes the following form:

$$E_{kin} = \frac{\mu_0 \Lambda}{2} \int_S [\mathbf{K}(\mathbf{r})]^2 dS = \frac{\mu_0 \Lambda}{2} \int_S [\ \ g(\mathbf{r})]^2 dS \qquad (2.8)$$

with all the involved quantities as defined in section 2.1.4. If a second thin sample is included then the integration of the same term over the second plate area must be added.

In the Meissner state, both $g(\mathbf{r})$ and $\mathbf{K}(\mathbf{r})$ are linear on $H_a$ and $I_a$. Then the distributions for arbitrary values of them can be obtained from the superposition of those for the magnetic and the transport cases.

When holes are present $g(\mathbf{r})$ must be uniform within the area of any hole $S_{hole}$, $g(\mathbf{r} \ \ S_{hole}) = \text{constant} \equiv g_{hole}$. The $g_{hole}$ value for which $E = E_{int} + E_{ext} + E_{kin}$ is minimum corresponds to zero fluxoids trapped at this particular hole. Thus, this state is

reached by minimizing $E$ without any constrain in $g_{hole}$. States with arbitrary non-zero number of fluxoids in a hole can be obtained from fixing $g_{hole}$ and minimizing $E$ under this constrain. When $H_a = 0$ and $I_a = 0$ in a sample presenting $N_h$ holes, if $g$ is fixed just at one of them, e.g. the $j$-th one, and unconstrained for all the others $(i = j)$, then the $g(\mathbf{r})$ and $\mathbf{K}(\mathbf{r})$ distributions are proportional to the $g_{hole}$ value at this hole, $g_{hole,j}$. Thus, the net fluxoid at hole $j$, $\Phi_j$, calculated from equation 2.24, is also linear on this parameter. This property allows for the obtaining of states with arbitrary number of fluxoids $N_{f,j} \equiv \Phi_j \ \Phi_0$ at each hole $j$ by linear combination of those with fixed $g_{hole,j}$ and unconstrained $g_{hole,i}$ (and hence $N_{f,i} = 0$)   $i = j$.

**Critical state**   The critical-state condition is applied by bounding the allowed values for the local sheet current. Moreover, being an irreversible and highly hysteretic state, $E$ from equation 2.3 does not represent the energy of the superconductor anymore. In this case we minimize $E = E_{int} + E_{ext}$ under the constraint

$$\mathbf{K}(\mathbf{r}) = \quad g(\mathbf{r}) \ \leq K_c \equiv J_c t \tag{2.9}$$

Samples in this state are sensitive not only to the present values of external magnitudes but also to the history of the sample, i.e. values applied previously (see Sec. 1.3.2). In particular, from the minimization of equation 2.3 under the constraint given by equation 2.9 we can simulate monotonic sweeps of applied $H_a$ or $I_a$ starting from the virgin state in a ZFC sample. Also by applying simultaneously $H_a$ and $I_a$ under these conditions, we simulate the case of monotonic sweep at constant rate $H_a \ I_a$.

However, when the magnitude that is being modified ($H_a$, $I_a$ or both of them), its sign of variation, or the sweeping rate $H_a \ I_a$, change, then a new stage starts. Then, to simulate an arbitrary sequence of $H_a$ and $I_a$ we must distinguish between currents at the end of the previous stage, or frozen currents, $\mathbf{K}(\mathbf{r})$ and the newly induced ones at the present stage $\delta\mathbf{K}(\mathbf{r})$. Then we write

$$\mathbf{K}(\mathbf{r}) = \mathbf{K}(\mathbf{r}) + \delta\mathbf{K}(\mathbf{r}) \tag{2.10}$$

for the total current. Analogously we define $H_a = H_a + \delta H_a$ and $I_a = I_a + \delta I_a$. The frozen sheet function $g(\mathbf{r})$ and the newly induced one $\delta g(\mathbf{r})$ can be defined analogously to $g(\mathbf{r})$ from equation 2.2 and from $\mathbf{K}(\mathbf{r})$ and $\delta\mathbf{K}(\mathbf{r})$, respectively.

To account for the different magnitudes from the previous stage the expressions for the $E$ terms given by equations 2.4 and 2.5 should be substituted by

$$E_{int} \quad = \quad \frac{\mu_0}{8\pi} \int_S \int_S \frac{g(\mathbf{r}) \cdot \ g(\mathbf{r} \ )}{\mathbf{r} - \mathbf{r}} \mathrm{d}S \mathrm{d}S \ - \frac{\mu_0}{4\pi} \int_S \int_S \frac{g(\mathbf{r}) \cdot \ g(\mathbf{r} \ )}{\mathbf{r} - \mathbf{r}} \mathrm{d}S \mathrm{d}S \tag{2.11}$$

and

$$E_{ext} = \mu_0(H_a - H_a) \int_S g(\mathbf{r}) \mathrm{d}S \tag{2.12}$$

respectively. Here the linearity of the gradient, the curl and the cross product are used. We also note that the second term in equation 2.5, contributing only at the far end of the feeding cables, has been dropped off. At the end of a stage the frozen ( ) quantities are refreshed to the present ones and are included in the $E$ terms at the steps of the following stage. Then the conditions

$$\mathbf{K}(\mathbf{r}) \;=\; \mathbf{K}(\mathbf{r}) + \delta\mathbf{K}(\mathbf{r}) \;\leq K_c \tag{2.13}$$

within the sample surface, and

$$g_{top,k} - g_{bottom,k} = I_a = I_{a,k} + \delta I_{a,k} \tag{2.14}$$

in all cables, must be fulfilled.

### 2.1.6   Other magnetic quantities as a function of $g(x,y)$

Once the $g(\mathbf{r})$ distribution is found, several magnitudes can be computed. Here we give the expressions in terms of $g(\mathbf{r})$ for some of them.

**Magnetic induction field**

The induction field produced by the currents flowing within the sample can be calculated from the Biot-Savart law. In this case its out-of-plane component, written in terms of $g(\mathbf{r})$, is given by

$$B_z(x\ y\ z) = \frac{\mu_0}{4\pi} \int_S \frac{g(\mathbf{r}\ )\cdot\mathbf{R}}{\mathbf{R}\ ^3}\mathrm{d}S \tag{2.15}$$

and its in-plane component by

$$\mathbf{B}_{xy}(x\ y\ z) = \frac{\mu_0}{4\pi} \int_S \frac{-z\ \ g(\mathbf{r}\ )}{\mathbf{R}\ ^3}\mathrm{d}S \tag{2.16}$$

where $\mathbf{R} = (x - x\ )\mathbf{x} + (y - y\ )\mathbf{y} + z\mathbf{z}$. The out-of-plane component takes the following simplified expression when evaluated at the sample plane:

$$B_z(x\ y\ 0) = B_z(\mathbf{r}) = \frac{\mu_0}{4\pi} \int_S\ \ g(\mathbf{r}\ )\cdot\ \ \left(\frac{1}{\mathbf{r} - \mathbf{r}}\right)\mathrm{d}S \tag{2.17}$$

For obtaining the total field we have to add to equations 2.15 and 2.17 the perpendicular applied induction.

In the case of twin films the contribution to total magnetic induction from the two of them must be accounted for.

**Magnetic moment and magnetization**

In the absence of applied transport currents, a finite planar sample placed normal to the $z$ axis has zero in-plane magnetic moment. Its out-of-plane component is

$$m_z \mathbf{z} = \frac{1}{2} \int_S \mathbf{r} \times \mathbf{K}(\mathbf{r}) \mathrm{d}S = \int_S g(\mathbf{r}) \mathrm{d}S \mathbf{z} \qquad (2.18)$$

The magnetization of the sample is defined as the magnetic moment per unit volume,

$$M_z = \frac{1}{t A_S} m_z \qquad (2.19)$$

with $A_S$ the total area of the sample.

When considering twin films, the net magnetic moment of the set, $m_{T,z}$, is obtained from the sum of the contributions from each of them. In this case $m_{T,z}$ must be divided by the total volume of the set of samples $V_T = t \sum_k A_{S_k}$ in order to get the magnetization of the system. Here $A_{S_k}$ refers to the area of the $k$-th plate.

Hard superconductors modeled within the critical state model present a hysteretic magnetization curve. In this case, the initial magnetization $M_{ini}(H)$ is induced within a ZFC sample when increasing applied field from 0 to $H$. The reversal magnetization $M_{rev}(H)$ is obtained when the field is reversed down to $H$ after reaching a maximum value $H_m$ in the initial curve. Finally, the return curve $M_{ret}(H)$ results from increasing back the field up to $H$ after the reach of $-H_m$ in the reversal curve. The magnetization hysteresis loop is composed from the reversal and the return curves. At this point, when cycling applied field between $-H_m$ and $+H_m$ the reversal and return curves are followed during the ramping-downs and the ramping-ups, respectively. In the critical state both the reversal and return magnetization curves can be obtained from the initial magnetization from equations 1.28 and 1.29, respectively.

**External susceptibility**

The external susceptibility can be defined from the sample magnetization. In the particular case of linear response to applied fields this susceptibility is minus the slope of the $M_z(H_a)$ curve, i.e.

$$\chi_0 \equiv -M_z \ H_a \qquad (2.20)$$

In this work we will always refer to the external susceptibility, which depends on the particular sample shape in opposition to the magnetic or internal susceptibility [49].

When the response is not linear, the ac susceptibilities are often measured or calculated from the response to alternating applied fields. In the particular case of a field time dependence $H_a(t) = H_m \cos(\ t)$ the real and imaginary ac susceptibilities are defined by equations 1.30 and 1.31. We are interested in the fundamental component $(n = 1)$. These susceptibilities are calculated from the Fourier transform of the magnetization hysteresis loop and hence from the reversal and return curves. However, thanks to

equations 1.28 and 1.29 it can also be obtained from the initial magnetization $M_{ini}(H_a)$. Then the expressions for $\chi$ and $\chi$ are

$$\chi = -\frac{4}{\pi H_m} \int_0^\pi M_{ini} \left( H_m \sin^2 \left( \frac{\theta}{2} \right) \right) \cos\theta \mathrm{d}\theta \tag{2.21}$$

$$\tag{2.22}$$

and

$$\chi = \frac{4}{\pi H_m^2} \left[ M_{ini}(H_m) H_m - 2 \int_0^{H_m} M_{ini}(H) \mathrm{d}H \right] \tag{2.23}$$

respectively.

**The fluxoid**

From the current and field profiles the magnetic fluxoid, always multiple of the flux quanta ($\Phi_0$), can also be calculated (see Sec. 1.3.1). In this case the net fluxoid crossing a given area $A$ within one of the films can be calculated from

$$\Phi = \int_A B_z(\mathbf{r})dS - \mu_0 \Lambda \oint_{\partial A} (\mathbf{z} \times g(\mathbf{r})) \cdot \mathrm{d}\mathbf{l} \tag{2.24}$$

where the first term in the right hand-side is the net flux through $A$ of $B_z$, calculated from equation 2.17, and the second one is $\mu_0 \Lambda$ times the net current circulation along the contour of this area, $A$.

## 2.2 Numerical Method

In this section we present the numerical method and the particular algorithm we use to determine the current distribution in the situations described above.

After describing how the samples are discretized in section 2.2.1 and how the initial and boundary conditions are set in section 2.2.2, the numerical calculation procedure is presented in section 2.2.3. Then we describe the different conditions for the simulation of the different states in section 2.2.4 and how to include a second twin film in section 2.2.5. Finally the algorithm of the computing program to obtain numerically the current distributions is shown in section 2.2.6.

### 2.2.1 Discretization

We discretize the sample dividing it in $C = N \times M$ identical rectangular cells of sides $\delta_x$ and $\delta_y$ along the $x$ and $y$ axis directions, respectively. This division defines a grid of the $N \times M$ cells and a grid of $(N+1) \times (M+1)$ nodes at their corners.

The discretized $g_n$ function is defined at the nodes $n = 1$ $(N+1) \times (M+1)$. The gradient of the sheet function $\mathbf{G}_c = [ g(\mathbf{r})]_c$, also entering the functional to be minimized, is defined at each cell surface, where it is assumed to be uniform. It is calculated from the bilinear interpolation of the values of $g$ at the four nodes adjacent to the cell $c$.

**Energy terms**

After the sample is been discretized and provided that the current density $\mathbf{K}(\mathbf{r})$ is assumed to be uniform within each cell, the energy terms given by equations 2.4 and 2.5 take the expressions

$$E_{int} \quad \frac{\mu_0}{2} \sum_{c,c'} \mathbf{G}_c \cdot \mathbf{G}_{c'} N_{cc'} \tag{2.25}$$

and

$$E_{ext} \quad \frac{\mu_0 H_a}{4} \sum_c \sum_{i=0}^{3} g_c^i \delta_x \delta_y \tag{2.26}$$

respectively, being $N_{cc'} = [1 \ (4\pi)] \int_{S_c} \int_{S_{c'}} (1 \ \sqrt{(x-x\ )^2 + (y-y\ )^2}) \mathrm{d}S \mathrm{d}S$ with $S_c$ the surface of cell $c$ (analytical expressions of $N_{cc'}$ are available in Eq. (A5) of [137]) and $g_c^i$ ($i = 0\ 1\ 2\ 3$) the value of $g$ at the $i-$th adjacent node to cell $c$. $c$ and $c$ range from 1 to $C$. The second term in equation 2.5 is been dropped off (see Sec. **Critical State** of 2.1.5).

### 2.2.2   Initial and boundary conditions

**Conditions for the application of magnetic fields**

The magnetic field is applied as described in section 2.1.5 by setting the $H_a$ value entering the discretized equation 2.26 in the model.

**Conditions for the application of transport currents**

The applied transport currents are taken into account via the boundary conditions for the $g(\mathbf{r})$ function at the outer edges of the sample (see Sec. 2.1.5). However, to model the sample we need to cut off the infinite cables at some given distance $L_{lead}$ from the region of interest, i.e. that including turns, widenings, constrictions or holes. These segments where the feeding cables are cut off will be referred to as the leads.

Therefore, $g$ will have to vary along these leads to account for the non-zero current crossing them. $g$ will then be uniform along some segments of the edges of the simulated region (outer edges of the sample) and nonuniform along others (leads). The $g_n$ values at all the nodes belonging to a given outer edge of the sample must take the same value $g_{edge}$. The particular fixed $g_{edge}$ value at each outer edge allows to set the applied transport current. The final distribution in the region of interest is independent on the values $g_n$ takes at the leads provided that $L_{lead}$ is chosen to be long enough.

**Initial conditions: Setting the initial distribution ($g_0(\mathbf{r})$)**

An initial distribution for $g(\mathbf{r})$, $g_0(\mathbf{r})$, must be set before the minimization procedure can start. It is worth to mention that there is some freedom on the choice of $g_0(\mathbf{r})$, although an ansatz distribution close to the final one yields a much faster convergence.

However, in the critical-state simulations one must start from discretized distributions $g_{0,n}$ with $\mathbf{G}_{0,c} \leq K_c$ within all the cells in the sample surface.

When no external current is fed, this initial distribution can be taken as $g_{0,n} = 0$ anywhere within the plate.

However, if some current enters and leaves the sample via thin strips, as discussed in section 2.1.4, then $g_n$ must change from one edge to another and along the leads. Generally, we account for that by starting with a $g_{0,n}$ distribution corresponding to a uniform sheet current $\mathbf{K}$ flowing parallel to the closest edge.

### 2.2.3 Minimization procedure

We determine the $g_n$ distribution induced within the thin sample in the different considered cases by minimizing a given quantity $E$ related to the work done over the system. As mentioned in section 2.1.4, $E$ corresponds to the energy of the system only when the sample is in the Meissner state. The procedure we use to perform this minimization is described as follows.

First we set the mesh, external magnitudes and initial $g$ distribution. We then begin a process in which we look for the node $n_{op}$ where either a positive or negative variation of its $g$ value ($\pm \Delta g$, for fixed $\Delta g > 0$) leads to the largest decrease of the quantity $E$. Once this node is found we modify the $g_{n_{op}}$ by the corresponding amount $\Delta g$, with the corresponding sign. This process is repeated until there is no node where a change in $g$ decreases $E$. Modifying the external conditions, we restart the process.

When the system presents some symmetries we look for the node $n_{op}$ just among these at one of the symmetrical regions. Once this node is found the change in $g_{n_{op}}$ with the right sign is applied on it and all its symmetrical ones. Therefore, if twin films are considered, we only need to look for the node $n_{op}$ at one of them.

When holes are present, the condition of zero current within the holes interior is given by forcing $g_n$ to take the same value $g_{hole}$ at all nodes belonging to the hole, including its edges. In this case, we have to search among both the $g_n$ values within the sample interior and the different $g_{hole}$ values at these holes for the one whose change leads to the largest decrease in $E$. When the change is applied at a hole, this must be done at all its nodes (including its edges) simultaneously.

**Iterative mesh**

The computing times can be significantly reduced by making use of initial $g_n$ distributions close to the final one. One way to get much faster results, based on this idea, is by iterating on the number of cells. This technique is only valid for samples in the Meissner state since it induces a large error when the critical-state condition is included. The procedure is described as follows.

First we find the $g_n$ distribution giving the minimum of energy for a small number of cells $N_x \times N_y$ (typically $N_W = 10$ along the shortest in-plane dimension). Then a new mesh is defined by doubling the number of cells along both the $x$ and $y$ axis directions

$(N_x \times N_y = (2N_x) \times (2N_y))$. At the nodes which are common to the new and the old meshes, the new $g_{0,n}$ is set to $g_n$. At the other nodes $g_{0,n}$ is obtained from the linear interpolation of the values at the closest nodes. From this new initial distribution the minimization procedure can start again, now with a smaller $\Delta g$ (typically a fourth of the previous one), to determine the profiles of fields and currents in this larger mesh. We proceed like that as many times as needed to achieve the desired space resolution.

### 2.2.4 Meissner and critical states

**Meissner state**

The $g_n$ distribution in thin samples in the Meissner state is determined from the numerical procedure described in section 2.2.3 with $E = E_{int} + E_{ext} + E_{kin}$, where $E_{int}$ and $E_{ext}$ are given by equations 2.25 and 2.26, respectively, and

$$E_{kin} = \frac{\mu_0 \Lambda}{2} \sum_c (G_{c,x}^2 + G_{c,y}^2)\delta_x \delta_y \tag{2.27}$$

is the discretized expression of equation 2.8.

When $g_{hole}$ at a hole is set free during the minimization procedure as described in section 2.2.3, the state with $N_f = 0$ at the hole is reached. Integer values of trapped fluxoids $N_f = 0$ in a given hole are simulated by fixing $g_{hole}$ there (see Sec. 2.1.5). In this case we must start from an initial $g$ distribution $g_{0,n}$ with $g_{hole} = 0$ at some holes. Then we usually start from a distribution corresponding to a uniform sheet current surrounding the hole and parallel to its closest edge.

**Critical State**

When the sample is modeled within the critical-state assumptions, the critical-state condition must be included. This is taken into account by applying the changes in $g$ $g \pm \Delta g$ only at nodes and holes where this change leads to values of $g_c \leq K_c$ at all cells $c$ adjacent to the respective node or hole.

As discussed in section 2.1.5, when the external magnitude that is being modified ($H_a$ or $I_a$) or its sign of variation, are changed, a new stage starts. In this new stage the frozen currents $\mathbf{K}$ present at the end of the finishing stage, must also be accounted for. Then the quantity $E$ in the minimization procedure is given by the sum of

$$E_{int} \quad \frac{\mu_0}{2} \sum_{c,c'} \mathbf{G}_c \cdot \mathbf{G}_{c'} N_{cc'} - \mu_0 \sum_{c,c'} \mathbf{G}_c \cdot \mathbf{G}_{c'} N_{cc'} \tag{2.28}$$

and

$$E_{ext} \quad \frac{\mu_0(H_a - H_a)}{4} \sum_c \sum_{i=0}^{3} g_c^i \delta_x \delta_y \tag{2.29}$$

obtained from discretizing equations 2.11 and 2.12, respectively. All the quantities appearing in the above expressions are defined in section 2.2.1.

Therefore, under these assumptions, when a stage comes to an end we save the values and distributions of the frozen quantities, i.e. $g_n$, $\mathbf{G}_c$, $I_a$ and $H_a$, and use them in the new initial conditions and functional $E$ for the new stage.

### 2.2.5   Twin Films

When a second parallel plate is placed in the neighborhood of the first one, its contribution to the functional $E$ must also be accounted for. This is been done in the expression for $E$ given by equations 2.6, 2.7 and 2.8 including the integration over the surface of the second plate. After the sample is discretized these equations can be written as follows:

$$E_{int} \quad \frac{\mu_0}{2} \sum_{k,k'=1}^{2} \left( \sum_{c,c'} \mathbf{G}_{k,c} \cdot \mathbf{G}_{k',c'} N_{kk',cc'} \right) \tag{2.30}$$

$$E_{ext} \quad \frac{\mu_0 H_a}{4} \sum_{k=1}^{2} \left( \sum_{c} \sum_{i=0}^{3} g_{k,c}^i \delta_x \delta_y \right) \tag{2.31}$$

and

$$E_{kin} = \frac{\mu_0 \Lambda}{2} \sum_{k=1}^{2} \left( \sum_{c} (G_{c,x}^2 + G_{c,y}^2) \delta_x \delta_y \right) \tag{2.32}$$

where $k$ $k$ $= 1$ and 2 for the different samples. Hence

$$N_{kk',cc'} = \frac{1}{4\pi} \int_{S_{k,c}} \int_{S_{k',c'}} \frac{\mathrm{d}S \mathrm{d}S}{\sqrt{(x - x\,)^2 + (y - y\,)^2 + (z_k - z_{k'})^2}} \tag{2.33}$$

with $S_{k,c}$ the surface of cell $c$ in the $k$-th sample and $z_k$ the position along $z$ of this sample (the expressions for these terms are given in appendix A). The above expression is valid for any shape and arrangement of the two films as long as they are parallel.

### 2.2.6   Algorithm

The algorithm of the whole numerical procedure described in the previous sections is given by the flow diagram sketched in figure 2.1. The module labeled as *Minimization* contains the minimization process for a given set of parameters for the geometry, the discretization and the initial and boundary conditions. This process is sketched in figure 2.2.

For samples in the critical state the numbers of cells $N$ and $M$ in the discretized sample never change. This is so for all cases since, as mentioned in section 2.2.3, otherwise we would get a large numerical error. The frozen $g_n$ distributions ($g_n$) and frozen applied field and current ($H_a$ and $I_a$, respectively) are always zero in samples in the Meissner state. In this regime the current distribution depends only on the present values of external magnitudes and not on previously attained ones. Therefore, no stages are defined there.
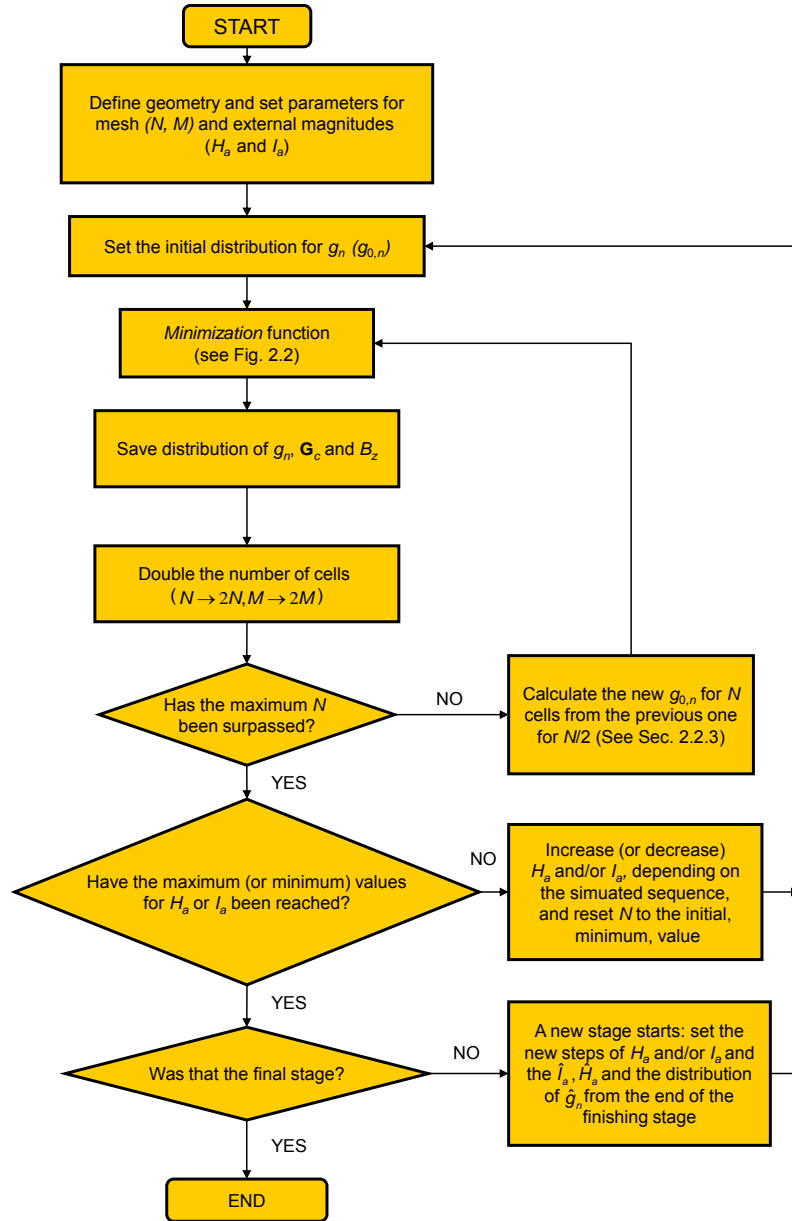
Figure 2.1: Flow diagram of the algorithm used to determine the current distribution in thin planar superconducting samples subjected to externally applied perpendicular magnetic fields and/or longitudinal transport currents (see Sec. 2.2.3). By following this procedure, any sequence of the external applied magnitudes can be simulated. The box labeled as *Minimization* is detailed in figure 2.2, which is used to determine the $g_n$ distribution for a particular set of conditions.
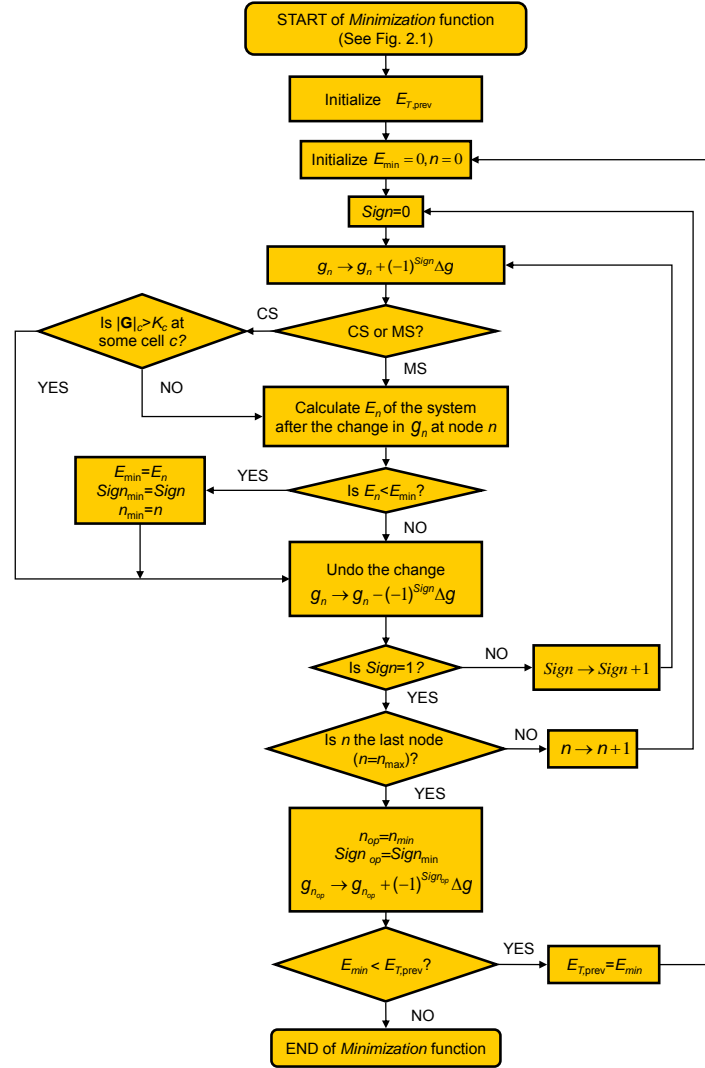
Figure 2.2: Flow diagram of the module labeled as *Minimization* in figure 2.1. It sketches the process used to determine the $g_n$ distribution for which the functional $E$ in equation 2.3 is minimum under a given set of applied fields and currents. At each step, while trying the change in $g$ at all nodes, the node counter $n$ is increased from 1 to $n_{max} = (N+1) \times (M+1)$. $Sign_{min}$, $n_{min}$ and $E_{min}$ are the temporary variables, used during the test for the change in $g_n$ at all nodes, whose final values are $Sign_{op}$, $n_{op}$ and $E_{T,prev}$, respectively. If the critical-state (CS) condition is considered, changes in $g_n$ are only tried at nodes $n$ where the gradient $(\nabla g)_c = \mathbf{G}_c$ at the cells $c$ sharing the node $n$ does not violate the condition $\mathbf{G}_c < K_c$. No such condition is applied in the Meissner state (MS). $E_{T,\text{prev}}$ is the value for $E$ before the present change is been applied.

Magnetic response of thin films in the Meissner state

In the present chapter we study the response of thin high-$\kappa$ ($\lambda \to \xi$) type-II superconducting samples in the Meissner state to applied magnetic fields and transport currents. The samples will be modeled within the London model and the large demagnetizing effects will be accounted for.

The chapter is organized as follows. In section 3.1 we study the behavior of fields and currents in thin strips of arbitrary two-dimensional screening length $\Lambda$ for different planar geometries, considering both the magnetic and transport cases. In section 3.2, the behavior of a penetrating vortex near a sharp $\pi$ 2-turn in a strip is studied for different $\Lambda$ and applied field and current combinations. Finally, in section 3.3 we study how thin square planar superconducting plates react to externally applied magnetic fields, and in particular we focus on the effects of a second parallel plate placed on top of the first one.

## 3.1 Magnetic and transport Meissner currents in superconducting thin films

In this section we consider thin planar strips of width $W$ and different geometries within the London model, both under applied transport currents $I_a$ and magnetic fields $H_a$ and for different $\Lambda$ $W$ values. We also study the case of a strip with a hole in the zero and trapped fluxoid cases. In chapter 1 we reviewed the existing solutions for different geometries in the magnetic case and stated that only the highly symmetrical cases of a a single and many straight strips was solved for the transport case. More recently were also studied for this case arbitrary thin geometries in the narrow [73] and complete shielding [71] limits. Here we show some of the general trends arising near turns, widenings, constrictions and holes when a finite non-zero $\Lambda$ $W$ is accounted for.

The results we present here complete the ones described in the above mentioned works. We also show how we recover the proper limits, such as the ones for straight strips at regions far from the non-straight segments.

In all the results presented below, meshes with a unit cell width of $\delta_x = W\ 40$ were used and parameters $\Delta g \approx 10^{-4} H_a W$ and $\Delta g \approx 10^{-4} I_a$ were chosen for the magnetic and transport cases, respectively.

### 3.1.1   Sharp $\pi/2$-Turn

The distribution of the sheet function $g(\mathbf{r})$ (see Sec. 2.1.3) induced in a thin strip of width $W$ with a $\pi$ 2-turn was obtained from the minimization procedure described in chapter 2. In this case we considered both the application of external magnetic fields and transport currents and accounted for an arbitrary 2D screening length $\Lambda \equiv \lambda\ t^2$ (see Sec. 1.3.1). It is interesting to point out that in the complete shielding ($\Lambda\ W \propto 1$) and narrow ($\Lambda\ W \to 1$) limits, it is possible to neglect the kinetic energy (see Eq. 2.8) from charge carriers and magnetic energy (see Eq. 2.4) of interaction between fields and currents, respectively. From the $g(\mathbf{r})$ function the profiles of sheet current, $\mathbf{K}$, and out of plane magnetic induction $B_z$, within the sample plane, where computed with the aid of equations 2.2 and 2.17, respectively.

We plot in figure 3.1 the out-of-plane magnetic induction and current streamlines (the contour lines of $g(\mathbf{r})$) in the region near the corner of the strip. We consider both the magnetic and transport cases and different values of $\Lambda\ W$ are plotted. The cases with $\Lambda = 0\ 01W$ and $\Lambda = 100W$ were chosen as representative for the $\Lambda \propto W$ and $\Lambda \to W$ limits, respectively. We have checked that more extreme values for $\Lambda\ W$ do not produce significant differences with respect to the presented ones.

When a transport current is applied (Figs. 3.1a-3.1c and 3.2), current accumulates at the inner corner of the turn regardless of the value of $\Lambda\ W$, diverging at the sharp corner for all cases. This effect, known as current crowding in the narrow limit, was already reported by Clem and Berggren [73] (see Sec. 1.3.1) and experimentally demonstrated by Adami *et al* in [138].

It is worth noting that the underlying mechanism giving rise to this accumulation is different in the different limits. For $\Lambda\ W \to 1$ the kinetic energy is much larger than the magnetic one and the fluid behaves as if no magnetic fields were present. In this case the distribution is that any massive ideal, non-viscous, fluid would follow, no matter if charged or uncharged. We can also observe the accumulation of currents near the inner corner is accompanied by a corresponding expansion near the outer one. On the opposite limit, with $\Lambda\ W \propto 1$, the magnetic energy is dominating and currents distribute in order to shield the self plus external out-of-plane induction, i.e. $B_z = 0$, at the sample surface. In this case the observed behavior at both the inner and outer corners, analogous to that observed in the magnetic case (see Sec. 1.3.1), can be understood as follows. When comparing to the straight strip case we observe: (i) turning currents make a lower (larger) field in their exterior (interior), with respect to a straight current; (ii)
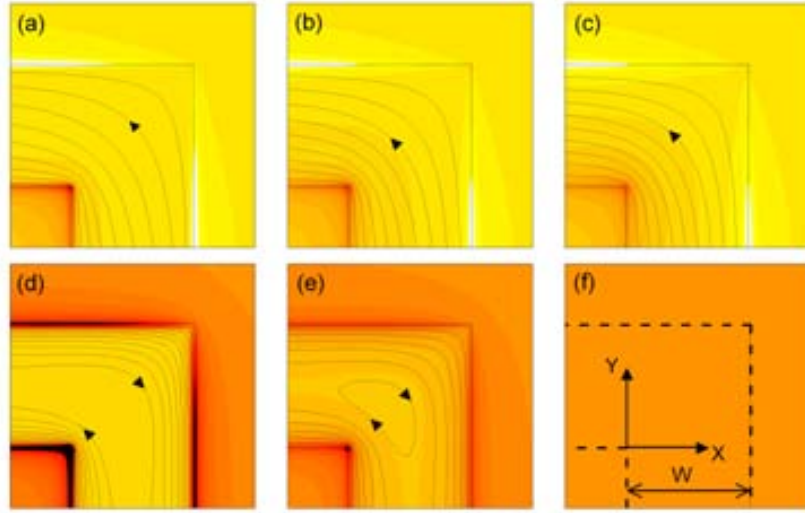
Figure 3.1: Current streamlines (full lines) and contour of out of plane magnetic induction (color scale) induced within an infinitely long strip with a sharp $\pi$ 2-turn under an applied longitudinal transport current, $I_a$, (upper row) or a perpendicular magnetic field, $H_a$, (lower row) and for $\Lambda$ $W =$ (left column) 0.01, (mid column) 0.1, and (right column) 100. Perpendicular magnetic induction ranges between $-0$ $5\mu_0 I_a$ $W$ (light yellow) and $+3$ $0\mu_0 I_a$ $W$ (dark red) in the transport case and between $-0$ $5\mu_0 H_a$ and $+3$ $0\mu_0 H_a$ in the magnetic case. Painted in black and in white are regions above and below this range, respectively.

then, currents trying to shield their self-field have to be more (less) intense in the inner (outer) corner; (iii) thus, field at the exterior of the superconductor is largely enhanced (decreased) at the inner (outer) corner. Naturally, for intermediate values of $\Lambda$, a combination of both effects is present.

We also note that the accumulation of current density due to shielding is higher than that due to the current crowding effect as seen in Figs. 3.1 and 3.2, where this accumulation is more evident for lower $\Lambda$ $W$ values. However, the rate of decay there is found not to depend very much on $\Lambda$ for the whole range of values $\Lambda$ $W$ [0 ]. This small dependence on $\Lambda$ near the corner contrasts with that along the straight segments of the strip. In fact, while currents suffer almost no change along the close-to-corner edge for different $\Lambda$, they are uniform far from it in the large $\Lambda$ case.

In the complete shielding limit, the effect of the corner on the current distribution is observed to last up to much longer distances $d$ from this corner than in the narrow limit. However, although significant, this difference is very slight for $d \geq W$. In the narrow limit, the uniform current distribution is almost met at $d = W$. Thus, the lower $\Lambda$ $W$ is, the farther from the turn we should go in order to recover the straight strip results. This is so because when $\Lambda$ $W \rightarrow 1$ the effect of the corner is a short distance
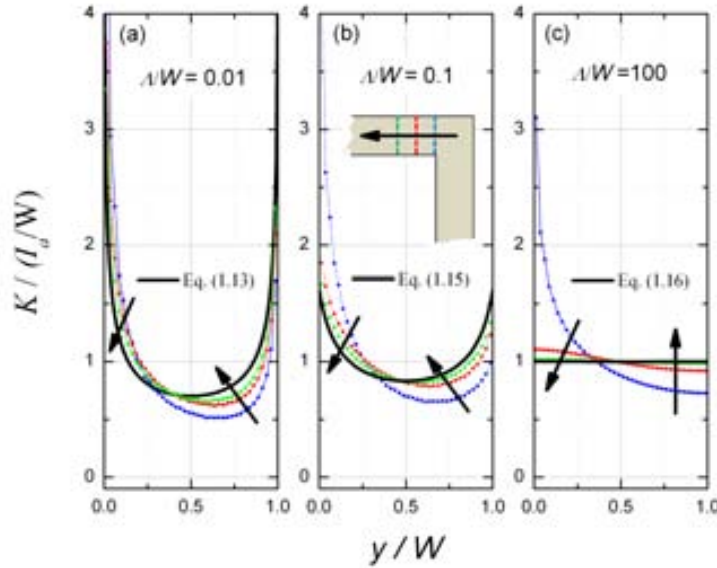
Figure 3.2: Modulus of the sheet current along lines of constant $x$ crossing the strip at distances $d = 0$ $W$ $2$ and $W$ from the beginning of the $\pi$ $2$ turn [arrows indicate direction of increasing $d$, as sketched in the inset of (b)] in the case of transport currents ($H_a = 0$) and for different values of $\Lambda$ $W$ =(a) 0.01, (b) 0.1, and (c) 100. Full thick lines show the limiting cases given by the indicated equations.

one, propagated only through the continuity equation condition. Instead, for low $\Lambda$ $W$ currents interact via their stray fields, which leads to a much longer range interaction. Something similar happens at the outer edge, but in this case currents vary slightly along it both for the narrow and complete shielding limits.

In the magnetic case, see Fig. 3.1d-f and Fig. 3.3 (in solid black lines we also show the analytical limits for a straight strip case), a zero net current is forced to flow along the strip. Now currents try to shield not only their self-field but also the external one. In this case when $\Lambda$ $W \rightarrow 1$ the sample becomes transparent to applied fields. Here the presence of the turn is also detected farther away from it as $\Lambda$ $W$ decreases. Currents in the inner corner and in the outer one have now different directions, so that the field they produce is positive (along $+z$) close to both corners (outside the superconductor). With respect to the straight strip, the ($\pi$ $2$)-turn yields an increase of field and current density near the inner corner, as in the transport case. However, magnetic currents also accumulate in the outer corner in order to shield, not only the self-field, but also the applied one. It is only very close to the outer corner where the geometry-driven current expansion dominates over this accumulation. We also observe that, when $\Lambda$ $W$ increases, the magnetic energy of interaction between external field and currents, $E_{ext}$, becomes less important and the applied field penetrates deeper into the superconductor.
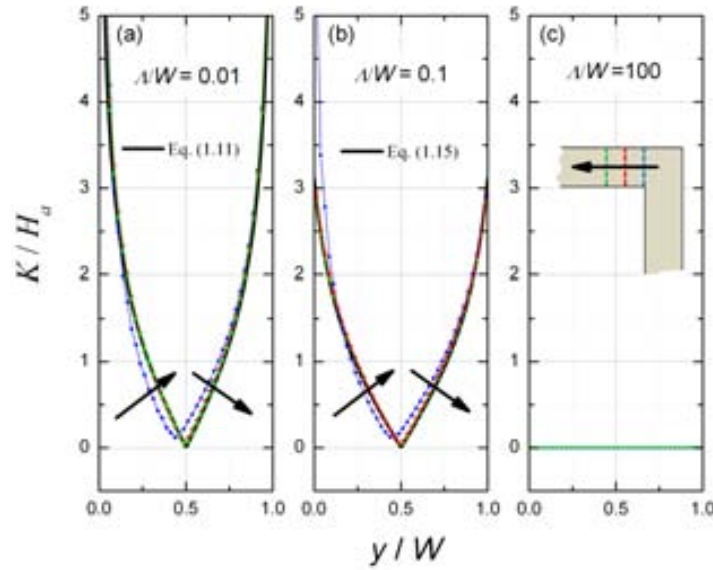
Figure 3.3: Modulus of the sheet current along lines of constant $x$ crossing the strip at distances $d = 0$ $W$ $2$ and $W$ from the beginning of the $\pi$ $2$ turn [arrows indicate increasing $d$, as sketched in the inset of (c)] in the case of magnetic currents ($I_a = 0$) and for different values of $\Lambda$ $W =$(a) 0.01, (b) 0.1, and (c) 100. Full thick lines show the limiting cases given by the indicated equations.

As a consequence, the current density (modulus) tends to decrease to zero for $\Lambda$ $W \to 1$.

Comparing transport and magnetic cases we see that in the former the net total current across any line connecting the borders must be $I_a$, so changing $\Lambda$ $W$ will produce some redistribution of the current in the superconductor (Fig. 3.1a-c). Instead, the net total current across any line connecting the borders must be zero in the magnetic case. Thus, not only the current is redistributed but also the magnitude of the induced currents at a given point is decreased down to zero when $\Lambda$ $W$ increases up to infinity (Fig. 3.1d-f).

Just as in the narrow limit case described in section 1.3.1 we expect the divergences at the sharp corner to be removed by considering a finite radius of curvature at the corner for the finite $\Lambda$ case as well. In the limit $\Lambda$ $W \propto 1$ the divergences are found even at the straight edges.

### 3.1.2 Sharp $\pi$-turnarounds

In this subsection we consider a thin strip of width $W$ which, at some point, presents a sharp U-turn, so that the two branches of the strip are separated by a thin slit of width $b \propto W$ and its edges are perpendicular (see Fig. 3.4). The origin of coordinates is chosen now to be at the end point of the slit.

In the current and field distributions, there are some trends similar to the $\pi$ $2$-turn
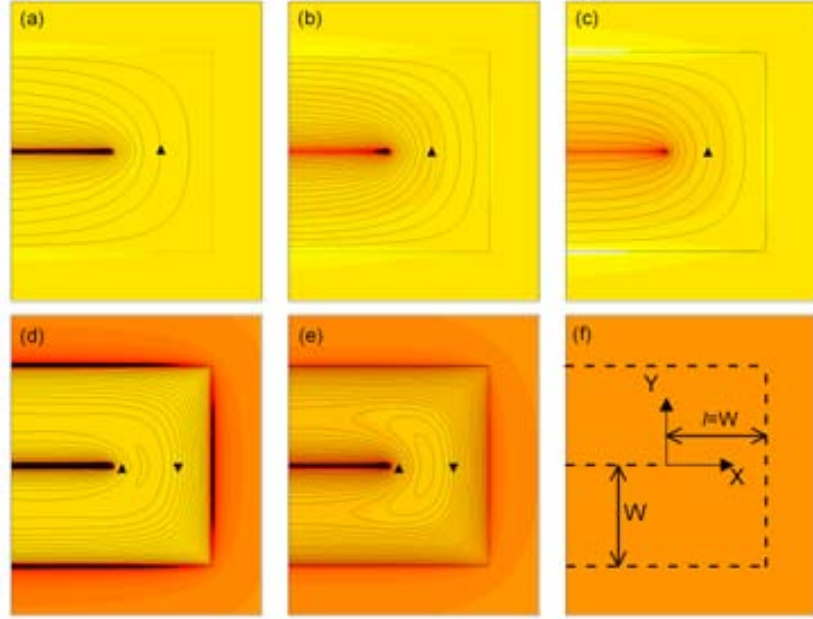
Figure 3.4: Same as in figure 3.1 but for a strip with a $\pi$ sharp turn with straight perpendicular edges.

case: the current crowding effect can be seen in the inner corner (now a sharp slit) and current expansion in the outer corners. Both effects are more pronounced as $\Lambda\ W$ decreases. Close to the end of the slit, currents undergo a U-turn. This leads to an accumulation of currents due to both current crowding ($\Lambda\ W \to 1$) and shielding of fields ($\Lambda\ W \propto 1$). Both effects are larger in the present geometry than in $\pi$ 2-turns.

When approaching the $\pi$-turnaround, its presence is made evident sooner in the transport case than in the magnetic one, like in the $\pi$ 2-turn. Moreover, if $\Lambda\ W$ decreases, the effects of the turnaround reach longer distances from it. This is shown in Figs. 3.5 - 3.6, where we plot the modulus of the sheet current along different lines perpendicular to the slit and crossing the strip from the slit to one border. These lines correspond to distances $d = 0$, $W\ 2$, and $W$ from the beginning of the turn. In this case the straight segments remain parallel and close to each other up to infinite distances from the turn. Then their interaction is high and the single strip is not recovered. Actually, in that region we should recover the solution for two parallel coplanar straight strips ($2st$), separated by a distance $b \propto W$. In this case, the transport ($T$) and magnetic ($M$)
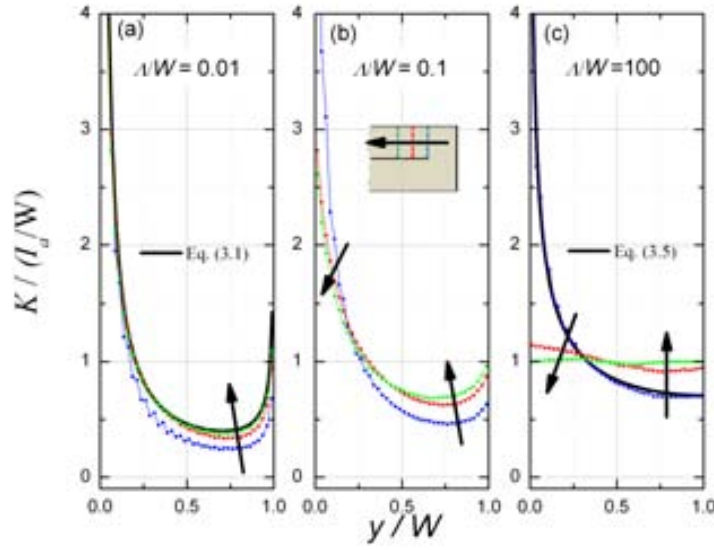
Figure 3.5: Modulus of the sheet current along lines of constant $x$ crossing the strip at distances $d = 0$ $W$ 2 and $W$ from the beginning of the $\pi$ turn [arrows indicate increasing $d$, as sketched in the inset of (b)] in the case of transport currents ($H_a = 0$) and for different values of $\Lambda$ $W$ =(a) 0 01, (b) 0 1, and (c) 100. Full thick lines show the limiting cases given by the indicated equations.

current distributions are, for the $\Lambda$ $W \propto 1$ (csh) [66] and $\Lambda$ $W \to 1$ (nrw) [67] limits,

$$K_{T,csh}^{2st}(y) = \frac{I_a}{\ln(b\ W)} \frac{W}{y\sqrt{W^2 - y^2}} \tag{3.1}$$

$$K_{T,nrw}^{2st}(y) = -\mathrm{sgn}(y) \frac{I_a}{W} \tag{3.2}$$

$$K_{M,csh}^{2st}(y) = \frac{2H_a}{\sqrt{W^2 - y^2}} \left( y + \frac{W^2}{y\ln(b\ W)} \right) \tag{3.3}$$

$$K_{M,nrw}^{2st}(y) = \frac{-\mathrm{sgn}(y)H_a}{2\Lambda}(W - 2\ y\ )\ \frac{\Lambda}{\quad}\quad 0 \tag{3.4}$$

where $\mathrm{sgn}(y)$ is the sign function, equal to $-1$ for $y < 0$ and $+1$ for $y > 0$. We observe that both in the magnetic and transport cases current is much larger at the edge close to the other strip and this enhancement is further increased by decreasing $b$. In Figs. 3.5 and 3.6 we also show in solid black lines the plots of Eqs. (3.1) and (3.3). We note that both equations are not well defined when $b = 0$. For a proper comparison with our numerical calculations, the value of $b$ has to be seen as a cut-off distance related to the sample discretization. Actually, the exact values of $b$ used in the above equations depend on the particular numerical parameters used. However, as expected, in all cases $b$    $\delta_x$ 2.

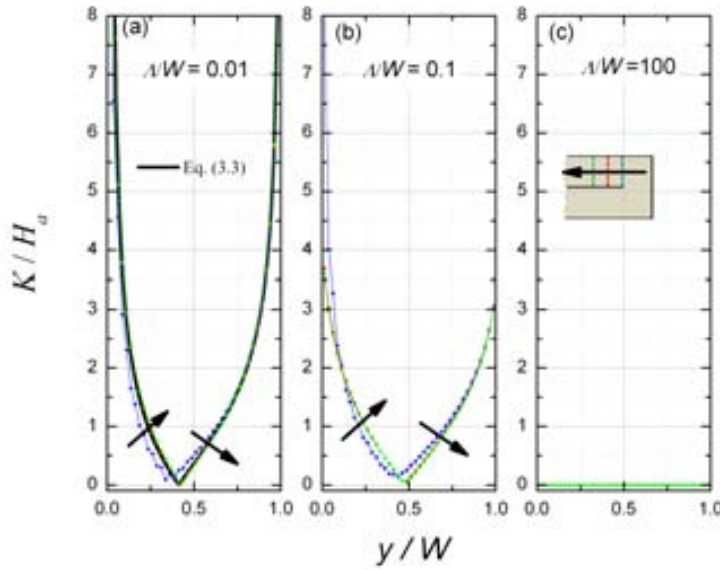For a given intermediate $\Lambda$ $W$, the distance $d$ up to which the effect of the corner

Figure 3.6: Modulus of the sheet current along lines of constant $x$ crossing the strip at distances $d = 0$ $W$ $2$ and $W$ from the beginning of the $\pi$ turn [arrows indicate increasing $d$, as sketched in the inset of (c)] in the case of magnetic currents ($I_a = 0$) and for different values of $\Lambda$ $W$ =(a) 0.01, (b) 0.1, and (c) 100. Full thick lines show the limiting cases given by the indicated equations.

over the current distribution is significant is larger in the transport case than in the magnetic case although not larger than in the $\pi$ $2$ turns. This is clearly seen in Fig. 3.5 where, for $d = W$, the current distribution is basically that of the two straight strips case (compare the results with Fig. 3.2 also for $d = W$). We also note that in the transport case, when $\Lambda$ $W \to 1$ our numerical results coincide with those in [73]. In particular, we show, in solid line in Fig.3.5c, the modulus of the sheet current in the $d = 0$ line:

$$K_{nrw}^{U-open}(d = 0) = \frac{I_a}{W} \left| \frac{1}{\sqrt{1 - e^{i\pi y/W}}} \right| \tag{3.5}$$

where indicates the modulus of the complex argument.

### 3.1.3   Other examples

Our model can be applied to any planar geometry, including holes, and any combination of applied field, current and fluxoids trapped in the sample, as described in chapter 2. In Fig. 3.7 we present some examples for illustration. Here $\Lambda = 0$ $2W$ is chosen for cases 3.7a, 3.7b, 3.7d and 3.7e and $\Lambda = 0$ $1W$ in 3.7c and 3.7f, when a hole is present, being $W$ the width of the feeding (and draining) strip. In figures 3.7b, 3.7c and 3.7e we show some cases under simultaneous applied magnetic field $H_a$ and transport
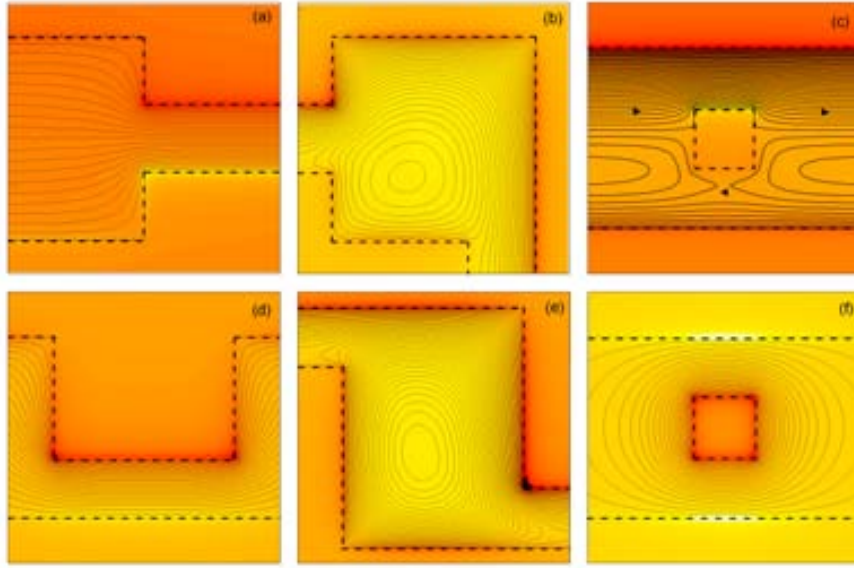
Figure 3.7: Same as in figure 3.1 but for different thin planar geometries involving turns, widenings, constrictions and holes. The strips with constrictions in the first column correspond to an applied current. In the second row cases of simultaneous applied field $H_a$ and current $I_a$ with $I_a = 1\,333 H_a W$ and $I_a = H_a W$, respectively, are considered. Figures (c) and (f) correspond to a strip with a square hole in $I_a = 0\,75 H_a W > 0$ and $N_f = 0$ at the hole in the former case, and $H_a = I_a = 0$ but $N_f = 1$ at the hole in the latter one. Color scale ranges from $-\mu_0 Ia\ W$ (light yellow) and $+\mu_0 Ia\ W$ (dark red) in (a) and (d), from 0 to $3\mu_0 H_a$ in (b) and (e), from $-\mu_0 H_a$ to $3\mu_0 H_a$ in (c) and from $-\Phi_0\ W^2$ and $5\Phi_0\ W^2$ in (f).

current $I_a$. In this case the profiles can be obtained from the linear superposition of the $I_a = 0$ and $H_a = 0$ distributions, since the response is linear on both. The strip with a hole in figure 3.7c has no net fluxoid $\Phi_f$ trapped on the hole, while in figure 3.7f some $\Phi_f = 0$ is present and $I_a = 0$ and $H_a = 0$.

In particular, we show in Figs. 3.7a and 3.7d the effect of a symmetric and asymmetric constriction in the strip, respectively. Both correspond to the application of a transport current flowing along them. We can observe in these figures how a constriction affects the currents and how far the constriction is noted. In an actual superconductor, when the local field or current overcome some particular critical values, superconducting vortices penetrate into the sample (see Sec. 3.2). Hence controlling the edge spots where these values are first achieved as well as the values for the applied fields and currents at which this happens can have important implications. We observe the maxima for the modulus of both the magnetic and the transport currents to be at the inner corners of both widenings and constrictions. However, by the simultaneous application of external fields and currents these local values can be tuned together with the position for the maxima.

Figs. 3.7b and 3.7e show more complex geometries considering applied field and current simultaneously. Here it is worth noting that the closed loops of current correspond to minima of the vortex potential (the $g(\mathbf{r})$ function [69], as noted in Sec. 2.1.3) in a bulk pinning free sample. Moreover, the minima of the magnetic field modulus $H = \mathbf{H}$ may have the ability to trap a cold atom placed on top of the sample [71]. Hence, by changing the values of the applied field and current one can tune the position where penetrating vortices or cold atoms would be trapped.

The distribution of currents within a straight strip with a centered square hole is plotted in figures 3.7c and 3.7f. In figure 3.7c the strip is subjected to a transport current and a magnetic field simultaneously, and no fluxoids are trapped in the hole. In this case, a non-symmetric distribution of current density appears since the transport and magnetic currents add (in magnitude) in one side and partially cancel each other in the other side. By modulating the applied fields and/or currents, one can control the regions where the field is enhanced or decreased. It is interesting to note that, for some values of the applied magnitudes ($I_a$ and $H_a$) we could find a region of zero current on the sides of the hole. This state is met under zero field cooling of the sample (see Sec. 1.3.1).

However, the field and current enhancement at the hole corners will eventually lead to the nucleation and leaving of some vortex or anti-vortex. When this happens some $N_f = 0$ will get trapped within the hole. For example, if a vortex nucleates at the strip outer edge and enters the hole $N_f = 1$ will take place at this hole. The same state would be reached if an anti-vortex nucleates at the hole edges and leaves the strip by one of its outer edges [63]. This state is shown in figure 3.7f. Field cooling the sample could also lead to this state. We note the high focusing of field into the hole in this case. The currents flowing around the hole sustained by the trapped fluxoid also superpose linearly with these induced by external fields and/or currents.

In all these cases we observe that the discussed accumulations and expansions of currents near inner and outer corners take place independently of whether currents bend in turns, widenings, or constrictions.

## 3.2   Vortex behavior near a sharp $\pi/2$-turn

In the present section we study the conditions for the entry as well as the behavior of the fluxoids inside a thin bulk-pinning free strip undergoing a sharp $\pi$ 2-turn. The same geometry, conditions and parameters as in section 3.1.1 are used.

The stream function $g(\mathbf{r})$ induced by the external fields $H_a$ and currents $I_a$ in a thin film can also be interpreted as the potential acting on a single vortex inside the sample [69] (see Sec. 2.1.3). In particular, $V(\mathbf{r}) = \Phi_0 g(\mathbf{r})$. This potential must thus lower the energy rapid enough to overcome the cost of suppressing superconductivity at the vortex core and to sustain the vortex currents. At this point the vortex will enter the film. The latter term includes the edge or Bean-Livingston barrier, which accounts for the interaction with the edges. Clem and Berggren [73] showed how this edge barrier
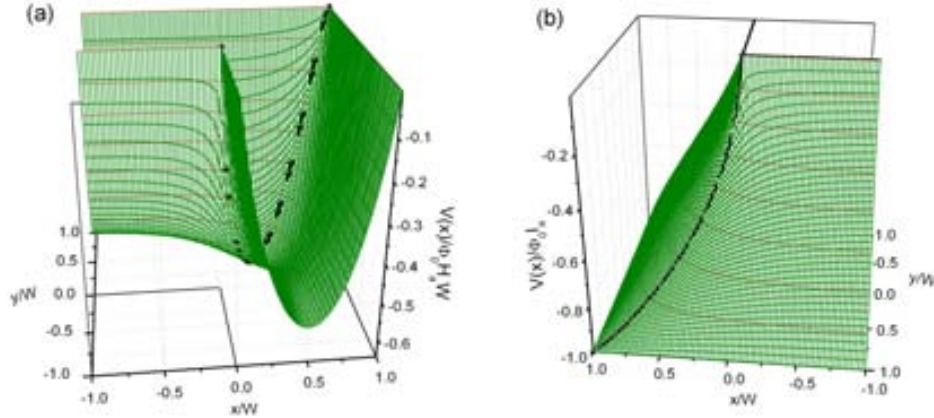
Figure 3.8: The vortex potential near the sharp $\pi$ 2-turn of a thin strip of width $W$ and $\Lambda = 0.1W$ subjected to a uniform perpendicular magnetic field $H_a$ along $+z$ (a) and a counterclockwise longitudinal transport current $I_a$ (b). The potential is normalized to the quantum fluxoid, $\Phi_0$, times $H_aW$ in (a) and to $\Phi_0$ times $I_a$ in (b). The lower left corner corresponds to the inner corner in (a) and the outer one in (b). In solid black lines we show the direction along which the edges run. Also highlighted in black dotted lines is the potential along the corner bisector, replotted with other $\Lambda/W$ values in figure 3.9.

avoids the critical current to vanish at a strip involving sharp corners where the sheet current diverges. Although they only considered strips in the narrow limit ($\Lambda \to W$), similar phenomena is expected to be present for finite $\Lambda$. In this section we neglect such edge-vortex interactions. Moreover the presence of a second vortex would distort the vortex potential. Hence, the discussion below applies only to the interaction between the first penetrating vortex and the Meissner currents induced by the applied $H_a$ and $I_a$.

We plot in figures 3.8a and 3.8b the potential the vortex would experience after penetrating the sharp $\pi$ 2-turn corner for the magnetic and transport cases, respectively. In both cases $\Lambda/W = 0.1$ is assumed. To be more precise these potentials are for the vortex and correspond to a positive magnetic field applied perpendicular to the plate and to a counterclockwise longitudinal transport current in the turn when seen from above, respectively. The contour lines of this function coincide with the current streamlines and are plotted as solid lines in figure 3.1b, and 3.1e, respectively. In these cases the slope or gradient of the potential, with modulus equal to $K$, is found to be maximum at the corner. Actually, we know it to diverge for all $\Lambda$, even for the narrow limit [73], in the transport case, and for any finite or zero $\Lambda$ in the magnetic one (see Sec. 3.1). Therefore the vortex is expected to enter the sample from the corner in all the considered cases.

This potential presents an elongated minimum along the strip length in the magnetic case. Differently, it monotonically decreases from the inner edge to the outer one in the transport case. Thus, the penetrating vortex will get trapped in the former case but will
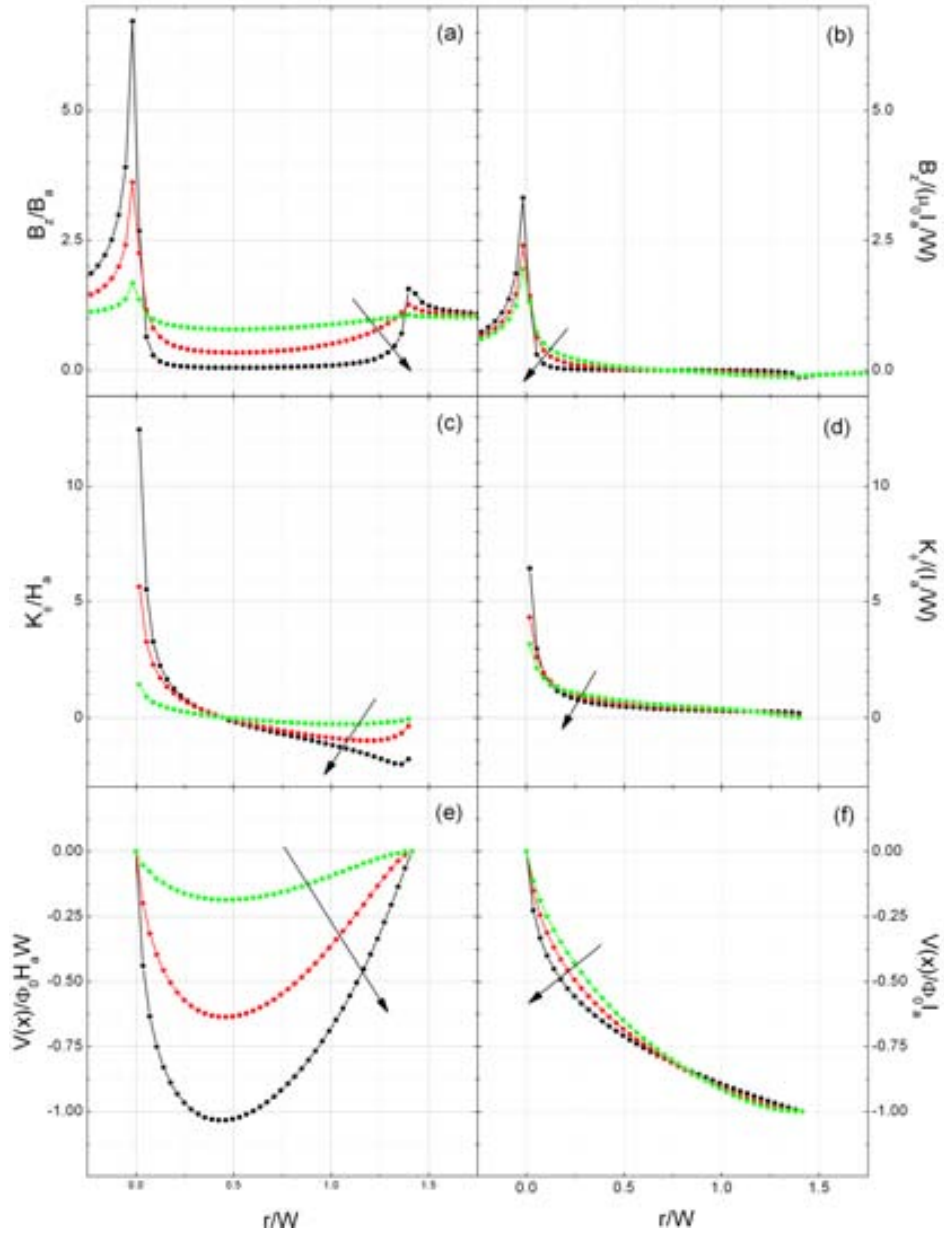
Figure 3.9: Out-of-plane magnetic induction $B_z$ (a)-(b), longitudinal sheet current $K_\phi$ (c)-(d) and vortex potential $V$ (e)-(f) for the same strip as in figure 3.8 with $\Lambda W = 0\,01\ 0\,1$ and 1 (decreasing in the arrow direction) subjected to a perpendicular uniform magnetic induction $B_a = \mu_0 H_a$ (left column) or longitudinal counterclockwise transport current $I_a$ (right column). The induction, current and potential are normalized to $B_a$, $H_a$ and $\Phi_0 H_a W$, respectively, in the magnetic case, and to $\mu_0 I_a\ W$, $I_a\ W$ and $\Phi_0 I_a$, respectively, in the transport case.
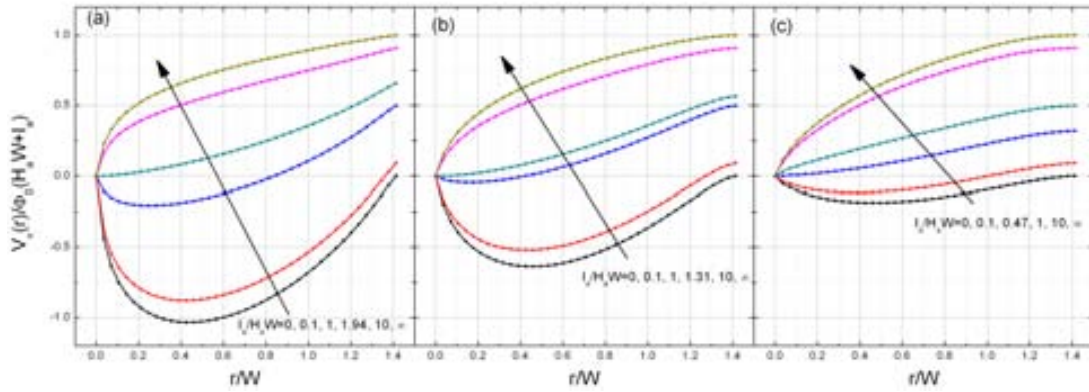
Figure 3.10: The vortex potential $V_v$ along the corner bisector for the strip with $\Lambda$ $W = 0\,01$ (a), $0\,1$ (b) and $1$ (c) subjected to a uniform perpendicular magnetic field $H_a$ and increasing a clockwise transport current $I_a$ (in the arrow direction) that partially compensates the sheet current at the inner corner. Plotted are the ratio $I_a$ $H_a W$ values $I_a$ $H_a W = 0\ 0\ 1\ 1\ 10$ and the particular one for which the potential well approximately disappears and the sheet current is totally compensated at the corner, $(I_a$ $H_a W)_{op} = 1\,94$(a), $1\,31$(b) and $0\,47$(c) for the three different $\Lambda$. The potential is normalized to the quantum fluxoid $\Phi_0$ times $H_a W + I_a$.

just transit from edge to edge in the latter one. Although this minimum runs along the whole strip length, it presents a small absolute minima placed along the corner diagonal for all values of $\Lambda$.

From the corner, where the first vortex is expected to enter, the force over the vortex points along the diagonal, which represents a path of maximum $V(\mathbf{r})$ there. This is then a non-equilibrium trajectory from which the vortex will be taken out by any small perturbation. In the transport case the vortex would then be pushed to either of the straight outer edges, where it would leave the strip. In the magnetic case, however, a rather different behavior is expected. There, the vortex would first move towards one of the straight segments but could not leave. Then it would slowly decay towards the absolute minimum. The potential slope is observed to be very small along this minimum and smaller for larger $\Lambda$.

The potential along the diagonal is highlighted with a black dotted line in the 3D $g(\mathbf{r})$ contour plots and plotted again in figures 3.9e and 3.9f for the different $\Lambda$ $W = 0\ 01\ 0\ 1$ and 1. In the same plot we show the out-of-plane magnetic induction and perpendicular current along the same line. The behavior of field and currents in this geometry was already studied in section 3.1.1.

The sheet function and sheet current are found to depend slightly on $\Lambda$ and just very near the corner significant differences arise in the diverging $\mathbf{K}$. This also produces very similar $B_z$ far from this corner. We also find the potential minima position to suffer almost no change with increasing $\Lambda$ in spite of the dramatic decay on its depth down to zero.
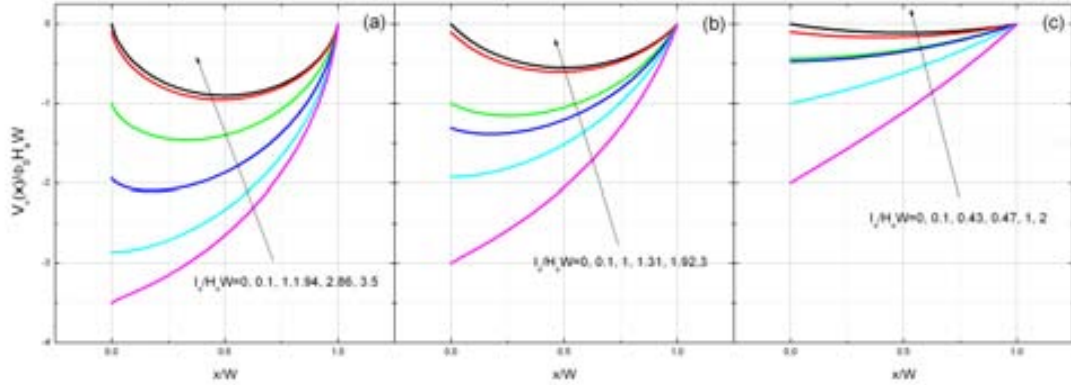
Figure 3.11: Same as in figure 3.10 but plotted across width at the straight segments far from the corner (obtained from Eqs. 1.15 and 1.18) and normalized to $\Phi_0 H_a W$ in order to see the vortex slope enhancement at the outer edge when increasing $I_a$. Here are plotted the cases with $I_a$ $H_a W = 0$ $0$ $1$ $1$ $3$, these for which the potential minimum disappears at the corner, $I_a$ $H_a W = 1$ $94$ (a), $1$ $31$ (b) and $0$ $47$ (c), and the ones for which the longitudinal straight well disappears at the inner straight edge far from the corner, $I_a$ $H_a W = 2$ $86$ (a), $1$ $92$ (b) and $0$ $43$ (c).

When a clockwise transport current is increased in a sample subjected to a positive applied field, the potential along the corner bisector evolves as shown in figure 3.10. Then the potential minimum depth and distance from the corner are found both to decrease monotonically for increasing $I_a$, together with the potential slope at the edge. This applies to any finite value for $\Lambda$ $W$. For a particular ratio between the applied field and current, $(I_a$ $H_a W)_{op}$, these three quantities vanish. At this point the sample presents no equilibrium position within its interior anymore. This value coincides with that in which transport and magnetic currents exactly cancel each other at the corner. For larger applied currents an anti-vortex will nucleate at the inner edge and transit the strip towards the outer one.

The $V(\mathbf{r})$ function along the diagonal is also shown for the cases close to $(I_a$ $H_a W)_{op}$. This quantity is found to decrease monotonically for increasing $\Lambda$, ranging from $(I_a$ $H_a W)_{op} \approx 1$ $94$ in the complete shielding limit to zero in the narrow limit, where the magnetic case potential is known to be flat.

It is also worth noting how the potential slope is nearly zero close to the outer corner for finite $\Lambda$. We cannot tell from our calculations if this tendency is restricted to much shorter distances to this corner, not observable from the grid in our numerical calculations, for very short $\Lambda$. This makes of the outer corner a bad candidate for the penetration of vortices even in this case. It is more likely for an anti-vortex to penetrate from the inner one at some $(I_a$ $H_a W) > (I_a$ $H_a W)_{op}$.

However, even before the $(I_a$ $H_a W)_{op}$ is been reached, $K$ at the corner $(K_{corner})$ will become too low for the anti-vortex to overcome the edge barrier. As Clem $et$ $al$ [74]
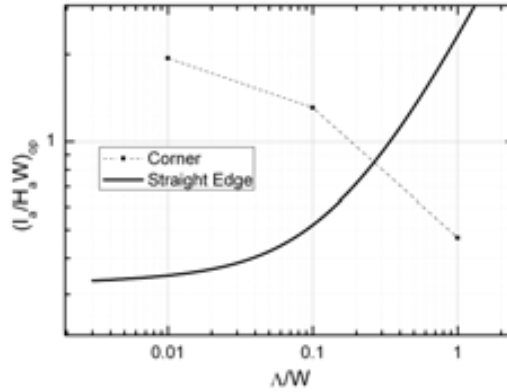
Figure 3.12: Optimum ratio between the applied current $I_a$ and the applied field $H_a$ at which transport and magnetic currents exactly compensate at the edge, normalized to strip width $W$, for the strip of figure 3.1. This quantity, $(H_a\ I_aW)_{op}$, is plotted as a function of the two-dimensional screening length to strip width ratio, $\Lambda\ W$, for the cases of currents compensating at one of the straight edges far from the turn (solid line), obtained from the solutions in figure 3.11, and that of currents compensating at the sharp inner corner (full squares).

pointed out, when magnetic and transport currents compensate each other along the inner edge, they are added at the outer one. Therefore, since the maximum $K$ is then found at the outer straight edge, a vortex is expected to penetrate first from there.

The behavior will then be determined by the distribution of currents and the vortex (or anti-vortex) potential across the width of a straight strip, which are the distributions recovered at far distances from the corner. This net vortex potential across the straight strip width is plotted in figure 3.11 for the same values of $\Lambda\ W$ as in figure 3.10, i.e. 0.01, 0.1 and 1. Here we use the $g(\mathbf{r})$ function obtained from the $\mathbf{K}$ distribution in thin straight strips with finite non zero values of $\Lambda\ W$[60] (see Eq. 1.15). These functions were found to give an error of $\sim 2\%$ near the edges of the strip, still much lower than the one committed due to the used finite mesh for the simulated samples. Note that the potential is not normalized to applied current in order to observe the enhancement of the edge potential slope at the outer edge when the applied current is increased. Similar behavior for the potential is found in this region compared to that along the corner bisector. However, in the former region the potential in the magnetic and transport cases is now symmetric and antisymmetric, respectively, with respect to the strip central line. Comparing it with figure 3.10, we can see the slight decrease in the potential well depth from the corner diagonal to the far straight segments when $I_a = 0$.

In this case the potential well is elongated along the straight strip length. However, also in this region, it disappears at some $I_a\ H_aW$ that corresponds to the value for which the local sheet current becomes zero at one of the straight edges, $(I_a\ H_aW)_{op}$. The $(I_a\ H_aW)_{op}$ value is also found to decrease with increasing $\Lambda\ W$ but at a different

rate than at the corner. In figure 3.12 we can see this quantity plotted as a function of $\Lambda/W$ for the approximated solution for a straight strip and for the values computed here at the corner. It is interesting to note the change in tendency. For fixed $H_a$ and small $\Lambda/W$, the potential minimum vanishes for lower applied $I_a$ in the straight segments. The opposite happens for large $\Lambda/W$, where lower applied currents $I_a$ are needed to remove this stable position at the corner than at the straight edge. This is the expected behavior if one realizes how in the large $\Lambda/W$ limit both the transport and magnetic currents become more uniform far from the turn. However, transport currents diverge at the inner corner but magnetic ones decrease down to zero anywhere within the strip.

## 3.3   Twin square plates

One important property that characterizes the response of magnetic samples to magnetic fields is the external susceptibility. In contrast to the internal susceptibility, which depends just on the material, the external one is also shape dependent. The reason for that is that it accounts for the demagnetizing fields, which depend on the particular geometry of the sample (see Sec. 1.3.1). In particular, the external susceptibility for a set of plates depends on the shape of the plates and also on their mutual arrangement.

Consider two identical parallel thin square planar superconducting plates, separated a distance $d$ in the vertical $z$ direction. The plates are subjected to an external uniform magnetic field applied perpendicular to the plates, $\mathbf{B}_a = \mu_0 H_a \mathbf{z}$. Their side $a$ is assumed to be much larger than its uniform thickness $t$, $a \to t$, and the 2D screening length $\Lambda$, $a \to \Lambda$. Thus, only the complete-shielding limit is considered here. Both are placed at $-a/2 \le x/y \le +a/2$, and at $|z \pm d/2| \le t/2$, where the $+$ sign stands for the upper plate and the $-$ for the lower one. Only the thickness averaged current $\mathbf{K}(\mathbf{r})$ is dealt with, and hence the behavior described below applies to arbitrary $\lambda/t$ as long as $a \propto \Lambda$ (see Sec. 1.3.1).

In samples in the complete-shielding limit subjected to external magnetic fields, induced electric currents are distributed in order to completely shield from the sample surface the out-of-plane magnetic induction, $B_z$. If more than one sample is present, then all of them interact magnetically via the fields created by their induced currents. Hence, currents within each sample will have to shield the net magnetic field, i.e. its own self-field, the external one, and that created by the other samples. This interaction can be observed from the distortion of the currents flowing on each sample when they are brought closer to each other, as well as from the behavior of the overall magnetic moment or susceptibility of the system. In particular, when the second sample is placed on top of the other each plate partially shields the external field on the other one. This interaction results in a decrease of the induced currents and susceptibility.

The $g(\mathbf{r})$ distribution induced by $H_a$ is determined by following the minimization procedure described in chapter 2. To account for the second plate the interaction between the plates is simulated as described in section 2.1.4, but the term given by equation 2.8 is not included since $\Lambda \propto a$ is assumed. We performed these calculations for one

and two thin square plates divided into a uniform mesh of $N \times N = 100 \times 100$ square identical cells of sides $\delta_x = \delta_y = a \ N$ along the $x$ and $y$ directions, respectively. For the present calculations $\Delta g \ (H_a a) = 5 \cdot 10^{-5}$ is used. The simulated separation distances between the two plates were $d \ a = 0 \ 05 \ 0 \ 1 \ 0 \ 2 \ 0 \ 5$ and $2 \ 0$ since $d \ a < \delta_x \ a$ would lead to large numerical errors and $\delta_x \ a = 1 \ N < 0 \ 01$ would need very long computing times. However, the results for $d \ a = \quad$ and $0$ can be obtained from these of one single plate by assuming a thickness of $t$ and $2t$, respectively.

Below we study both the behavior of fields and currents and of their external susceptibility $\chi_0$. The latter will be compared with results from experimental measurements.

### 3.3.1   Evolution of magnetic currents

The thickness averaged or sheet current density $\mathbf{K}(\mathbf{r})$ (see Sec. 2.1.2) is calculated from equation 2.2 from the sheet function $g(\mathbf{r})$. The out-of-plane magnetic induction in the film plane is also calculated from this sheet function using the Biot and Savart law expressed as in 2.17. As discussed above, $\mathbf{K}$ gets distributed within the sample in order to make $B_z = 0$ in the whole sample area. One consequence of this is that local currents will grow linearly with the applied magnetic field at each point of the plates and so will magnetic induction outside them. To check the accuracy of the numerical calculations, we calculate the out-of-plane magnetic induction for a single isolated plate and find it to be below 1% of $B_a \equiv \mu_0 H_a$ in the central part of the plate. The $B_z$ is also found to present some peaks in $B_z$ of $\approx 10\%$ of $B_a$ at the first cells neighbour to the edges, arising from the numerical error.

The particular current distribution that completely shields $B_z$ within a single square plate is discussed in section 1.3.1, together with its generated magnetic field. When the second plate is placed on top of the first one at a distance $d$, each of them partially shields the external field on the other one, hence reducing its induced currents. These currents will be identical on both of them since their generated field has mirror symmetry with respect to the plate plane. In figure 3.13 the $y$ component of sheet current flowing on the two plates is plotted along the $y$ axis (that bisects two of their sides) for different distances between the two plates $d \ a = 0 \ 1 \ 0 \ 5$ and $2 \ 0$, the latter very similar to that of one isolated plate. The shape of the current streamlines (not shown) is found to be just slightly distorted from that in a single plate within the studied range of $d \ a \quad [0 \ 05 \ 2 \ 0]$. However, the magnitude of these currents is observed to decrease monotonically with decreasing distance. This is because the partial shielding made by each of them on the other one is more effective as this distance is made smaller. The currents are found to decrease very slowly at large distances.

The effect of bringing them closer to each other is not the same in the different regions of the plates for different distances $d$. Actually outer currents flowing near the edges decrease slower for larger distances and much faster when the two plates are very close to each other. This will have an important effect on the plates magnetization and susceptibility, whose main contribution comes from the near-edge currents.
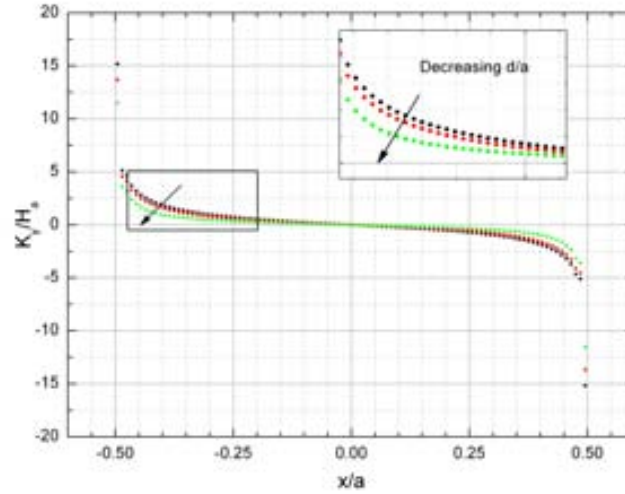
Figure 3.13: $K_y$ $H_a$ along the $y$ $a = 0$ line flowing in two identical thin square planar superconducting plates of side $a$ and thickness $t \propto a$ subjected to an applied uniform perpendicular magnetic field $H_a$ along $z$. The plates are placed in parallel with their sides aligned with the $x$ and $y$ axis (so $(x\ y)$ [$\pm a\ 2\ \pm a\ 2$] for both) and centered to the $z$ axis at $z = \pm d\ a$, thus separated by a distance $d\ a$ for different $d\ a = 2\ 0\ 0\ 5$ and $0\ 1$ (arrows show direction of decreasing $d\ a$). The induced currents are identical for the two plates. The zoom of the framed region is plot in the inset.

### 3.3.2 External susceptibility

In this section, we study the susceptibility of the two plates considered in the previous section, as a function of their distance $d$. The study will include both the numerical results obtained from the procedure described above and some experimental results.

The real samples are thin type-II YBCO plates whose ac susceptibility was measured in high alternating magnetic fields. These fields were risen up above the full penetration magnetic field defined in the critical state model (see Sec. 1.3.2), much larger than $B_{c1}$. In this section we only analyze the low-field limit of the real part of the first harmonic of the ac external susceptibility. In this limit, this term of the ac susceptibility coincides with the Meissner state external one, as discussed in section 1.3.2. The ac susceptibilities measured in the full range of fields are studied and compared with numerical results, obtained within the critical-state model approach, in section 4.3.

### Numerical results

From the $g(\mathbf{r})$ distribution within the thin plates, the magnetic moment and the magnetization of the system can be computed from equations 2.18 and 2.19, respectively. Since currents grow linearly with the applied field, so does the magnetization and the field independent external susceptibility is calculated as the slope of the $-M_z(H_a)$ curve

from equation 2.20.

The calculated susceptibilities as a function of $d/a$ are plotted in figure 3.14 and compared with the experimental ones in the short distance range, in the inset. The results are normalized to the calculated susceptibility for two distant plates, $\chi_0(d/a = \infty)$. This quantity is found to increase with increasing $d$ and to converge to the $\chi_0$ of one single plate in the limit of large $d$, $\chi_0(d/a \to \infty) \to \chi_{0,1\text{Pl}} = 0.4547\,(a/t)$. When the distance between the plates is zero, the pair of plates behaves essentially as a single one with twice its thickness, therefore its $\chi_0$ should be half that of one since $\chi_0 \propto a/t$. We use this property to get the calculated $\chi_0(d/a = 0) = 0.4547/2\,(a/t) = 0.2274\,(a/t)$. For decreasing $d/a$, $\chi_0$ is found to decrease, with an increasing slope modulus, to approach sharply the $\chi_0(d/a = 0)$ value.

**Experimental results**

The ac susceptibility was measured in three different pairs of thin square YBCO plates subjected to very large alternating magnetic fields ($H_a \to H_{c1}$) and hence presenting a highly nonlinear $M_z(H_a)$ curve (see Sec. 1.3.2). However, for very low applied fields the real part of this ac susceptibility approaches $\chi' \approx -\chi_0$ and can be compared with the susceptibility in the Meissner state.

The samples being measured were epitaxial YBCO films of nominal thickness $t$, each grown by chemical solution deposition on a $5 \times 5$ mm$^2$ (001)LaAlO$_3$ single crystal of $0.5$ mm thickness [139]. The in-plane and out-of-plane misalignment angles were approximately $0.5^\circ$. Susceptibilities were measured with a home-made high-filed ac susceptometer [140] at 77 K after zero-field cooling. Two of the samples (A and B) had a thickness $t = 0.25$ $\mu$m and a side of $a = 5$ mm. Since they were observed to have the edges partially damaged, from these and some others new samples were patterned by optical lithography to sides of 4 mm (samples C and D, the latter patterned from B). Finally a third pair of samples (E and F) of thickness $t = 0.15$ $\mu$m were also measured.

The experimental results are plotted in the inset of figure 3.14, normalized to the calculated susceptibility for two distant plates, $\chi_0(d/a = \infty)$, like the theoretical ones. Naming the face of the single crystal on which the superconducting film is deposited as the upper face and the other one as the bottom face, the upper to upper, upper to bottom, and bottom to bottom face touching overlapped A and B correspond to $d/a = 0$, $0.1$ and $0.2$, respectively.

The observed general trends described for the numerical results also apply to the experimental ones. However, some differences are observed. For example, we can clearly observe that the $\chi_0(d = 0)$ calculated as mentioned above underestimates the measured value for the three pairs of samples. As discussed in [141] this could be due to a mutual shift along the $xy$ plane in all three measurements, since the pairs of plates are hard to be exactly overlapped. However, the shift could not be much larger than $0.2$ mm and this would only give an increase in $\chi_0$ of about 2% [77], much lower than the observed one. Another possible reason for the discrepancy is the real distance between the plates
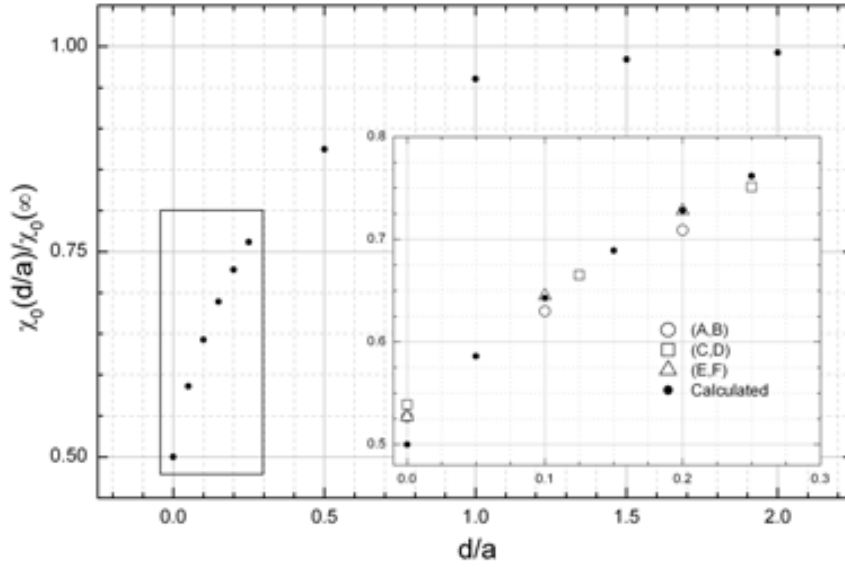
Figure 3.14: Calculated (full circles) and measured (open symbols in inset) effective suscepti-
bilities $\chi_0$ for the set of the same two plates as in figure 3.13 as a function of separation distance
between the two plates, $d\ a$. Both the measured and calulated $\chi_0$ are normalized to the calcu-
lated value for very distant plates $d\ a \to 1$, corresponding to that of one single plate (see text).
Plotted are the experimental results for the three different pairs of samples A and B (circles), C
and D (squares), and E and F (triangles).

to be of $d\ a \approx 0\ 001$, due to its finite thickness. In that case a quick increase of $\chi_0$
with increasing distance should take place at very small distances. Calculating the $\chi_0$
for so small $d\ a$ would require long computing times, since $d\ a > 1\ N$ is needed to have
accurate results. Therefore, the particular behaviour in this region still remains an open
question.

Apart from this over-large measured $\chi_0(d = 0)$ we also observe the measured $\chi_0$ for
the overlapped A and B samples to be systematically lower at finite $d\ a = 0\ 1$ and $0\ 2$.
Since the ac susceptometer was calibrated by C and D and the measured $\chi_0(\ )$ of E
and F is merely about 1% smaller than the calculated value, the measured $\chi_0(\ )$ is
practically the same as the calculated one for the case of C and D or E and F. Thus,
the difference between the $\chi_0(d\ a)$ at $d\ a = 0\ 1$ and $0\ 2$ of samples A and B and the
calculated ones should be a consequence of over-low experimental $\chi_0(\ )$.

# Magnetic response of thin films in the critical state

In chapter 3 we simulated high-$\kappa$ type-II superconducting thin planar plates and strips of different geometries in the Meissner state. There we only considered the Meissner currents present before the penetration of vortices within the sample. Only in section 3.2 the interaction of an entering vortex with these currents was studied under the assumption of negligible bulk pinning.

Here we also consider thin superconducting films, but in this case in the critical state. In this regime, in general, the length-scale is assumed very different to the one considered in chapter 3 and also the involved fields are much higher (see Sec. 1.3.2). Moreover, this state is reached when a strong bulk pinning is present. More precisely the in-plane sample dimensions $W$ are assumed much larger than the Pearl length $\Lambda$, $W \to \Lambda$, and the local fields $H_i$ are comprised within the range $H_{c1} \propto H_i < H_{c2}$ with respect to $H_{c1}$ and $H_{c2}$, the lower and upper critical fields, respectively. Therefore, even for small $H_i$ many vortices are present and we only deal with quantities averaged over several intervortex spacings.

The chapter is organized as follows: first we study in section 4.1 the distribution of currents within thin planar superconducting strips of different shapes and for different sequences of applied magnetic fields and transport currents. Then in section 4.2 we analyze the effect of the history-dependent current profiles in the critical current $I_c$, as a function of applied field $H_a$, for the particular case of a straight strip with some pierced antidots. Finally, the study of the current distribution, sample magnetization and external susceptibility made in section 3.3 for two twin plates, is extended in section 4.3 to account for the new phenomena taking place in the critical state.

## 4.1   Response of strips of different geometries to applied transport currents and magnetic fields

In this section we describe the penetration of fields and currents in the critical state when a transport current $I_a$, a magnetic field $H_a$, or both, are applied to the thin sample of uniform thickness $t$ and current density $J_c$. We consider different geometries and sequences of $I_a$ and $H_a$. Then, with this study we extend the previous ones considering situations under applied current for the simple straight strip geometry [142, 57] and the ones considering only the response to applied magnetic fields in different 2D thin geometries (see Sec. 1.3.2). The two geometries we simulate are these of a thin straight strip with a narrow perpendicular slit starting from one edge and that of a straight strip with straight edges that turns sharply, forming a $\pi$ 2 radiants angle (see Fig. 4.1).

The magnetic case [68, 76, 102, 103, 104], in which a uniform magnetic field is applied perpendicular to the strip, is first reviewed for the two different geometries and only for the case of $H_a \to K_c = J_c t$. Although the results we present in this part are well known or can be easily derived from these for other similar geometries (see Sec. 1.3.2), we consider they will help us understand the behavior observed in the following sections. Then we study the transport case of longitudinal $I_a$ applied to the strips. Applied current is increased up to the corresponding saturation value for each strip and then decreased back to zero. In the following part, different sequences of increasing $I_a$ first and then $H_a$, and vice versa, are also considered for the same geometries. Some general conclusions about the current penetration that apply to any strip geometry and sequence of applied field and current are given there. Finally, at the end of the section some of the previously discussed cases are studied within a straight strip that widens sharply.

The thin superconducting strips are modeled following the approach described in chapter 2 and accounting for the constraint on the allowed **K** values and also for the hysteresis present in samples in the critical state (see Sec. 2.1.5). The samples are discretized by dividing them in square cells of side $\delta_x = W_m$ 40, where $W_m$ is the strip width at narrowest segments, and $\Delta g = 5 \cdot 10^{-4} I_a$ and $\Delta g = 5 \cdot 10^{-4} H_a W$ are used for the transport and the magnetic cases, respectively.

### 4.1.1   Magnetic case

The slitted strip is assumed to be very long (along $x$), of width $W$ and with a slit of length $W_s$, which is perpendicular to the strip edges and starts from one of them. The turning strip is also long, of width $W$ and, at some point, turns sharply forming a $\pi$ 2 radians angle.

**Geometrical interpretation of the critical current streamlines shape**   The well known trends regarding the appearance of the different critical regions and critical current streamlines shape in the magnetic case, can be understood as follows. First
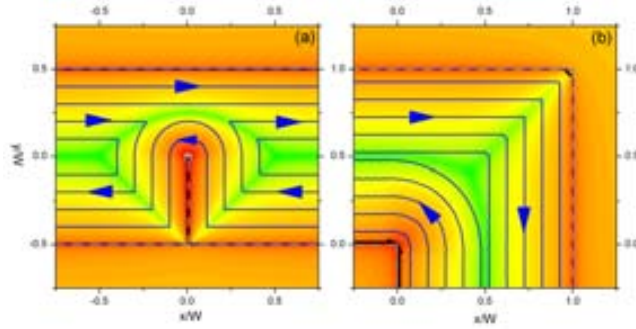
Figure 4.1: Current stream lines (arrows show direction of current flow) in thin planar super-conducting strips of width $W$, thickness $t$ and critical current $J_c$ subjected to a large positive perpendicular magnetic field $H_a = 1\,5K_c \to K_c = J_c t$, above that of full saturation, when the strip either (a) contains a straight narrow slit of length $W_s = W\,2$ that starts from one of the strip edges and is perpendicular to it or (b) undergoes a sharp $\pi\,2$ turn at some point. Colors represent the intensity of the out-of-plane magnetic induction $B_z$ at the strip surface, ranging from $0\,0$ (green) to $+2\,5\mu_0 K_c$ (red). Bold lines mark the critical region inner boundaries or flux fronts (FF) while dark gray dashed lines delimit the sample perimeter.

we must note that the critical currents (the ones of maximum modulus, $\mathbf{K} = K_c$) follow line paths whose points keep a uniform distance to the closest edge. Thus, at regions where some edge is closest than any other these currents will flow parallel to it. Moreover, there might be some regions which are the locus occupied by points of equal distance to two edges. In this case the behavior will be qualitatively different depending on whether the two edges meet at a corner forming an angle smaller (convex corner) or larger (concave corner) than $\pi$. In the former case this locus is a line, named $d^+$-line, along which current streamlines must bend sharply (see Sec. 1.3.2). Logarithmic infinities in the out-of-plane magnetic field are observed at these lines [103]. Differently, near a concave corner the points of equal distance to the two meeting edges occupy a given area, which is the one subtended by the two edge extensions. In that region the closest edge point is the corner where the two edges meet. Within this area the current streamlines must follow circular paths in order to keep a uniform distance from the edge. As pointed out by Brandt [76], vortices move perpendicular to the critical current streamlines. This means that vortices must always enter perpendicularly to the sample edges and they can never cross a $d^+$-line. Moreover, it is worth noting that at a sharp concave corner the vortex transit is much higher, since all the vortices filling the area with rounded critical currents must enter from that corner.

Some of theses trends can be observed within the geometries we consider here. In particular, we show in figure 4.1 the critical currents distribution at full saturation, i.e. a very large positive magnetic field is been applied perpendicular to the samples, starting from the virgin state. Indeed, we observe how straight currents flow far from the widenings, turns and slits and how they bend sharply along some formed $d^+$-lines near these geometric elements. Moreover, currents follow circular paths around the concave

corners. In this case the whole sample can be fully saturated with critical currents. As a result, the $d^+$-lines can develop but just asymptotically, when $H_a \to K_c$.

In particular we observe straight $d^+$-lines extending along the convex corners bisector. Also curved $d^+$-lines are present in this state near point defects, as is the case of the tip of a slit. The latter were shown to follow a parabolic shape [143, 104].

In the turning strip, for example, we observe circular critical currents flowing near the concave corner, while a $d^+$-line is formed, along the corner bisector, from the outer convex corner. Up to a distance $W/2$ from the inner and the outer corner, the circular and the straight sharply-bending currents come from infinity. However, in the region near the corner the strip is widened. The remaining central region, equidistant to the inner and outer edges, is filled with closed loops of current. These currents are also circular at points closer to the inner corner and turn sharply at points closer to one of the outer edges. Thus, both circular currents and the $d^+$-line extend along the corner angle bisector down to the central point at a distance $\sqrt{2}W$ from both of the two corners.

In the strip with a slit, a straight $d^+$-line develops along both of the two corner bisectors by the two slit sides. These $d^+$-lines extend up to the strip central and longitudinal line, $y = W/2$. The parabolic $d^+$-line links these two end points of the straight $d^+$-lines and crosses the point $(x, y) = (0, \frac{3}{4}W)$. This point is at the slit extension line and is equidistant to the slit tip and the opposite strip edge. Currents flowing between these three $d^+$-lines are, circular in the upper strip half and centered in the slit tip, and straight and vertical in the lower half. The remaining currents outside this region are straight and horizontal, along the strip longitudinal direction.

### 4.1.2   Transport case

The behavior of currents and fields induced within a thin straight strip of uniform width $W$ in the critical state for the transport case has been solved in the literature and was described in section 1.3.2. There we showed how the currents, longitudinally symmetric along the strip direction, evolve when increasing $I_a$. In particular we could see how when the critical current $I_c$ of the strip ($I_c = K_c W$) was reached, the whole strip surface was filled with critical currents of modulus $K_c$.

Here we consider the same case of applied transport current but in this case for the two same geometries from the previous section, thus breaking the longitudinal symmetry. Also in these geometries, if we start from a virgin sample, when a current $I_a$ is fed into the strip there will appear a critical region penetrating from the strip edges according to the critical-state model. However, if the cross section normal to applied current (or equivalently the width in our case, since uniform $t$ is always assumed) is not uniform along the strip length, its own $I_c$ is reached when the narrowest segments become fully saturated with critical currents $K_c$. For larger $I_a$ vortices get depinned and transit across the strip width at these regions. Thus, the critical-state model breaks down. At this point, some flux-free regions remain at the wider parts of the sample.

**Strip with a slit**

Consider now the strip with a slit of the previous section (see Fig. 4.2). We fix the origin of coordinates at the slit $x$-position and at the center of the strip [the slit goes from $(0 \ -W \ 2)$ to $(0 \ -W \ 2 + W_s)$].

When feeding a transport current $I_a$ to the strip in the virgin state the critical regions will penetrate the sample from all of its edges, including these by the slit. This critical region will penetrate deeper around the slit tip and towards the opposite strip edge. It will not penetrate at all from the convex corners where the slit meets the strip edge, just like in the magnetic case (see Sec. 1.3.2). The result is a droplet shape critical region boundary or flux front (FF) growing towards the opposite edge as $I_a$ increases. The critical regions penetrate from the other straight edges as well. The depth of penetration of the FF at the edges by the slit sides decreases monotonically with decreasing distance from the convex corner. At the opposite straight slit-free edge, a slightly deeper penetration is observed near the spot which is closest to the slit.
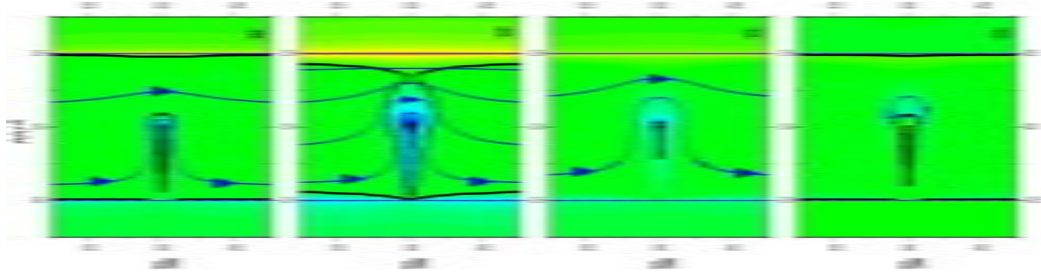


Figure 4.2: Same as in figure 4.1a when no magnetic field is applied but a longitudinal transport current $I_a$ is increased through $0 \ 25K_cW$ (a) up to the strip saturation value $I_{c,s} = 0 \ 50K_cW$ (b) and then decreased back through $0 \ 25K_cW$ (c) again and down to 0 (d). Here out of plane magnetic induction ranges from $-1 \ 0\mu_0 K_c$ (dark blue) through 0 (green) and up to $+1 \ 0\mu_0 K_c$ (red).

These trends in the current penetration can be understood from the same ideas discussed in [144] for the Meissner currents for the particular case of short $\Lambda$ (see Sec. 3.1). Since the penetrating currents try to shield the total field, convex shaped currents can exert an effective shielding with low magnitude. This explains the little penetration of the critical region near these corners, strictly zero at the sharp ones present in this geometry. However, concave shaped currents do a less effective shielding in the interior of the sample. Thus, they must be larger in magnitude in order to keep a zero magnetic field in the innermost regions. The difference with respect to the Meissner state case, is that here **K** is bounded. Then, currents penetrate deeper instead of becoming larger near concave corners.

When the two FFs penetrating from opposite edges of the strip meet, the minimum transversal width allowed for currents to pass is fully saturated with maximum sheet current $K_c$. This maximum current intensity is $I_{c,s} = K_c(W - W_s)$ for this particular geometry. At this point some subcritical flux-free regions remain at the wider segments
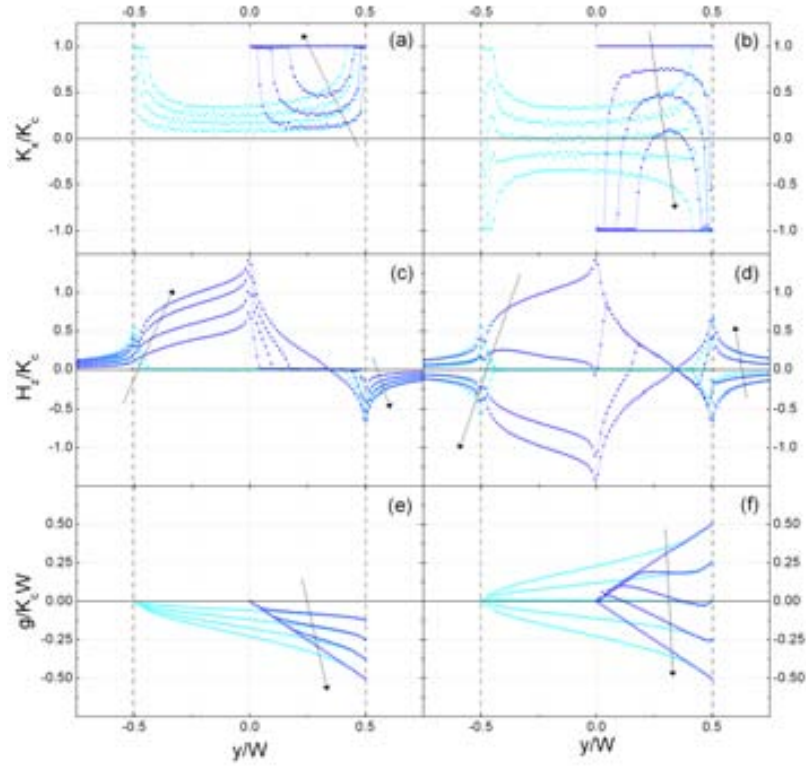
Figure 4.3: Longitudinal current (top row), out-of-plane field (mid row) and $g$ profiles (bottom row), normalized to $K_c$, $K_c$ and $K_cW$, respectively, plotted along the slit line extension (dark blue) and along the parallel to slit line at a distance $d = W$ from it (light blue), for the strip with a slit of figure 4.1a subjected to an increasing (in the arrow direction) applied current (left column) up to the critical value $I_{c,s} = 0\,5K_cW$ and then decreasing (in the arrow direction) this current (right column) down to $-I_{c,s}$ after the reach of $I_{c,s}$. Vertical dashed dark gray lines delimit the strip edges positions. Oscillations are due to direct numerical derivation.

by the slit sides.

In figure 4.2 we show the current distribution for different applied currents, starting from a virgin state sample and increasing the current (Fig. 4.2a) up to the maximum allowed $I_{c,s}$ (Fig. 4.2b) and then decreasing back (Fig. 4.2c) to zero (remanence, Fig. 4.2d).

Although the FF shape and its rate of penetration are very different, the shape of the stream lines of critical currents is the same for the magnetic and the transport cases, following the same principles discussed in section 4.1.1. The reason for this is that the necessary field distribution to be shielded is very different for the two cases: in the magnetic case it includes the external uniform applied field whereas in the transport case only the currents self-fields are present. However, the shape of the critical current stream lines in the critical state model is not given by the field distribution but just from the geometrical principle of currents following paths of constant distance to a particular sample edge.

The tip of the slit is one of the edge spots that gets surrounded by circular critical

currents and thus where a high vortex transit takes place. In particular all the vortices filling the region of curved circular stream lines must enter from there.

In the magnetic case, the $d^+$-lines that develop along convex corner bisectors are known to be well defined just asymptotically and to be the last region to become saturated. This is why in the transport case such $d^+$-lines will never develop when the strip cross section is not uniform. This is precisely what we observe in figure 4.2c, where $I_{c,s}$ is already been reached.

In figure 4.3 we show the calculated values for $g$, the $x$ component of the sheet current and the out-of-plane component (evaluated at $z = 0$) of the field along the line containing the slit and the one parallel to it at a distance $d = W$ from it, for different values of $I_a$ increasing from zero to $I_{c,s}$ and then decreasing down to zero. We can see that the distributions are not symmetric with respect to the center of the aperture, as expected, because the slit breaks the $y$-symmetry.

Another interesting fact comes from the square-root dependence of the penetration depth of the critical regions as a function of $I_a$ $I_c$, in strips with a critical current $I_c$ (see Eq. 1.38). This is that a relatively small slit can produce a large distortion in the flux front far from it. Indeed, when the maximum current has been applied, far from the slit the critical region occupies a fraction $\alpha = ((W - 2b)\ W) = 1 - \sqrt{\frac{2Ws}{W} - \frac{Ws^2}{W^2}}$ of the total cross section of the strip. For small slits $\alpha\quad 1 - \quad\overline{2}\sqrt{W_s\ W}$. This indicates that, for example, when the slit width is just 10% of the total strip width, far from the slit just about 56% of the cross-section width is filled with critical currents at $I_{c,s}$ (in the case of the Fig. 4.2, $W_s\ W = 1\ 2$ and $\alpha\quad 0\ 13$).

When reversing current, just like in the magnetic case, new currents of opposite sign penetrate from both of the two edges. Because of the slow rate of penetration of the critical region with changing $I_a$, this region is very narrow when $I_a = 0$ is reached in the current reversal (remanence). At this point, at each cross section there should be as much positive currents as negative ones, producing some closed loops of current, as we observe near the tip of the slit in figure 4.2d (in the figure most of the loops would eventually close very far from the slit). When $-I_c$ is reached (not shown) the same distribution present at $+I_c$ takes place, but currents flow in the opposite direction.

The high number of penetrating vortices at the slit, and particularly at its end, is also expected from the increase in the magnetic field in its immediacies. Actually, the magnetic field along the slit arises mainly from the current that surrounds it. When they have critical value, it can be seen that the field diverges logarithmically in the slit, as in the border of a slit-free strip. Nonetheless, now the contribution comes from both sides of the strip and thus, the field is doubled. At the end of the slit the field has its maximum value because of the rounding currents. This increase along slits was also calculated in [69] with magnetic currents in the Meissner state.

### $\pi$ 2-Turn

We now consider the turning strip of width $W$ as in section 4.1.1. The current and field distributions for different applied currents are shown in Fig. 4.4.
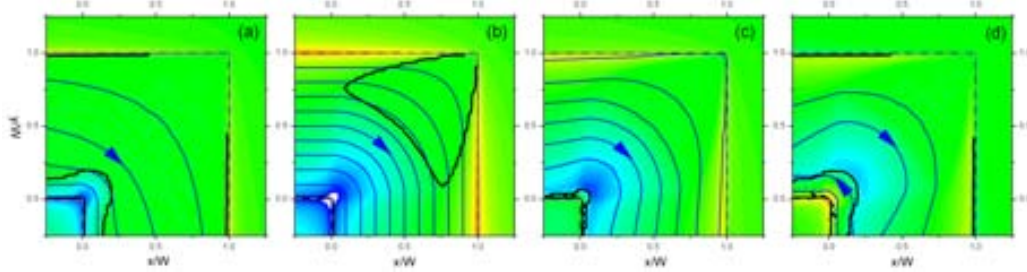


Figure 4.4: Same as in figure 4.2 but for the turning strip of width $W$ that undergoes a sharp $\pi$ 2 turn at some point of its length subjected to increasing clockwise applied currents of values $I_a = 0\,5K_cW$ (a) and the critical one $I_{c,t} = 1\,0K_cW$ (b) and then decreasing from the latter back through $0\,50K_cW$ (c) and down to 0 (d). Regions in light gray are out of range.

For the same reasons as in the case described above, here we observe the FF to penetrate deeper from the inner concave corner along the corner angle bisector. Differently, at the outer straight edges, the FF penetration depth is found to decrease monotonically along the edge with decreasing distance from the convex corner. Again, like in the magnetic case, the critical region does not penetrate at all from this corner. Also in this case critical currents flow straight and parallel to the closest edge anywhere but at the region near the concave corner, where they must follow circular paths.

To understand the behavior near the strip full saturation current, $I_{c,t} = K_cW$, we must realize that the strip is widened at the corner region. In particular it reaches a maximum value $W_{max} = \overline{\phantom{2}}2W$ along the bisector of the corner angle. Then, when the strip straight segments become fully saturated with $K_c$, this region is not so. The result is that the critical regions penetrating from opposite parallel straight edges meet before the $d^+$-line can develop along the bisector of the outer convex corner angle. An arrow shaped flux free-region boundary appears at $I_{c,t}$.

The $\pi$ 2-turn considered here appears to us as the simplest strip geometry involving sharp convex corners. Therefore, we expect $d^+$-lines only to be formed by the application of perpendicular magnetic fields (assimptotically) but never from an applied transport current.

The presence of a flux-free region at $I_{c,t}$ and the low $K$ near the outer convex corner are more clearly seen in Fig. 4.5. There we plot, along the segment connecting the two corners of the turn, the $g$ function, the perpendicular component of the current, and the out-of-plane component of the magnetic field at $z = 0$. We see how the critical region grows from the concave corner towards the opposite strip edge up to some depth and, from that point to the other corner the field is shielded from the sample. In Fig. 4.6 we have plotted the calculated flux-front penetration depth (defining a distance $r_p$ from
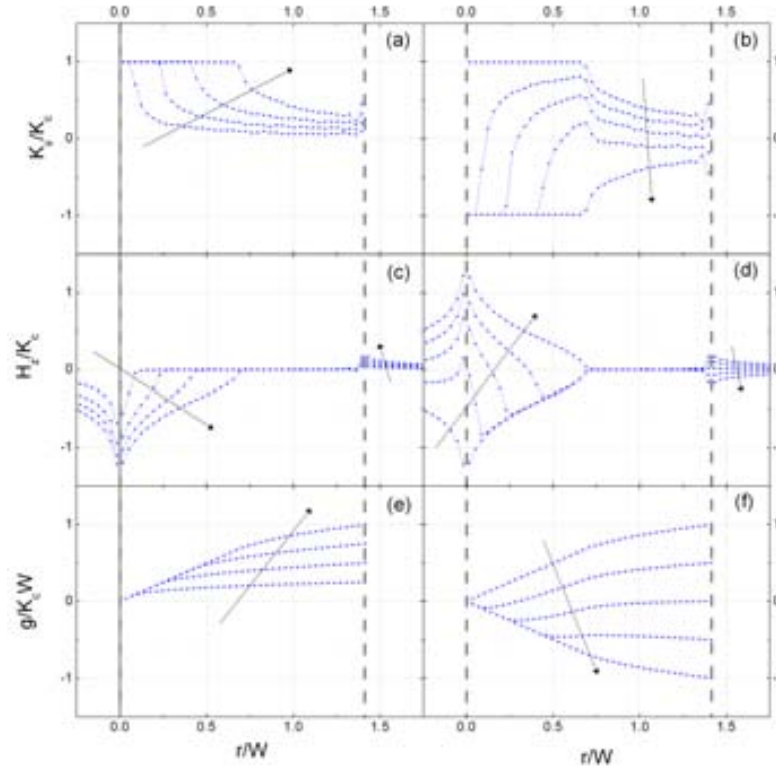
Figure 4.5: Longitudinal current(top row), out-of-plane magnetic field (mid row) and $g$ profiles (bottom row), normalized to $K_c$, $K_c$ and $K_cW$, respectively, along the sharp corner angle bisecting line of the turning strip in figure 4.4 subjected to an increasing (in the arrow direction) clockwise applied current (left column) up to the saturation value $I_{c,t} = K_cW$ and then decreasing (in the arrow direction) this current (right column) down to $-I_{c,t}$. The shown current component is the one flowing perpendicular to the turning angle bisector and is defined as positive in the clockwise direction. Vertical dashed dark gray lines delimit the strip edges at the inner and outer corners.

the inner corner) as a function of $I_a$, along the corner angle bisector and compare it with that of a straight strip along a transversal line crossing the strip (defining $x_p$ as the distance from the inner side). This depth cannot be easily predicted, since it depends on the particular shape of currents in the subcritical flux-free region. Note that for the straight strip, the two flux fronts penetrating from the two sides of the strip meet at the center of the strip for $I_a = K_cW$, whereas for the $\pi$ 2-turn strip, there is no penetration from the outer corner and thus the flux fronts cannot meet. Intermediate values for the FF penetration depths from both of the two edges would be observed along straight lines connecting the opposite edges and running between the two we consider here.

When reversing $I_a$ the trends are very similar to the ones already described above for the strip with a slit. For example we note that here closed loops of current also develop near the sharp concave corner at the remanence, while most of them close far from the turn.
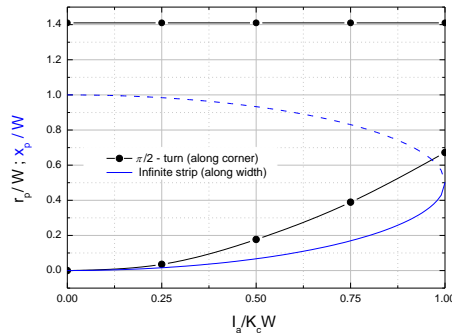
Figure 4.6: Position of the flux fronts (FF) entering from the two sides of a long straight strip normalized to the strip width $W$ (blue lines) and the same flux-front positions from the inner (bottom black line) and outer (top black line) corners of the sharp turning strip of figure 4.4. The positions along the diagonal from corner to corner are normalized to the diagonal length $\sqrt{2}W$.

### 4.1.3  Application of a transport current and a subsequent magnetic field

Up to now, we have considered either a perpendicular magnetic field, in section 4.1.1, or a given transport current, in section 4.1.2, applied over a strip of different geometries. The calculation method can also be successfully applied if field and current are both applied. Naturally, in this situation a a great variety of different sequences of applied field $H_a$ and current $I_a$ can be studied (see Sec. 1.3.2).

Our numerical method can manage to calculate all these cases as far as the critical-state assumptions remain valid and, in particular, as far as quasi static situation (slow variation of applied field and current) is considered.

These different sequences of applied fields and currents in the critical state were studied in detail just for the case of a straight strip of uniform width $W$ [58, 57]. A very rich set of phenomena could be observed there. In spite of this, whenever the sample critical transport current $I_c$, was applied, currents with $\mathbf{K} = K_c$ flowing in the direction of applied current filled the whole sample. Therefore, all the information from previously attained states was completely erased. Moreover, at this point the distribution became insensitive to any change of the external applied field. We show here how this is no longer the case when the strip width is not uniform along its length. Even when the sample $I_c$ is applied, we will see how in this case the critical current distribution strongly depends on the sequence by means of which the final state is been reached. In particular we shall consider here that the sample is saturated by applying a critical current $I_c$ and, after this, a perpendicular field is applied in the two possible directions.

We will thus only describe the behavior of critical currents, specially in the limit $H_a \to K_c$. Then, we will not discuss the particular shape of the flux front nor of the sub-critical currents in the flux-frozen regions.
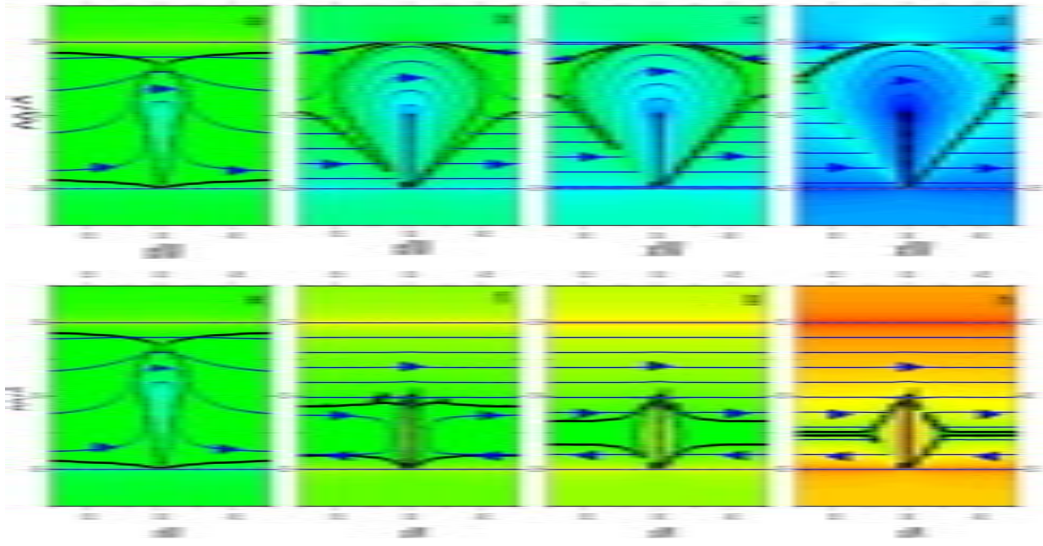
Figure 4.7: Same as in figure 4.1a for the strip with a slit subjected to its critical transport current $I_{c,s} = 0\,5K_cW$ and then also a magnetic field of modulus $H_a$ $K_c$ with increasing values $0\,00$ $0\,50$ $0\,75$ and $1\,50$ (increasing from left to right), up to the strip full saturation, applied in the negative (top row) or the positive (bottom row) out-of-plane $z$ directions. Here the out-of-plane magnetic induction $B_z$ ranges from $-2\,5\mu_0K_c$ (blue) through $0\,0$ (green) and up to $+2\,5\mu_0K_c$ (red). Asymmetries in the FF solid black thick lines are due to numerical error.

## Strip with a narrow slit

Consider a strip with a slit over which a transport current has been applied up to saturation. The current distribution has been described in section 4.1.2. After the current $I_{c,s}$ has been reached we apply a magnetic field along either of the two directions perpendicular to the strip plane. The new induced currents will tend to shield any variation of the total field in the strip region.

In Fig. 4.7 we see how, starting from the same current distribution at $I_c = I_{c,s}$, the newly induced current is completely different for different signs of applied field $H_a$. For the two signs of $H_a$, however, critical currents fill the whole sample surface when $H_a \to K_c$ is reached. This is because a positive $H_a$ makes the critical region that entered from the upper edge to grow towards the lower one, while the lower currents are gradually erased. On the contrary, a negative field makes the critical region from the lower edge to grow towards the upper one.

Then, when increasing the applied field in the positive direction, the initial droplet-shaped critical region grows in width while a $d^+$-line forms along the convex corners bisector by the slit sides. This $d^+$-line is only assimptotically formed for large applied fields. When the applied field is large enough, the rounded part of the critical region reaches the other side of the strip, differently to the case of large applied field without previous transport current. There is some current that returns back before reaching the slit region. Far from the slit, thus, and for large applied field, the flux-free region

reduces to a horizontal line located at $y = (W - W_s)\,2$, provided that the net current crossing the strip has to be $I_{c,s} = (W - W_s)K_c$.

On the other hand, when the applied field is negative, the initial droplet-shaped critical region tends to disappear and the critical region close to the slit-free border tends to increase until it reaches the slit. Interestingly, in the saturation situation, the current distribution is exactly the same as that for three unconnected strips: one of them infinite and of width $W - W_s$ carrying all the transport current $I_{c,s}$, and two of them semi infinite of width $W_s$, with a current distribution equivalent to that completely saturated with large perpendicular magnetic field and without net current crossing them. In the lower part, 2 $d^+$-lines forming a $\pi\,4$ angle with the slit, like in a square or rectangular plate, develop by each slit side. For distances from the slit larger than $W_s\,2$ along the strip longitudinal direction, the two flux fronts meet at the lines $y = -(W - W_s)\,2$.

Thus, the final state is the result of currents following the principle of constant distance from an edge. At the narrowest segments, the entire critical region from edge to edge is filled with currents following the same edge. This edge is the lower one for the former case with positive applied $H_a$ and the upper one when the applied $H_a$ is negative. This proves how one can control, through the applied field sign, which of the strip edges is the one followed by the transport critical currents at the narrowest strip segments when $I_a = I_{c,s}$ is fed.

Once $H_a \to K_c$ is reached, we could reverse it up to very large values again but with opposite sign. In that case the final state would be the same one as if this last $H_a$ variation was applied directly after the reach of $I_a = I_{c,s}$. If the field is reversed back again to $H_a \to K_c$, the same state present previously for the same value of $H_a$ would be achieved.

### $\pi\,2$-turn

Consider now the strip with a $\pi\,2$-turn over which a saturation current $I_a = K_c W$ has been applied. As discussed in section 4.1.2, currents turn the corner following circular paths close to the inner corner and keeping a zero flux region close to the outer one (see Fig. 4.8a and Fig. 4.8e). Applying the same principles described above, the application of an external perpendicular magnetic field $H_a$ leads to two very different behavior depending on the sign of this field.

In this geometry, an interesting effect can be observed in the close-to-corner region. When applying the field in one direction the flux-free region shrinks and the circular-currents region expands (see Fig. 4.8). At high enough applied field, the circular current region reaches its maximum extent. At this point, the outermost circular current stream line has a radius $W$. If the field is applied in the opposite direction, the circular-current region shrinks being substituted by straight currents. When the applied field is large enough, these currents form a $d^+$-line going from corner to corner. All current stream lines are straight and bend sharply at the $d^+$-line.

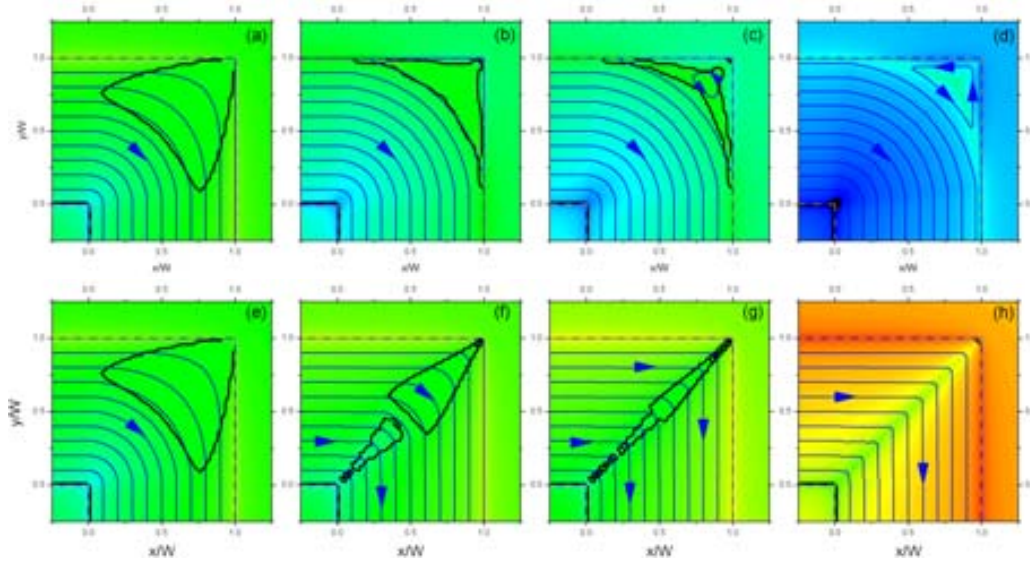This behavior arises from the need of the currents produced by the application of a

Figure 4.8: Same as in figure 4.7 but with the turning strip subjected to the same values of perpendicular magnetic field applied after the reach of its own critical transport current $I_{c,t} = K_c W$. Out-of-plane magnetic indution ranges from $-2\,5\mu_0 K_c$ (dark blue) to $+2\,5\mu_0 K_c$ (red). In (d) the applied field is $H_a\ K_c = 2\,0$ since the full saturation was not reached yet at $1\,5$, and the out-of-plane magnetic induction ranges from $-3\,0K_c$ to $+3\,0K_c$. Colored in black are regions below the corresponding $B_z$ range.

magnetic field to shield the flux-free region. Again, this difference is possible thanks to the widening present near the corner (the width is $\overline{2}W$ from corner to corner). If the outer corner was rounded so that the strip width was uniform and equal to $W$ in spite of turning, then the current distribution would be independent on the applied field, as well as on the sequence of external fields and currents, whenever $I_{c,t}$ was applied.

### 4.1.4 Application of a magnetic field and a subsequent transport current

Here we consider the cases in which the magnetic field $H_a$ is increased up to the saturation, $H_a \to K_c$, before the application of a transport current $I_a$. The applied current is gradually increased up to the saturation value, $I_c$, of the corresponding geometry, with either of the two polarities.

**Strip with a slit**

Consider now that we apply $H_a \to K_c$ to the strip with a slit of length $W_s = W\ 2$. The present magnetic currents flow in the positive $x$ direction by the upper straight edge and in the negative one by the lower edge with the slit. If then $I_a$ is applied in the negative direction, currents will penetrate and distribute themselves within the upper half. The currents flowing by the lower half and turning around the slit tip will suffer
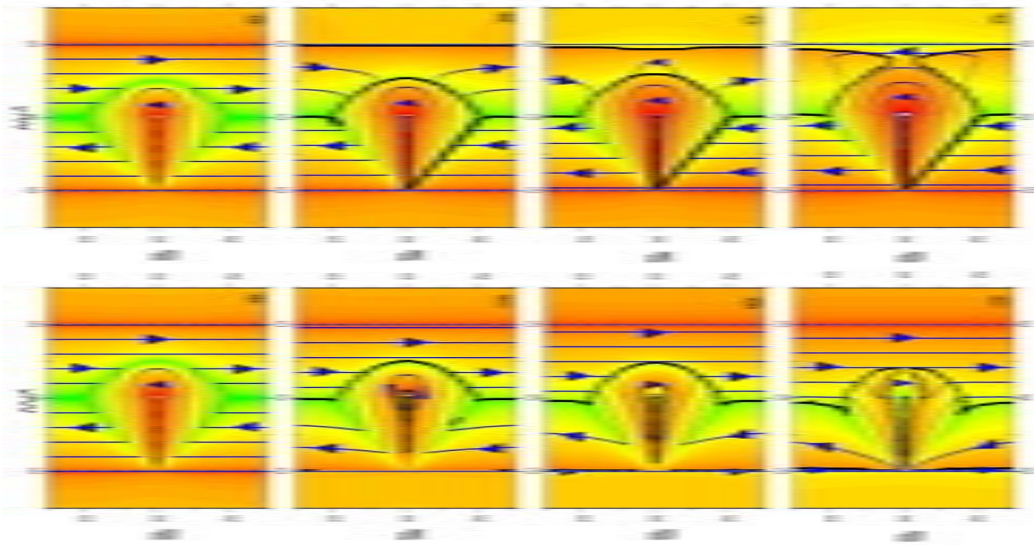
Figure 4.9: Same as in figure 4.1a for the strip with a slit subjected to a large positive perpendicular magnetic field $H_a \to K_c$ to which, after the reach of $H_a$, a transport current of modulus $I_a$ $K_cW$ with increasing values 0 00 0 25 0 375 and up to the saturation one 0 50 (increasing from left to right) is been applied in the negative (top row) or the positive (bottom row) longitudinal directions. Here the out-of-plane magnetic induction ranges from $-2$ 5$\mu_0 K_c$ (blue) through 0 0 (green) and up to $+2$ 5$\mu_0 K_c$ (red).

no change from the application of $I_a$. Actually the critical region in this lower half, delimited by the parabolic $d^+$-line near the slit, will grow towards the upper edge. At the same time a new critical region will penetrate from the top edge. The maximum allowed current $I_{c,s} = K_cW$ 2 is reached when the two flux fronts meet along the slit extension. All along this line currents will then be saturated, but regions with subcritical currents will remain in the other parts of the strip upper half. In particular, far from the slit just $\sim 30\%$ of the upper half width will be filled with critical currents.

On the contrary, if the current is applied in the positive direction, it will distribute itself within the strip lower half. The upper critical region with straight currents will grow towards the lower edge in this case. At the same time critical positive currents will start to penetrate from the bottom edge, including the slit. The saturation is also reached for $I_a = I_{c,s} = K_cW$ 2 when the slit extension becomes fully saturated. In the region at the lower half of the strip and outside this line subcritical currents will be present. The fraction of the lower half width filled with critical currents is also $\sim 30\%$ far from the slit in this case.

### $\pi$ 2-turn

Assume now that we apply the large perpendicular magnetic field to the strip undergoing a $\pi$ 2 radiants turn. The current distribution is the one presented in figure 4.1b. In this case magnetic currents flow in the clockwise direction in the outer half of
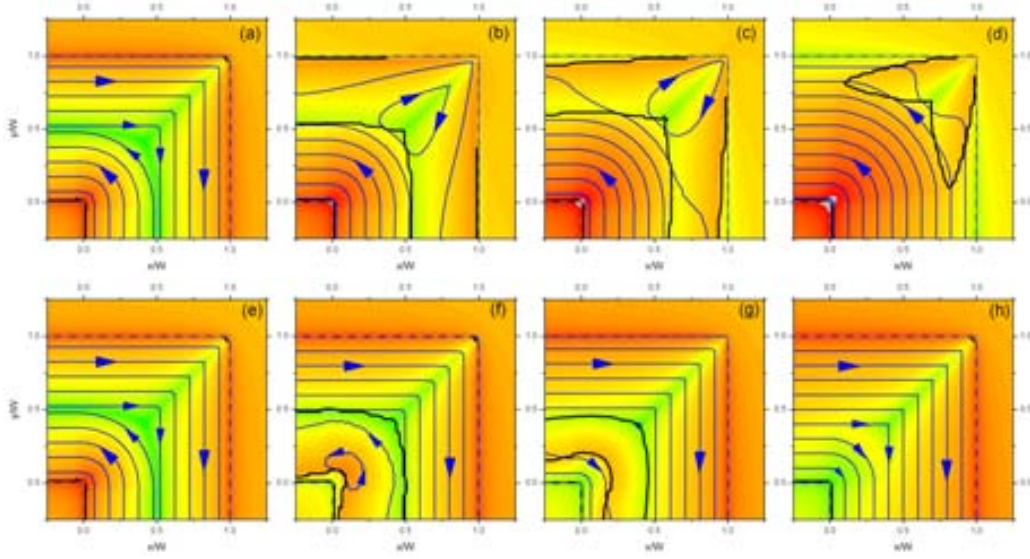
Figure 4.10: Same as in figure 4.9 but for the $\pi/2$ turning strip to which, after the reach of $H_a$, the increasing values of $I_a/K_cW = 0.00$, $0.50$, $0.75$ and the critical one $1.00$ have been fed in the counter-clockwise (upper row) and clockwise (lower row) directions.

the corner (straight currents meeting at a $d^+$-line) and in the counter-clockwise one in the inner half (circular currents near the corner).

The subsequent application of a counter-clockwise current cannot alter the currents in the upper half, where the $d^+$-line is been formed. The applied current will distribute itself throughout the inner half. Actually, the region where these new currents can penetrate defines a strip undergoing a $\pi/2$ turn with the same geometry as the real one but with half its width. Thus, in this half the same final distribution of currents will take place at $I_{c,t} = K_cW$ as for the turning strip under applied current starting from the virgin state (see Sec. 4.1.2). A new critical region with circular currents close to the concave corner will penetrate from the inner edge, including this corner. Meanwhile, the critical regions present along the outer edges will grow towards the inner one but just from the straight segments and not from the $d^+$-line. This line, where currents bend sharply, will never be formed in the lower half.

If the current applied after a large $H_a$ flows in the clockwise direction, the strip half to be filled by these currents is the outer one. Thus, the critical region with circular currents will grow towards the outer edge while a new one will penetrate from the outer straight edges but not from the convex corner. At the end, again, the same as in the case of section 4.1.2 will be observed. However, in this case the circular currents extend up to a distance $d = \frac{3}{4}\sqrt{2}W$ (3/4 of the width of the strip from corner to corner) from the inner concave corner and along its angle bisector. Again the $d^+$-line will never be formed.

### 4.1.5    General behavior under simultaneous applied field and current

In the previous sections we considered different sequences of applied fields and currents to different thin samples initially in the virgin state. These cases included the application of a large perpendicular magnetic field $H_a$ ($H_a \to K_c$) and the subsequent application of a gradually increasing transport current $I_a$ up to the sample critical value, $I_c$. The two possible polarities of applied current were considered. The other cases were those for the same final values of $H_a$ and $I_a$ but $I_a = I_c$ was the first one to be applied, followed by the application of $H_a$ in the two directions perpendicular to the sample. These studies dealt only with two different thin strip geometries. In spite of this, some general rules can be extracted from them regarding the few simple rules behind the penetration of critical currents. These ideas, which apply to any thin strip geometry and sequence of applied field and current, are:

- *New* variations of any external magnitude ($I_a$ or $H_a$) lead to a further penetration of the *old* present critical currents, with $\mathbf{K} = K_c$, where *old* and *new* currents flow in the same direction, and to the penetration of *new* currents from the outer edge where both flow in opposite directions.

- Magnetic currents, induced by a change in $H_a$, penetrate with opposite direction of flow at opposite edges. Differently, transport currents, coming from the applied $I_a$, do so with the same direction at both edges.

- The critical currents at samples with straight edges meeting at sharp corners can be straight, bend sharply (along the $d^+$-lines formed near convex corners) or turn following circular paths (near concave corners), depending on which edge they follow.

- The particular edge that determines the shape of the critical current stream lines is that from where they penetrated the sample.

As a result, by following different sequences of applied fields and currents, one can control which is the edge followed by currents at most of the strip surface.

Of particular interest is the case of a strip undergoing a sharp $\pi$ 2-turn subjected to an applied critical transport current and the subsequent application of a large perpendicular magnetic field $H_a \to K_c$. In this case one can control, by the perpendicular applied field sign, whether a $d^+$-line (currents following the outer edge) or circular currents (following the inner edge) fill the entire sample width at the $I_c$ current.

An important conclusion derived from these rules concerns erasing magnetic history. In strips with non-uniform cross section, it is possible to erase all the information about previous stages by the application of a large magnetic field. This cannot be done if the last magnitude to be varied is the applied current. There, some particular characters will remain at the wider parts telling us something, at least, about the last previous stage.
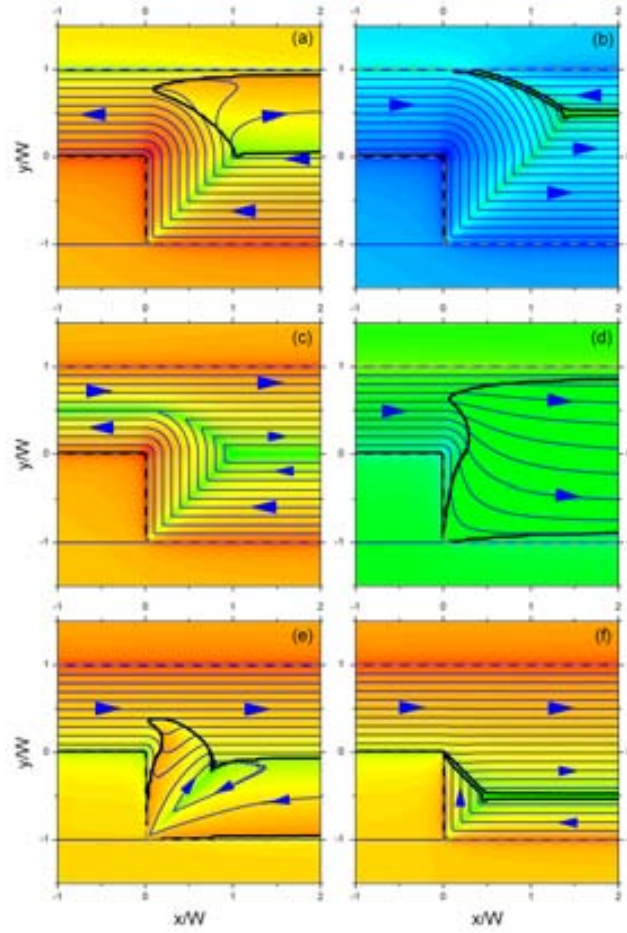
Figure 4.11: Same as in figure 4.1 but for a straight strip of width $W$, sheet current $K_c$ and thus critical current intensity $I_{c,w} = K_c W$ (placed in the $xy$ plane and aligned with the $x$-axis) that widens sharply from its lower edge to reach a new width $2W$. The strip is subjected either to a large (above full saturation) applied positive perpendicular magnetic field (left column) followed by the application of a longitudinal transport current of values $-I_{c,w}$, 0 (magnetic case) and $+I_{c,w}$ (from top to bottom) or to a longitudinal transport current $+I_{c,w}$ followed by a large perpendicular magnetic field of values $-H_a$, 0 (transport case) and $+H_a$ (from top to bottom), with $H_a \to K_c$ (above that of full saturation). Here the out-of-plane magnetic induction ranges from $-2\,5\mu_0 K_c$ (blue) through 0 0 (green) and up to $+2\,5\mu_0 K_c$ (red).

### 4.1.6   Strip with a widening

As mentioned in section 4.1.5 the response to applied fields and currents for any strip geometry can be obtained from the few rules given there. Another example of this of practical interest is that of a strip of width $W$ that, at a given point, widens sharply from one of its edges to achieve a new width $W_w$ (in our case $W_w = 2W$). Interestingly, this geometry presents a very similar behavior to that for the straight strip with a slit, considered above, when $W_w - W = W_s$. The similarities are observed for all the sequences of applied fields and currents considered here and they are specially obvious near the saturation values.

In particular we show the field and current distributions for the full saturation cases for all the sequences considered above, i.e. only magnetic field (Fig. 4.11c), only transport current (Fig. 4.11d), first magnetic field and then transport current (Figs. 4.11a and 4.11e) and, finally, first transport current and then magnetic field (Figs. 4.11b and 4.11f). The last magnitude to be applied is been ramped up to $H_a \rightarrow K_c$ for the magnetic field and up to $I_a = K_c W$ for the transport current.

We can observe how the narrow part is always fully saturated with longitudinal currents of modulus $K_c$ at critical applied current, independently of the followed sequence. However, in the wide half we observe almost identical current distributions as for each of the two halves by each slit side in the strip with a slit.

All of the results presented so far assume a constant critical current density $J_c$. However, they allow us to anticipate some of the effects that the described trends would have on a sample presenting a magnetic-induction-dependent current density $J_c(B)$ (see Sec. 1.3). In this case the critical current of a sample $I_c$ depends on the particular distribution of fields at it. In the particular case of a widened strip as the one studied above we predict an $I_c$ reduction, with respect to that of a strip of uniform width $W$, due to the field enhancement at the sharp concave corner of the widening.

## 4.2   Hysteretic $I_c(H_a)$ in a strip with antidots

In the present section we study the distribution of fields and currents in a thin straight strip of thickness $t$, width $W$ and critical current density $J_c$, with an array of $2 \times 2$ pierced square antidots for different sequences of applied perpendicular magnetic fields and longitudinal transport currents. The antidots side is $a_{hole} = W\,8$ and thus the strip width at narrowest regions, where the holes are present, is $W_{min} = W - 2a_{hole} = 0\,75W$ (see region A in figure 4.12a). In this case the maximum allowed current $I_{c,a}$ for the strip is determined by the width at narrowest segments (see Sec. 4.1.2), so that $I_{c,a} = K_c W_{min} = J_c t W_{min}$. The results we show here were obtained from the numerical procedure described in chapter 2 by considering the sample holes and the different sequences of applied fields and currents as described in sections 2.1.5 and 2.2.4. The used discretization parameters are $\delta_x = W\,80$ and $\Delta g = 10^{-4} K_c W$.

A constant critical current density $J_c$ is assumed. However, the hysteresis in the

distribution of fields for different sequences of applied field $H_a$ and currents, will allow us to anticipate some effects arising from the presence of a magnetic-induction dependence $J_c(B)$. In particular we predict that a hysteresis in the maximum allowed current $I_c(H_a)$ curve will be present in this case. Such hysteresis was already observed in polycristalline samples [145, 146, 147]. Here we demonstrate that this effect can be obtained in uniform strips when the strip width is not constant.

We simulate the two following sequences of applied fields and currents in the strip with antidots. In the first one (1) a perpendicular magnetic field significantly smaller than $K_c$, $H_a < K_c$, is first applied to the sample in the virgin state (see Fig. 4.12a). The increase until $H_a$ is followed by the application of a longitudinal transport current $I_a$ increased up to $0\,7K_cW \sim I_{c,a}$ (see Fig. 4.12b). In the second considered sequence (2) the applied field is first raised up to a large value $H_{a,\mathrm{max}} \sim K_c$, close to the sample full saturation field, and then decreased back to $H_a$ (see Fig. 4.13a). Also in this case the same transport current $I_a = 0\,7K_cW$ is applied after the reach of $H_a$ (see Fig. 4.13b).

When increasing $H_a$ we observe critical currents to penetrate from all of the strip edges. These currents flow in the positive direction at the strip upper half and in the negative direction at its lower half. If the field is farther increased and then reversed back to $H_a$, new currents with opposite direction penetrate from the outer edges (see Sec. 1.3.2).

In sections 4.1.4 and 4.1.5, the effect of applying a transport current to a thin strip already filled with currents was already described. According to these results, applying the positive $I_a$ to the sample of sequence 1 after $H_a$, will lead to the growth of currents flowing in the strip upper half towards its lower one. In this case, the penetrating currents must surround the holes and they do so developing a   -shape next to them when $I_{c,a}$ is reached (see Fig. 4.12b). Differently, in sequence 2 currents flowing in the lower half will be the ones to grow towards the upper half when applying the positive $I_a$. Then, for the latter sequence, at $I_{c,a}$ the current streamlines are   -shaped near the antidots in order to surround them (see Fig. 4.13b).

In the case of constant $J_c$ considered here the maximum allowed current is $I_{c,a}$ for all values of applied field and all sequences of fields and currents, and hence no hysteresis is observed. However, if a $J_c(B)$ were present, the maximum allowed current $I_c(H_a)$ for the sample, would be given by the particular field distribution at regions A (see Fig. 4.12a) when this maximum current was applied. If so, the exact distribution at these regions would be necessary in order to compute the $I_c(H_a)$, but its average across the same regions would give a rough quantity allowing to predict some general trends. We also remark that, although the same sequences were applied, both the distribution of fields and their averages along regions A would be different for the $J_c(B)$ case, from those we show here (but this differences should be small). Thus, by comparing the averaged $B_z$ at the mentioned regions at the end of sequences 1 and 2 (compare Figs. 4.12b and 4.13b), we anticipate that the $I_c(H_a)$ under a $J_c(B)$ dependence would be different for the two sequences, in spite of equal external field $H_a$. The same discussion we make here applies for any $H_a$ within a certain range $0 < H_a < K_c$, if a significantly larger $H_{a,\mathrm{max}} > H_a$ is
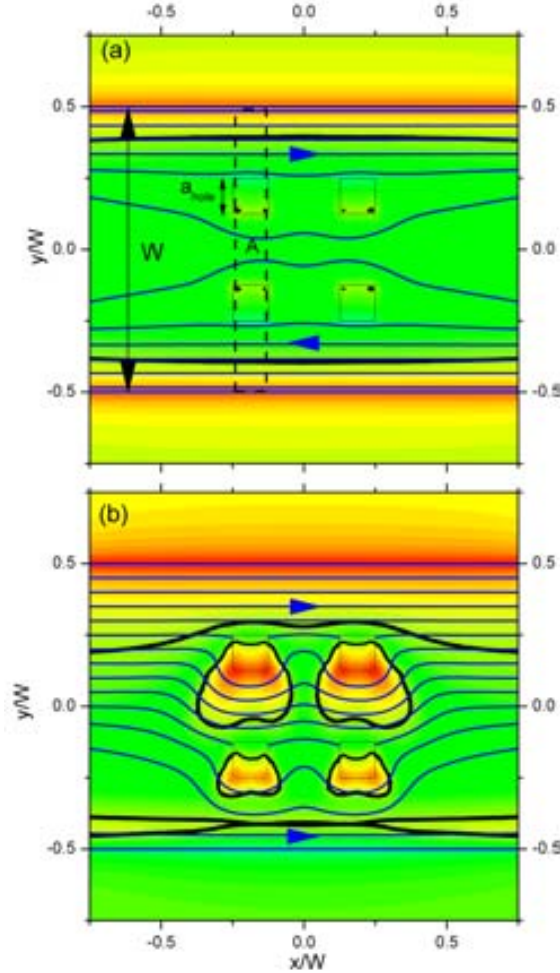
Figure 4.12: Out-of-plane magnetic field $H_z$ (color), and current stream lines (blue lines, arrows indicate direction of current) induced in a thin straight superconducting strip of uniform thickness $t$, width $W$ and constant critical current $J_c$. The strip presents four symmetrical square antidots of side $a_{hole}$. It is subjected to (a) a uniform perpendicular positive magnetic field $H_a = 0\,3K_c$ applied to the zero field cooled (ZFC) sample and, (b) a positive longitudinal transport current $I_a = 0\,7K_cW$, applied after the field $H_a$ is reached (case 1). The critical current intensity value is $I_c = 0\,75K_cW \sim I_a$. $H_z$ ranges from $-K_c$ (blue) through 0 (green) and up to $+K_c$ (red), with the thick black lines separating the regions with $H_z < H_a$ from these with $H_z > H_a$. The region A, framed with black dashed line, is the first one to saturate at $I_c$ together with its symmetric counterpart by the right holes (see text).
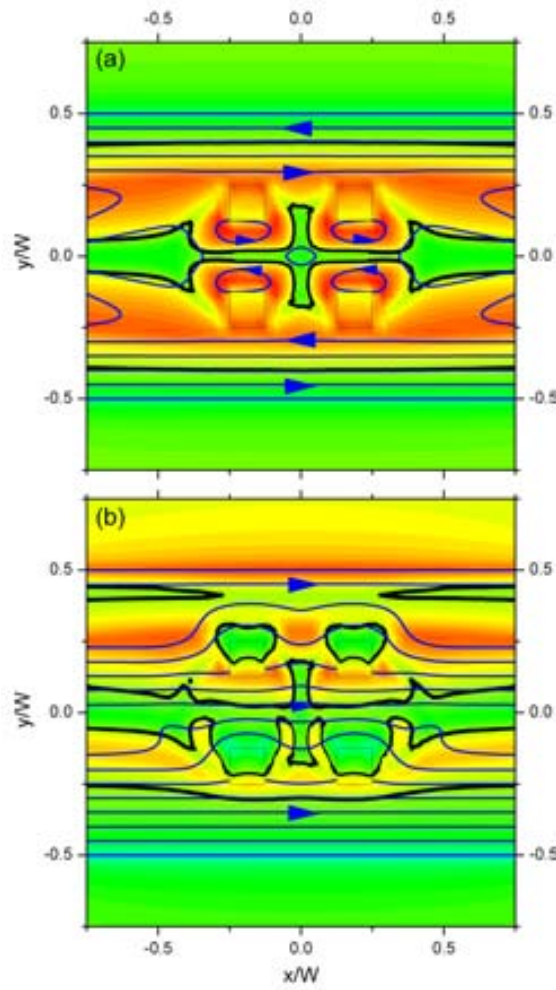
Figure 4.13: Same as in figure 4.12 but when (a) the external field is increased up to a large value, $H_{a,max} = 1\,0K_c$, and then decreased down to $H_a = 0\,3K_c$ and (b) when the longitudinal transport current $I_a = 0\,7K_cW$ is fed into the strip after $H_a$ is reached (case 2).

used, and for arbitrary strip geometry with non-uniform width. Therefore, we predict from these results that a hysteretic behavior in the $I_c(H_a)$ curve will be observed for monocrystalline samples of such geometries under a $J_c(B)$ dependence.

## 4.3   Twin square plates

In this section we recover the study for the twin plates of section 3.3 and extend it for the case of plates in the critical state.

We aim at extending the study by Chen *et al* presented in [77]. There, Chen *et al* proposed an expression for the extraction of $J_c$ in hard superconducting plates from the ac susceptibility curves under alternating magnetic fields. In particular, for the case of thin square plates of side $a$, this parameter was found to be related with the maximum field at peak imaginary susceptibility $H_m(\chi_m)$ and the low-field-limit real susceptibility $\chi_0 = -\chi_{H_m \to 0}$ (see Sec. 1.3.2) according to

$$J_c = \frac{2.43\chi_0}{a} H_m(\chi_m) \tag{4.1}$$

This expression, valid for thin square superconducting plates with no $J_c(B)$ dependence, was obtained from the scaling of the magnetization curves for thin disks with the same properties[77, 90, 148] discussed in section 1.3.2. The validity of this expression and the more general one for rectangular plates was already checked from numerical calculations for samples of these geometries. However, it was not studied which would be the effect of adding a second plate, and whether it would be equally valid or would require some modification to account for the new effects arising from their interaction.

Here we analyze how is the relation 4.1 affected by the presence of the second plate. In these studies the same two identical plates described in section 3.3 are subjected to a perpendicular magnetic field $H_a \to H_{c1}$. Under these circumstances identical current and field distributions are induced in both. To simulate them we extend the same method to account for a finite constant $J_c$ as described in section 2.1.5, from which the $g(\mathbf{r})$ distribution within the plates is obtained. In this case the currents come either from surface Meissner currents or from curved or flat vortices depending on the ratio of London penetration depth $\lambda$ to plate thickness $t$, $\lambda \ll t$ (see Sec. 1.3.2), but the behavior described below for the thickness-averaged current $\mathbf{K}$ is independent on this ratio. The results from these calculations are compared with experimental results.

We carried out the calculations for the pair of plates divided in $N \times N = 100 \times 100$ square identical cells each and separated by different $d/a = 0.0, 0.05, 0.1, 0.15, 0.2$ and $\infty$ (the last corresponding to one isolated plate). The samples were assumed to be zero-field cooled and hence to have no trapped flux nor currents at $H_a = 0$. The applied field was increased from $H_a = 0$ to $H_a > K_c \equiv J_c t$ and a $\Delta g = 5 \cdot 10^{-5} \ K_c a$ was used.

In particular, we show and discuss the effects of the second plate and of varying their relative distance on the distribution of fields and currents. Also studied are the overall magnetization of the set and its ac susceptibilities at fundamental frequency, the latter
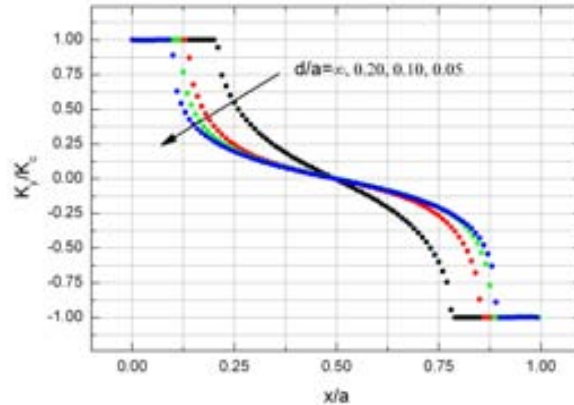
Figure 4.14: Normalized sheet-current component $K_y$ $K_c$, with $K_c = J_c t$, as a function of position $x$ $a$ along the central $y = 0$ line ($K_x = 0$) of the two square identical thin parallel plates of critical current $J_c$, side $a$ and thickness $t \propto a$. The plates are placed perpendicular to the $z$ axis with corners at the same ($x$ $y$) coordinates ($\pm a$ 2 $\pm a$ 2), separated by different distances $d$ $a =$     0 2 0 1 and 0 05 along $z$ (decreasing in the arrow direction) and subjected to an external perpendicular uniform field of modulus $H_a = 0\,5K_c$. The field is applied after zero-field cooling and induces the currents identically in the two plates.

compared with experimental results. Finally the validity of equation 4.1 for this system is analyzed.

### 4.3.1   Evolution of magnetic currents

When a perpendicular field $H_a \to H_{c1}$ is applied to the thin square plate critical and Meissner currents penetrate the sample. In particular, depending on the ration $\lambda$ $t$ The sheet current $\mathbf{K}(\mathbf{r})$ (see Sec. 2.1.2) is calculated with the aid of equation 2.2 from the sheet function $g(\mathbf{r})$ profiles. We plot in figure 4.14 the calculated currents, identical for the two plates, along the perpendicular bisector of two of its sides ($y = 0$), for different $d$ $a$ and an $H_a = 0\,5K_c$ of significant penetration.

The behavior of these currents for the particular case of one single plate (equivalent to that with $d$ $a \to 1$) is described in section 1.3.2. The sharp $\pi$ 2 radiants convex corners present in a thin square plate lead to the already known cushion-like shaped subcritical region when a uniform perpendicular magnetic field is applied (see Fig. 1.4a). This shape does not vary significantly when the second plate is placed on top of the first one (not shown). However, we can see in figure 4.14 how the depth of penetration of this region for a given $H_a$, is shorter for smaller $d$ between the plates. We only plot the currents for $H_a = 0\,5K_c$ because, although delayed, the penetration in increasing field for the different $d$ $a$ is analogous to that for one plate. This slower penetration of the saturated region is due to the partial shielding of the external field each plate makes on the other one. Therefore, the effective external magnetic field each plate must shield for

a given applied one, will be lower for smaller distance $d$.

The full saturation of currents in thin plates takes place at infinite $H_a$ (see Sec. 1.3.2). This is solved by introducing a cutoff distance of the largest among $t$, $\lambda$ and $\Lambda$ on the size of the inner flux-free core. When the profiles are solved numerically, the resolution is limited to the size of the grid unit cell, $\delta_x$. In that case the cutoff distance will be on the order of $\delta_x$ if $t$, $\lambda$ and $\Lambda$ are all shorter than it. When this full saturation is reached, it follows from the Bean model assumptions that the profiles must depend just on the sample geometry and not on the presence of a second one. At that point currents follow straight paths parallel to the closest edge and bend sharply along the square diagonals forming the so called $d^+$-lines [12].

### 4.3.2  Magnetization of the twin films

From the sheet current flowing within the plate, the perpendicular magnetization, $M_z$, can be calculated from equation 2.19. We plot in figure 4.15 the calculated $M_z$ as a function of applied field $H_a$ for $H_a$ $K_c$ from 0 0 to 3 0, where it was found to be saturated. We observe that in the low-field limit $M_z(H_a)$ is negative and decreases linearly with a slope $-\chi_0$, corresponding to the constant slope in the Meissner state (see Sec. 1.3.2).

The presence of the second plate does not modify this linearity, observed at low fields, for any separating distance $d$ $a$ between the two of them. However, we already observed in section 3.3 how this initial slope absolute value, monotonically decreases with decreasing $d$ from that of one single plate ($\chi_0 = 0$ $4547$ $a$ $t$) at $d \to a$ to one half of that value ($\chi_0 = 0$ $2274$ $a$ $t$) for $d = 0$. The simulation of very small $d$ $a$ would require long computing times since $d$ $a < 1$ $N$ is needed. In spite of this, the whole curve for $d = 0$ can be obtained from scaling that of one isolated plate.

In the opposite limit, when $H_a$ is very large, the negative magnetization of each plate approaches the saturation value $M_s = J_c a$ $6$, independent on the number of plates and $d$. Although thin samples never get fully saturated, a field of significant penetration is defined as $H_s \equiv M_s$ $\chi_0$.

For intermediate values of $H_a \approx H_s$ the magnetization slope absolute value monotonically decreases from the low-field limit ($\chi_0$) to zero when it reaches $M_s$ at some $H_a > H_s$. From the decrease of $\chi_0$ with decreasing $d$ $a$ a shift to larger $H_a$ of the saturation reach follows, as shown by the increase of $H_s$.

From the universality of the magnetization curve, $M_z(H_a$ $H_s)$ $M_s$, for thin samples, Gilchrist proposed a scaling law to obtain such curves for arbitrary geometry from that of a thin disk (see Sec. 1.3.2). The parameters used for the scaling are $\chi_0$ and $M_s$. We show in figure 4.15 with dashed lines the curves obtained following this approach. The maximum difference observed between the scaled and the calculated curves for $d$ $a =$ is actually found to be roughly 0 3%. However, as $d$ $a$ is made smaller, we observe this difference to increase monotonically and the scaling does not offer a good approximation anymore. For $d$ $a = 0$ the agreement between the two curves is again very good, which
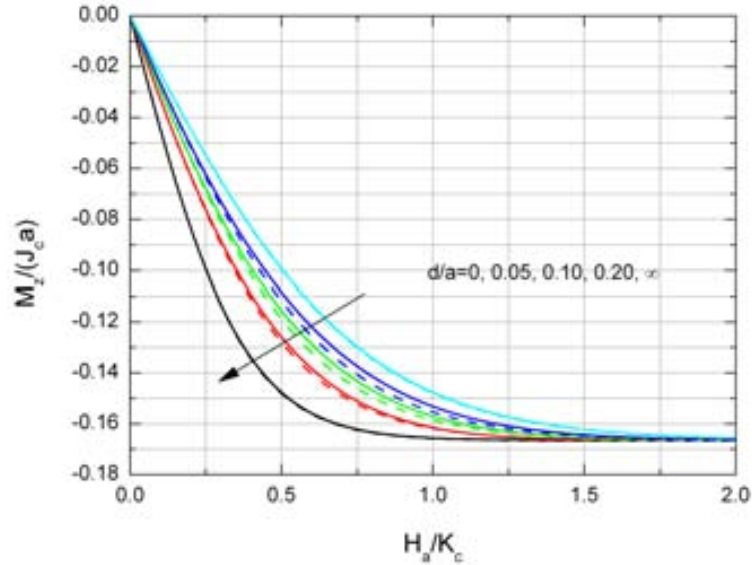
Figure 4.15: Calculated (solid lines) normalized out-of-plane magnetization $M_z$ $J_ca$, as a function of the uniform perpendicular applied magnetic field $H_a$ $J_ct$, induced in the same plates, of critical current $J_c$, side $a$, and thickness $t \propto a$, of figure 4.14. The different curves correspond to different separation distances between the plates, $d$ $a = 0$ $0$ $05$ $0$ $1$ $0$ $2$ and     (increasing in the arrow direction). In dashed lines we plot the same quantity but in this case obtained from scaling the magnetization of a thin disk [148] by using the corresponding $\chi_0$ calculated for each $d$ $a$ (shown in Fig. 3.14) and the saturation magnetization for square plates $M_s = -J_ca$ $6$ (see text).

is not surprising since $M_z$ is calculated from that for $d$ $a =$   .

One could expect this difference in the behavior to appear at short $d$ $a$ since the scaling was proven to work for different sample shapes but always assumed a uniform magnetic field was applied. However, the case of two or more samples close to each other is equivalent to the application of a nonuniform magnetic field. Moreover, since we cannot simulate the plates in the short $d$ $a > 0$ range, we cannot conclude whether the discrepancy should decay when decreasing $d$ $a$ from some short distance or suddenly drop at $d$ $a = 0$.

In fact, Mawatari [65] already showed how an infinite stack of parallel strips periodically arranged along its perpendicular direction presented an $M_{ini,z}(H_a)$ very different to that of one strip. In that case only in the limit of very large ratio of strips distance to width, $d$ $W \to 1$, the $\tanh(x)$ dependence of the single strip was recovered.

### 4.3.3   AC external susceptibilities

In the present section we study the theoretical susceptibilities, computed from the magnetization, and the experimental ones, measured from the pairs of YBCO plates described in section 3.3.2. Here we only study the external ac susceptibility at fundamental frequency (see Sec. 1.3.2).

**Calculation results**

Since the Bean model with constant $J_c(B)$ is assumed, we use the expressions 2.21 and 2.23 to calculate $\chi'$ and $\chi''$, respectively, from the initial magnetization curve. We show in figure 4.16 the real and imaginary susceptibilities, $\chi' \equiv \chi'_1$ and $\chi'' \equiv \chi''_1$, for the two thin plates computed from these equations. The susceptibilities are studied as a function of $H_m$ for different plates separation $d/a$. Actually, the response of samples simulated in the Bean critical-state model does not depend on the particular profile of $H_a(t)$, nor on its frequency, because it neglects all the dynamic effects like the flux flow and the flux creep.

The well known general trends for $-\chi'$ and $\chi''$ in the different limits are observed for all plotted distances $d/a$ (see Sec. 1.3.2).

When the two plates are approached, the initial $-\chi' = \chi_0$ decreases with decreasing $d/a$. As a result of this, $H_s$ increases when $d/a$ is made smaller and both the decay of $-\chi'$ and the peak of $\chi''$ are shifted to larger $H_m$. A useful interpretation of $\chi''(H_m)$ shows it is proportional to the ratio between the area inside the magnetization loop for $H_m$ and the circle of radius $H_m$ [61]. Therefore, since the decrease in $\chi_0$ also makes smaller the magnetization loop area, this allows to understand why decreasing $d$ will also reduce the maximum $\chi''$, $\chi_m$.

In particular, as is well known, the decays of $-\chi'$ and $\chi''$ in the high-field limit as $H_m^{-3/2}$ and $H_m^{-1}$, respectively, correspond to a constant $M_z$ in increasing $H_a$. This is a general behavior characteristic of the Bean model with constant $J_c$ and independent of sample geometry and applied field profile (see Sec. 1.3.2). Therefore, this behavior is observed for all the present cases, as can be seen from figure (4.16b).

In the low-field limit, it was shown how $\chi''$ grows linearly with $H_m$ in longitudinal geometry while it does as $H_m^2$ in transverse one, being independent on the particular shape of the sample cross section in both cases [58, 57, 61, 92]. The possibility to obtain the magnetization curve of a single thin square plate by scaling that of a thin disk also allows for the obtaining of its suceptibility in the same way. Therefore, since for $d/a = \infty$ and $d/a = 0$ the behavior is equivalent to that of one plate, in these cases one would also expect $\chi'' \propto H_m^2$ in the low-field limit. This is actually what we observe in figure 4.16b.

For $H_m$ lower than $0.2 J_c t$ significant numerical error arises from the use of the discretized expression in equation 2.23 to calculate $\chi''$ and from the little accuracy in the calculated $M_z(H_a)$ in this range. However, we can still see from figure 4.16 how $\chi''$ approaches the $\propto H_m^2$ curve for decreasing $H_m$ for all different distances $d/a$.
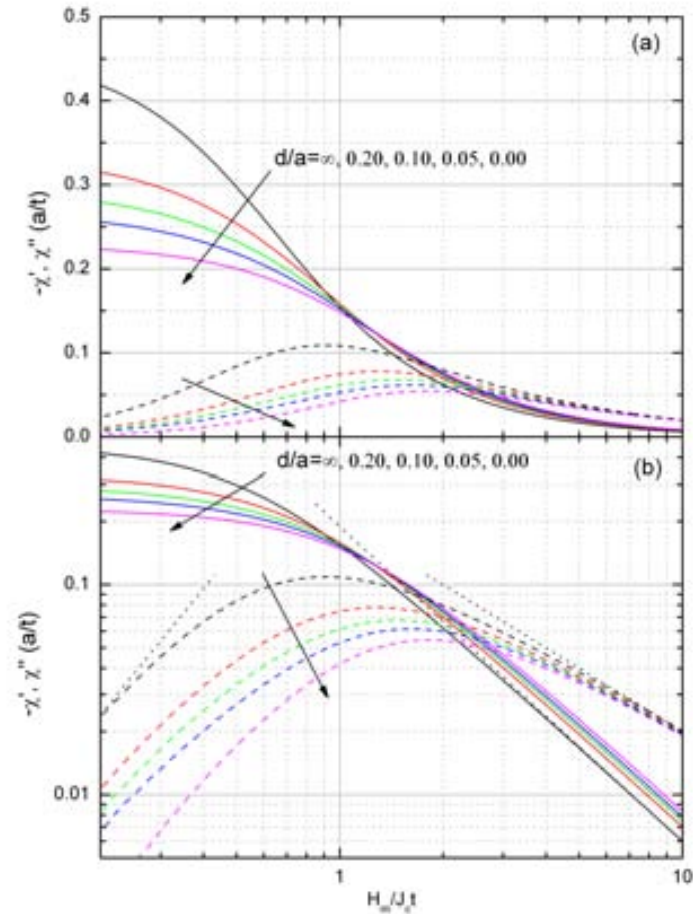
Figure 4.16: Calculated real and imaginary external susceptibilities, $-\chi'$ (solid lines) and $\chi''$ (dashed lines), of the two plates, of critical current $J_c$, side $a$ and thickness $t \propto a$, of figure 4.14 and separated by different distances $d/a = \infty$, 0 2 0 1 0 05 and 0 (decreasing in the arrow direction). Figures (a) and (b) show in log-linear and log-log scales, respectively, the susceptibilities normalized to $a/t$, as a function of the maximum of the alternating applied magnetic field, $H_m$, normalized to $J_c t$. Dotted lines in (b) show the predicted behaviors in the corresponding limits (see text).
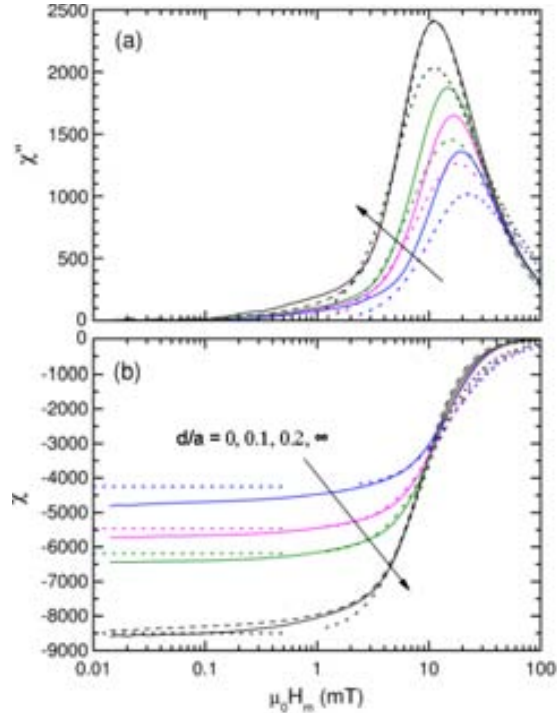
Figure 4.17: Same calculated curves as in figure 4.16 (dotted lines) altogether with the measured curves (solid lines) for the real samples A and B (see Sec. 3.3.2) of side $a = 5$ mm and thickness $t = 0.25$ $\mu$m for different separation distances $d/a = 0, 0.1, 0.2$ and $\infty$ (increasing in the arrow direction). The susceptibilities are plotted as a function of the maximum in the uniform alternating induction, $B_m = \mu_0 H_m$ (in mT), applied perpendicular to the plates. Due to the large numerical error in the calculated curves for $B_m < 1$ mT, in this range we plot $\chi' = -\chi_0 = $ constant, its low-field limit value. Solid and dashed black lines correspond to individual samples A and B, respectively, and would equal the $\chi$ of two identical plates at long distance ($d/a = \infty$). The calculated curves are scaled by a factor 0.935 to fit the experimental $\chi_0$ (see text).

**Results from measurements**

Measurements of ac susceptibilities were carried out in three pairs of thin square superconducting samples of YBCO. The samples are described in section 3.3.2 and were measured with a home-made high-field ac susceptometer, up to large applied fields $H_m$, in a 77 K atmosphere. The average results for the individual A and B, from the first pair, are regarded as the results for two plates separated by a distance $d/a \to \infty$. In figure 4.17, these results and the ones for the two plates with $d/a = 0, 0.1$ and $0.2$, are compared with the numerical results in figure 4.16. These samples were chosen because they were observed to present very similar $\chi''_m$ and $H_m(\chi''_m)$, as can be seen from figure 4.18.

The results from measurements for the case of one single plate (or $d/a = \infty$) are also
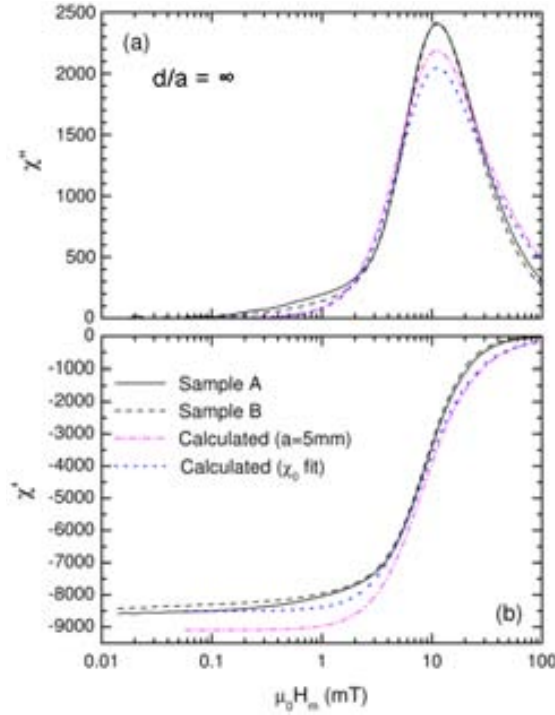
Figure 4.18: The measured $\chi''$ (a) and $\chi'$ (b) in individual samples A and B (corresponding to identical plates at $d/a = \infty$), arranged as in figure 4.14, as a function of $\mu_0 H_m$ (in mT). Also plot are the curves analytically calculated from scaling these of a thin disk using equations (17) and (18) in [148] (dashed-dotted lines), and the same calculated curves scaled by a factor of 0.935 (dotted lines) as indicated in the text.

compared with the analytical results obtained from the scaled magnetization of a thin disk (see Fig. 4.18). In this case the theoretical curve is calculated with the values $a = 5$ mm and $t = 0.25$ $\mu$m, but the theoretical $\chi_0 = 9094$ obtained by doing so is larger than the measured averaged $\chi_0 = 8500$. A side of $a = 4.888$mm fits better the experimental $\chi_0$ by reducing the calculated value (due to $\chi_0 = 0.4547\, a/t$) and increasing the measured one (due to sample volume $\propto a^2$) to a common value of about 8890. This effect could be due to the presence of a narrow region of normal material of width $\delta_n \approx 0.056$ mm, as is suggested by the observation by visual inspection of some normal regions near the corners of the samples. Moreover, this is the reason for patterning new samples of sides $a = 4$ mm from the former ones with $a = 5$ mm as mentioned in section 3.3.

Therefore, the calculated curve is multiplied by a factor 0.935 in order to fit the experimental value $\chi_0 = 8500$, as shown by the dotted lines. If this is done, we observe the following. On the one hand, the calculated $-\chi'$ is observed to be systematically lower than the measured one within the whole $H_m$ range and, on the other hand, the calculated $\chi''$ is lower than the experimental one near the peak and larger at higher $H_m$.

In figure 4.17 the calculated curves for all different values of $d/a$ are multiplied by
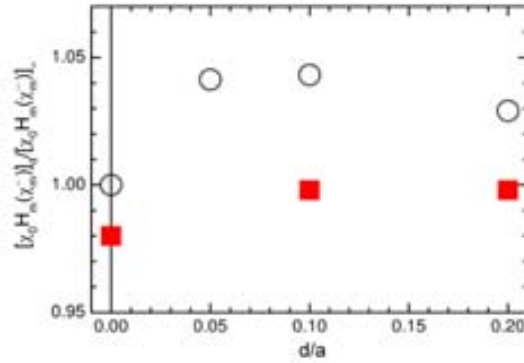
Figure 4.19: Numerical (open circles) and experimental (full squares) $\chi_0 H_m(\chi_m)$ as a function of plates distance $d/a$, where $\chi_0 = -\chi'(H_m \to 0)$ is the low-field limit real susceptibility and $H_m(\chi_m'')$ is the maximum alternating field at maximum imaginary susceptibility. Both numerical and experimental results are normalized to $[\chi_0 H_m(\chi_m'')]_{d/a=\infty}$, the calculated value for very distant plates. The measurements were performed on samples A and B.

the same factor $0.935$. After multiplying by this factor, the same discrepancies between measured and calculated $\chi'$ and $\chi''$ are observed for finite $d/a$. One possible cause is the presence of a $J_c(B)$ dependence [92] or creep of magnetic flux [85, 149] in the real samples, which are both neglected in the model assumed (Bean model) for the calculations. However, a pronounced field dependence of critical current $J_c(B)$ would give a decay of $\chi''$ in the high-field limit much faster than the observed one $(\chi'' \sim H_m^{-1})$ in the experimental results.

We can also observe the experimental $\chi_0$ to be larger than the calculated one for all finite values of $d/a$ and the experimental $H_m(\chi_m'')$ to be lower than the theoretical one. Therefore we wonder whether this systematic experimental over-large $\chi_0$ and over-low $H_m(\chi_m'')$ could still lead to the fulfillment of equation 4.1 or not.

In particular we show in figure 4.19 the quantity $[\chi_0 H_m(\chi_m'')]_d$ normalized to that of one single plate (or $d/a = \infty$). Although we cannot conclude which is the reason for the deviation of up to $\approx 4\%$ of the calculated values from these of equation 4.1, we can still observe this quantity to be almost independent on the number and separation distance of plates both for the measured and calculated results.

In spite of the observed discrepancies, from the insensitivity to the variation of $d/a$ of $[\chi_0 H_m(\chi_m'')]$ it still may be concluded that equation 4.1 may be used for the $J_c$ determination of twin films. The validity of this equation to the twin film case is logical, since $\chi_0 H_m(\chi_m'')$ should be at least roughly proportional to the saturation magnetization $M_s$, which is a function of film shape and $J_c$ but not film number [148].

CHAPTER **5**

## Conclusions

We have theoretically studied the response of type-II superconductors to applied magnetic fields and more specially to applied transport currents. Throughout the work we consider thin and planar plates or strips of different shapes. The used approaches are the London and the critical-state models, very useful for describing the behavior of superconductors in spite of their limiting intrinsic assumptions. These two models apply in very different regimes. Thus, we have divided our work in two main parts. The first one deals with the Meissner state within the London theory. In the second part we study the behavior in the critical state.

All of these results are obtained based on the Magnetic Energy Minimization (MEM) model. This model, already used previously for other geometries, has been adapted for the thin planar geometry. It has been extended to account for holes or antidots within the superconducting samples and specially to that of an applied transport current besides to the external magnetic field. Both extensions are applied successfully to the two considered states. Moreover, in the case of samples simulated within the London model many different conditions on the trapped fluxoids at present holes can also be studied. The model is able to reproduce any desired sequence of applied fields and currents. This is specially important when the hysteretic behavior characteristic of the critical state takes place.

In the first part we have extended previous studies on different thin strip geometries by describing the behavior of transport currents for a more general case. We have dealt with sharp corners, present in many applications, within samples of arbitrary two-dimensional screening length $\Lambda$. These studies are also applied to acquire a better knowledge and control for the conditions of vortex nucleation. We remark the observed enhancement of the current crowding effect, according to which transport current accumulates near corners, when the ratio of $\Lambda$ to strip width $W$ is decreased. Previous

works only dealt with the case $\Lambda \ll W$. The distance from the corners up to which their effects on the flowing currents can be observed has also been studied. This has been done for both the applied field and current cases and for different values of $\Lambda/W$ within the whole range $\Lambda/W \in (0 \infty)$.

We also include some more detailed studies on the Meissner currents near the sharp $\pi/2$ radiants turn of a thin strip of width $W$ undergoing such a turn at some point along its length. There the combination of an applied magnetic field and a longitudinal transport current has been considered. In this case, for a particular relative sign between the applied field and current, currents induced by each of these magnitudes partially compensate at a given edge. By choosing properly their intensity, a state with zero local current at a particular edge spot can be achieved. We study the conditions for which this happens at the inner concave corner of the strip and at the strip straight edges far from the turn. We observe how, for a fixed value of the applied field, when $\Lambda$ is smaller this condition is reached at the corner for much larger applied current. However, the opposite happens for large $\Lambda$, and this condition is met for larger applied current at the far straight edges. The crossover takes place at $\Lambda \approx 0.3W$.

Another interesting topic of research that appeared recently is that of metamaterials. There the design of the material on a small, often microscopic, scale, leads to an effective response on a larger scale interesting for many applications. We make an accurate and systematic study of the effective behavior of two parallel and non-coplanar identical square plates, as a function of their separating distance. We analyze the particular dependence between the susceptibility and the plates separating distance, proving how by changing this distance the effective susceptibility of the system as a whole can be tuned. A comparison with experimental results is also included. This study wishes to contribute on the achievement of desired magnetic susceptibilities for the design of metamaterials.

In the second part of the thesis, the superconductor is assumed to be in the critical state. First we make a systematic study of the magnetic and transport currents for some strip geometries of practical interest. These include sharp turns, slits and widenings. Previous to the present work, systematic studies in the transport regime only existed for geometries involving one or several straight strips of uniform width. We have shown how transport currents are also rounded near sharp turns at the inner edges, just like in the magnetic field case. However, the maximum allowed value for the applied transport current is reached when the strip becomes fully saturated at the narrowest strip segments. At this point some subcritical regions are observed to remain at wider segments. These results allow us to make some predictions on the impossibility of the formation of the known as $d^+$-lines, where critical currents must bend sharply, when just a transport current is applied to the sample. These predictions apply to any thin strip geometry.

We next studied the consecutive application of transport currents and magnetic fields. In general, the distribution of currents under different sequences of these applied magnitudes has been observed to follow few simple rules. In the critical state, changing the applied external magnitude (magnetic field or transport current) that is being varied,

or its sign of variation, induces the deeper penetration of present currents at some regions and the penetration of new ones from the outer edges at some others. The former behavior is observed where currents induced by the new variation have the same sign as the already present ones. The new penetration of currents from an outer edge takes place where these new currents flow in the opposite direction than the old ones. The direction of flow of currents is determined by the magnitude to be varied. In particular, the variation of the magnetic field induces currents flowing in opposite directions at opposite edges of the sample and the variation of an applied transport current leads to the penetration of currents flowing in the same direction at both edges. We also remark that the shape of the streamlines of critical currents, those with maximum allowed modulus, is determined by the sample edge where they started. These shapes include straight lines (near straight edges), sharp bends (at convex corners, where the edges form an angle lower than $\pi$) and circular arcs (at concave corners, where the edges form an angle larger than $\pi$). We remark the possibility, derived from these trends, to control which is the edge followed by currents at most of the strip surface by means of the sequence of applied fields and currents.

Another prediction from our results is the appearance of hysteresis in the critical current intensity, $I_c(H_a)$, in strips subjected to an external applied field, $H_a$. In this case the strip is regarded to be homogeneous but could be of any geometry whose width is not uniform along length. In particular we considered the case of a straight strip pierced with some square antidots. If experimentally demonstrated this would appear as a new source for hysteresis in the critical current of thin superconducting strips.

Finally, we briefly reviewed a formerly derived procedure for the determination of the critical-current density, from magnetic measurements, of single superconducting plates of different geometries. After doing so we have extended the same procedure to the case of two parallel and non-coplanar plates, studying it for a system consisting of two square identical plates.

The MEM model we present here appears as one of the very few recently developed ones allowing for the inclusion of a transport current for arbitrary thin superconducting planar shapes. Apart from systematic studies of the phenomena involved in these systems, this extension also allows for the simulation of particular geometries of practical interest. Of significant importance is also the possibility to account for the effects from present holes under different conditions of trapped fluxoids. Examples of such studies are the possibility to seek for the optimum tuning of the position and behavior of single vortices in bulk-pinning-free samples. The same can be done to control the magnetic field distribution in the sample surroundings. It could also help to predict with more accuracy on the desired or undesired distribution of critical currents under strong bulk pinning, and the effects deriving from their generated magnetic fields.

One of the possible extensions to the model, is the consideration of an induction-dependent critical-current density $J_c(B)$. This would allow for the reproducibility of other phenomena present in hard superconductors.

About one century after its first discovery, superconductivity is still surprising us

with new and better understood phenomena. Its use and presence in so many hot topics of research in different fields, makes superconductivity itself a very productive field from the point of view of the generation of new knowledge. We hope the discoveries and studies we present here, and future ones derived from them, to be useful for the design of devices with a better performance. Some of the devices where the studied effects may play an important role range from waveguides, used for the implementation of quantum gates and for particle accelerators, to single photon detectors or transition edge sensors, used for cosmological observations, or to cold-atom traps, with applications on the fields of quantum computing and simulation. Moreover, some of these phenomena can be also useful for the coated conductors used for power applications such as cables, fault-current limiters, motors and energy storage systems like SMES or flywheels. Thus, the studies made here may contribute on the better understanding of our world from a fundamental point of view as well as for the development of a more sustainable and environmentally respectful future society.

## Analytical expressions for the integrated $E_{int}$ kernel for twin films

In this appendix we give the analytic expressions for the kernel of the terms of the minimization functional term $E_{int}$, integrated over the surfaces of the different pairs of cells in the discretized twin films (see Sec. 2.2.5).

The kernel we need to integrate is that from the Biot-Savart law although here we have to perform a double surface integral in order to compute the internal energy terms. These integrated expressions were already given in [137] for the case of a single plate. Here we extend the above mentioned expressions for the case when the surface integral is performed over two cells belonging to different twin plates at different height.

In particular, we seek for the expressions for the double surface integral of the kernel in the $E_{int}$ terms from equation 2.33 performed over the cells $c$ and $c$ of the plates $k$ and $k$ , repsectively, for $c$ $c$ [1 $N \times M$]. For $k = k$ and after taking the limits for the resulting expressions, those given in [137] are recovered. Here we assume the $k$-th plate to be placed at $z_k$ along the perpendicular, vertical, direction. We always divide the samples into uniform grids of $N \times M$ rectangular cells of sides $\delta_x$ and $\delta_y$ along the in-plane $x$ and $y$ directions, respectively. In this case, these expressions are given by:

$$
\begin{aligned}
N_{kk',cc'} &= \frac{1}{4\pi} \int_{S_{k,c}} \int_{S_{k',c'}} \frac{\mathrm{d}S \mathrm{d}S}{\sqrt{(x - x\,)^2 + (y - y\,)^2 + (z_k - z_{k'})^2}} \\
&= \frac{1}{4\pi} T(x\ x\ \ y\ y\,) \, {}^{(x_k+\delta_x, x_{k'}+\delta_x, y_k+\delta_y, y_{k'}+\delta_y)}_{(x_k, x_{k'}, y_k, y_{k'})}
\end{aligned}
\tag{A.1}
$$

where the primitive function

$$T(x\ x\ \ y\ y\ ) = \frac{1}{6}\Big[(y - y\ )^2 \sqrt{(x - x\ )^2 + (y - y\ )^2 + (z - z\ )^2}$$

$$-(x - x\ )(y - y\ )(z - z\ )\arctan\left(\frac{(x - x\ )(y - y\ )}{(z - z\ )\sqrt{(x - x\ )^2 + (y - y\ )^2 + (z - z\ )^2}}\right)$$

$$-\frac{1}{2}(x - x\ )((y - y\ )^2 + (z - z\ )^2)\ln\left((x - x\ ) + \sqrt{(x - x\ )^2 + (y - y\ )^2 + (z - z\ )^2}\right)$$

$$-\frac{1}{2}((x - x\ )^2 - (z - z\ )^2)(y - y\ )\ln\left((y - y\ ) + \sqrt{(x - x\ )^2 + (y - y\ )^2 + (z - z\ )^2}\right)\Big] \quad \text{(A.2)}$$

Here the $k$-th cell of each plate is chosen to be placed at $x\ \ (x_k\ x_k + \delta_x)$ and $y\ (y_k\ y_k + \delta_y)$.

# Bibliography

[1] H. Kamerlingh Onnes. The superconductivity of mercury. *Comm. Phys. Lab. Univ. Leiden*, 122, 124, 1911.

[2] JK Hulm and BT Matthias. High-field, high-current superconductors. *Science*, 208(4446):881 887, 1980.

[3] J George Bednorz and K Alex Muller. Possible high-Tc superconductivity in the Ba-La-Cu-O system. *Zeitschrift für Physik B Condensed Matter*, 64(2):189 193, 1986.

[4] MK Wu, JR Ashburn, CJ Torng, Ph H Hor, RL Meng, Lo Gao, Z J Huang, YQ Wang, and CW Chu. Superconductivity at 93 K in a new mixed-phase Y-Ba-Cu-O compound system at ambient pressure. *Physical Review Letters*, 58(9):908 910, 1987.

[5] SR Foltyn, L Civale, JL MacManus-Driscoll, QX Jia, B Maiorov, H Wang, and M Maley. Materials science challenges for high-temperature superconducting wire. *Nature materials*, 6(9):631 642, 2007.

[6] Walther Meissner and Robert Ochsenfeld. Ein neuer effekt bei eintritt der supraleitfahigkeit. *Naturwissenschaften*, 21(44):787 788, 1933.

[7] F London and H London. The Electromagnetic Equations of the Supraconductor. *Proceedings of the Royal Society of London Series A-Mathematical and Physical Sciences*, 149:71 88, 1935.

[8] WA Little and RD Parks. Observation of quantum periodicity in the transition temperature of a superconducting cylinder. *Physical Review Letters*, 9(1):9 12, 1962.

[9] John Bardeen, Leon N Cooper, and John Robert Schrieffer. Theory of superconductivity. *Physical Review*, 108(5):1175, 1957.

[10] A. A. Abrikosov. On the magnetic properties of superconductors of the second group. *Soviet Physics JETP-USSR*, 5:1174 1183, 1957.

[11] V. L. Ginzburg and L. D. Landau. To the theory of superconductivity. *Zhurnal Eksperimentalnoi i Teoreticheskoi Fiziki*, 20:1064 1082, 1950.

[12] A.M. Campbell and J.E. Evetts. Flux vortices and transport currents in type II superconductors. *Advances in Physics*, 21(90):199 428, mar 1972.

[13] G Blatter, MV Feigel Man, VB Geshkenbein, AI Larkin, and V M˗ Vinokur. Vortices in high-temperature superconductors. *Reviews of Modern Physics*, 66(4):1125, 1994.

[14] TTM Palstra, B Batlogg, LF Schneemeyer, and JV Waszczak. Thermally activated dissipation in $Bi_{2.2}Sr_2Ca_{0.8}Cu_2O_{8+\delta}$. *Physical review letters*, 61(14):1662 1665, 1988.

[15] P. Ao and D.J. Thouless. Tunneling of a quantized vortex: Roles of pinning and dissipation. *Physical Review Letters*, 72(1):132 135, 1994.

[16] A Hoekstra, JC Martinez, and R Griessen. Vortex tunneling in thin films of $YBa_2Cu_3O_{7-\delta}$ and $YBa_2Cu_4O_8$ in fields up to 7 T. *Physica C: Superconductivity*, 235:2955 2956, 1994.

[17] M Velez, JI Martin, JE Villegas, A Hoffmann, EM Gonzalez, JL Vicent, and Ivan K Schuller. Superconducting vortex pinning with artificial magnetic nanostructures. *Journal of Magnetism and Magnetic Materials*, 320(21):2547 2562, 2008.

[18] Ernst Helmut Brandt. The flux-line lattice in superconductors. *Reports on Progress in Physics*, 58(11):1465, 1995.

[19] D Cribier, B Jacrot, L Madhov Rao, and B Farnoux. Evidence from neutron diffraction for a periodic structure of the magnetic field in a niobium superconductor. *Phys. Lett*, 9:106 7, 1964.

[20] U Essman and H Trauble. Scientific American, March 1971. *H. Trauble, U. Essman, J. Appl. Phys*, 39:4052, 1968.

[21] H.W. Weber. Properties of the flux line lattice in hysteretic type-II superconductors. II. Neutron depolarization experiments. *Journal of Low Temperature Physics*, 17(1-2):49 63, 1974.

[22] EH Brandt and A Seeger. Muon-spin rotation as a tool for investigating the diffusion of positive muons in type-II superconductors. *Advances in Physics*, 35(2):189 236, 1986.

[23] H.F. Hess, R.B. Robinson, and J.V. Waszczak. Vortex-core structure observed with a scanning tunneling microscope. *Physical Review Letters*, 64(22):2711 2714, 1990.

[24] Tetsuya Hasegawa and Koichi Kitazawa. Atomically resolved STM/STS observation on the edge of CuO2 and (BiO)2 layers of Bi-Sr-Ca-Cu-O. *Japanese Journal of Applied Physics, Part 1: Regular Papers and Short Notes and Review Papers*, 29(3):434 437, 1990.

[25] H.J. Hug, A. Moser, I. Parashikov, B. Stiefel, O. Fritz, H.J. Gantherodt, and H. Thomas. Observation and manipulation of vortices in a YBa2Cu3O7 thin film with a low temperature magnetic force microscope. *Physica C: Superconductivity and its applications*, 235-240(PART 4):2695 2696, 1994.

[26] O.B. Hyun, J.R. Clem, and D.K. Finnemore. Motion of a single superconducting vortex. *Physical Review B*, 40(1):175 181, 1989.

[27] G.H. Kruithof, P.C. Van Son, and T.M. Klapwijk. Interaction between moving flux lines and a two-dimensional electron gas. *Physical Review Letters*, 67(19):2725 2728, 1991.

[28] S.J. Bending, K.V. Klitzing, and K. Ploog. Two-dimensional electron gas as a flux detector for a type-II superconducting film. *Physical Review B*, 42(16):9859 9864, 1990.

[29] J. Mannhart, J. Bosch, R. Gross, and R. P. Huebener. Two-dimensional imaging of trapped magnetic flux quanta in josephson tunnel junctions. *Phys. Rev. B*, 35:5267 5269, Apr 1987.

[30] K Harada, T Matsuda, H Kasai, JE Bonevich, T Yoshida, U Kawabe, and A Tonomura. Vortex configuration and dynamics in $Bi_2Sr_{1.8}CaCu_2O_x$ thin films by lorentz microscopy. *Physical review letters*, 71(20):3371 3374, 1993.

[31] H Kirchner. Improved faraday technique for observing magnetic structures in superconductors. *Physics Letters A*, 30(8):437 438, 1969.

[32] TH Johansen, M Baziljevich, H Bratsberg, Y Galperin, PE Lindelof, Y Shen, and P Vase. Direct observation of the current distribution in thin superconducting strips using magneto-optic imaging. *Physical Review B*, 54(22):16264, 1996.

[33] Ch Jooss, J Albrecht, H Kuhn, S Leonhardt, and H Kronmuller. Magneto-optical studies of current distributions in high-tc superconductors. *Reports on progress in Physics*, 65(5):651, 2002.

[34] Peter Brull, David Kirchgassner, and Paul Leiderer. Observation of symmetric patterns in the flux distribution of thin $YBa_2Cu_3O_{7-x}$ films. *Physica C: Superconductivity*, 182(4):339 344, 1991.

[35] Anna Palau Masoliver et al. *Critical currents and dissipation of grain boundary networks in coated conductors.* PhD thesis, 2005.

[36] M. Tinkham. *Introduction to Superconductivity: Second Edition.* Dover books on physics and chemistry. Dover Publications, 2004.

[37] G. Eilenberger. Transformation of Gorkov s equation for type-II superconductors into transport-like equations. *Zeitschrift für Physik*, 214(2):195 213, 1968.

[38] J. Friedel, P.G. De Gennes, and J. Matricon. Nature of the driving force in flux creep phenomena. *Applied Physics Letters*, 2(6):119 121, 1963.

[39] P. G. DE GENNES and J. MATRICON. Collective modes of vortex lines in superconductors of the second kind. *Rev. Mod. Phys.*, 36:45 49, Jan 1964.

[40] J. Pearl. Current distribution in superconducting films carrying quantized fluxoids. *Applied Physics Letters*, 5(4):65 66, 1964.

[41] C. Bean and J. Livingston. Surface Barrier in type-II Superconductors. *Physical Review Letters*, 12(1):14 16, jan 1964.

[42] E. Zeldov, A. Larkin, V. Geshkenbein, M. Konczykowski, D. Majer, B. Khaykovich, V. Vinokur, and H. Shtrikman. Geometrical Barriers in High-Temperature Superconductors. *Physical Review Letters*, 73(10):1428 1431, sep 1994.

[43] AI Buzdin. Multiple-quanta vortices at columnar defects. *Physical review. B, Condensed matter*, 47(17):11416 11419, 1993.

[44] A Yu Aladyshkin, AV Silhanek, Werner Gillijns, and VV Moshchalkov. Nucleation of superconductivity and vortex matter in superconductor ferromagnet hybrids. *Superconductor Science and Technology*, 22(5):053001, 2009.

[45] C. Bean. Magnetization of Hard Superconductors. *Physical Review Letters*, 8(6):250 253, mar 1962.

[46] Charles P. Bean. Magnetization of High-Field Superconductors. *Reviews of Modern Physics*, 36(1):31 39, jan 1964.

[47] PW Anderson. Theory of flux creep in hard superconductors. *Phys. Rev. Letters*, 9, 1962.

[48] Charles K Poole, Horacio A Farach, and Richard J Creswick. *Handbook of superconductivity.* Academic Press, 1999.

[49] Enric Pardo Vivé et al. Geometry effects on the electromagnetic properties of linear magnetic materials and superconductors in the critical state. 2004.

[50] D.-X. Chen and R. B. Goldfarb. Kim model for magnetization of type-II super-conductors. *Journal of Applied Physics*, 66(6):2489, sep 1989.

[51] Ernst Helmut Brandt and Grigorii P Mikitik. Meissner-london currents in super-conductors with rectangular cross section. *Physical review letters*, 85(19):4164 4167, 2000.

[52] A. Forkl and H. Kronmuller. Calculation of the magnetic flux density distribu-tion in type-II superconductors with finite thickness and well-defined geometry. *Physical Review B*, 52:16130 16139, Dec 1995.

[53] Thomas Schuster, Holger Kuhn, Ernst Helmut Brandt, Mikhail Indenbom, Michael R Koblischka, and Marcin Konczykowski. Flux motion in thin super-conductors with inhomogeneous pinning. *Physical Review B*, 50(22):16684, 1994.

[54] ST Stoddart, SJ Bending, AK Geim, and M Henini. Quantum-resolved investiga-tions of flux dynamics: Collective and single vortex effects. *Physical review letters*, 71(23):3854, 1993.

[55] PD Grant, MW Denhoff, W Xing, P Brown, S Govorkov, JC Irwin, B Heinrich, H Zhou, AA Fife, and AR Cragg. Determination of current and flux distribution in squares of thin-film high-temperature superconductors. *Physica C: Supercon-ductivity*, 229(3):289 300, 1994.

[56] W Xing, B Heinrich, Hu Zhou, AA Fife, and AR Cragg. Magnetic flux mapping, magnetization, and current distributions of $YBa_2Cu_3O_7$ thin films by scanning hall probe measurements. *Journal of applied physics*, 76(7):4244 4255, 1994.

[57] E. Zeldov, John Clem, M. McElfresh, and M. Darwin. Magnetization and transport currents in thin superconducting films. *Physical Review B*, 49(14):9802 9822, apr 1994.

[58] E.H. Brandt and M. Indenbom. Type-II-superconductor strip with current in a perpendicular magnetic field. *Physical Review B*, 48(17):12893 12906, 1993.

[59] D.Yu. Vodolazov and I.L. Maksimov. Distribution of the magnetic field and current density in superconducting films of finite thickness. *Physica C: Superconductivity and its Applications*, 349(1-2):125 138, 2001.

[60] B.L.T. Plourde, D.J. Van Harlingen, D.Yu. Vodolazov, R. Besseling, M.B.S. Hes-selberth, and P.H. Kes. Influence of edge barriers on vortex dynamics in thin weak-pinning superconducting strips. *Physical Review B - Condensed Matter and Materials Physics*, 64(1):145031 145036, 2001.

[61] John Clem and Alvaro Sanchez. Hysteretic ac losses and susceptibility of thin superconducting disks. *Physical Review B*, 50(13):9355 9362, oct 1994.

[62] A.A. Babaei Brojeny and J.R. Clem. Magnetic-field and current-density distributions in thin-film superconducting rings and disks. *Physical Review B - Condensed Matter and Materials Physics*, 68(17):1745141 1745149, 2003.

[63] V.G. Kogan, J.R. Clem, and R.G. Mints. Properties of mesoscopic superconducting thin-film rings: London approach. *Physical Review B - Condensed Matter and Materials Physics*, 69(6):645161 645169, 2004.

[64] Ernst Brandt and John Clem. Superconducting thin rings with finite penetration depth. *Physical Review B*, 69(18), may 2004.

[65] Y. Mawatari. Critical state of periodically arranged superconducting-strip lines in perpendicular fields. *Physical Review B*, 54(18):13215 13221, nov 1996.

[66] Ali A Babaei Brojeny, Yasunori Mawatari, M Benkraouda, and John R Clem. Magnetic fields and currents for two current-carrying parallel coplanar superconducting strips in a perpendicular magnetic field. *Superconductor Science and Technology*, 15(10):1454, 2002.

[67] John R. Clem and Ernst Helmut Brandt. Response of thin-film squids to applied fields and vortex fields: Linear squids. *Phys. Rev. B*, 72:174511, Nov 2005.

[68] Th. Schuster, H. Kuhn, and E. Brandt. Flux penetration into flat superconductors of arbitrary shape: Patterns of magnetic and electric fields and current. *Physical Review B*, 54(5):3514 3524, aug 1996.

[69] Ernst Brandt. Thin superconductors and SQUIDs in perpendicular magnetic field. *Physical Review B*, 72(2):024529, jul 2005. Note the different sign in $V(\mathbf{r}) = -\Phi_0 g(\mathbf{r})$.

[70] Yasunori Mawatari, Carles Navau, and Alvaro Sanchez. Two-dimensional arrays of superconducting strips as dc magnetic metamaterials. *Phys. Rev. B*, 85:134524, Apr 2012.

[71] V. Sokolovsky, L. Prigozhin, and V. Dikovsky. Meissner transport current in flat films of arbitrary shape and a magnetic trap for cold atoms. *Superconductor Science and Technology*, 23(6), 2010.

[72] H.L. Hortensius, E.F.C. Driessen, T.M. Klapwijk, K.K. Berggren, and J.R. Clem. Critical-current reduction in thin superconducting wires due to current crowding. *Applied Physics Letters*, 100(18), 2012.

[73] J.R. Clem and K.K. Berggren. Geometry-dependent critical currents in superconducting nanocircuits. *Physical Review B - Condensed Matter and Materials Physics*, 84(17), 2011.

[74] J.R. Clem, Y. Mawatari, G.R. Berdiyorov, and F.M. Peeters. Predicted field-dependent increase of critical currents in asymmetric superconducting nanocircuits. *Physical Review B - Condensed Matter and Materials Physics*, 85(14), 2012.

[75] C. Navau, N. Del-Valle, and A. Sanchez. Macroscopic modeling of magnetization and levitation of hard type-II superconductors: The critical-state model. *Applied Superconductivity, IEEE Transactions on*, 23(1):8201023 8201023, 2013.

[76] Ernst Brandt. Electric field in superconductors with rectangular cross section. *Physical Review B*, 52(21):15442 15457, dec 1995.

[77] D.-X. Chen, C. Navau, N. Del-Valle, and A. Sanchez. Perpendicular critical-state susceptibility of square superconducting films. *Applied Physics Letters*, 92(20):202503, 2008.

[78] Y. Kim, C. Hempstead, and A. Strnad. Critical Persistent Currents in Hard Superconductors. *Physical Review Letters*, 9(7):306 309, oct 1962.

[79] Y.B. Kim, C.F. Hempstead, and A.R. Strnad. Magnetization and critical supercurrents. *Physical Review*, 129(2):528 535, 1963.

[80] J. H. P. Watson. Magnetization of Synthetic Filamentary Superconductors. B. The Dependence of the Critical Current Density on Temperature and Magnetic Field. *Journal of Applied Physics*, 39(7):3406, june 1968.

[81] F. Irie and K. Yamafuji. Theory of flux motion in non-ideal type-II superconductors. *J. Phys. Soc. Jpn.*, 23:255, 1967.

[82] I. M. Green and P. Hlawiczka. Pinning forces and hysteresis in type ii superconductors. *Proc. IEE*, 114:1329, 1967.

[83] W. Fietz, M. Beasley, J. Silcox, and W. Webb. Magnetization of Superconducting Nb-25%Zr Wire. *Physical Review*, 136(2A):A335 A345, oct 1964.

[84] Ernst Brandt. Geometric barrier and current string in type-II superconductors obtained from continuum electrodynamics. *Physical Review B*, 59(5):3369 3372, feb 1999.

[85] Ernst Helmut Brandt. Susceptibility of superconductor disks and rings with and without flux creep. *Physical Review B*, 55(21):14513, 1997.

[86] Leonid Prigozhin. Solution of Thin Film Magnetization Problems in type-II Superconductivity. *Journal of Computational Physics*, 144(1):180 193, jul 1998.

[87] D.-X. Chen, A. Sanchez, and J.S. Munoz. Exponential critical-state model for magnetization of hard superconductors. *Journal of Applied Physics*, 67(7):3430 3437, 1990.

[88] X Granados, B Bozzo, S Iliescu, E Bartolomé, T Puig, X Obradors, J Amorós, and M Carrera. Critical current determination of artificially welded hts samples by in-field hall mapping technique. *Applied Superconductivity, IEEE Transactions on*, 15(2):3632 3635, 2005.

[89] John R Clem and Zhidong Hao. Theory for the hysteretic properties of the low-field dc magnetization in type-ii superconductors. *Physical Review B*, 48(18):13774, 1993.

[90] J Gilchrist. Critical state model: comparison of transverse and elongated geometries. *Physica C: Superconductivity*, 219(1):67 70, 1994.

[91] John R. Clem. Theory of ac losses in type-II superconductors with a field-dependent surface barrier. *Journal of Applied Physics*, 50(5):3518, may 1979.

[92] Du-Xing Chen and Alvaro Sanchez. Theoretical critical-state susceptibility spectra and their application to high-t c superconductors. *Journal of applied physics*, 70(10):5463 5477, 1991.

[93] Ernst Helmut Brandt. Superconductors of finite thickness in a perpendicular magnetic field: Strips and slabs. *Physical Review B*, 54:4246 4264, Aug 1996.

[94] John R Clem. Field and current distributions and ac losses in superconducting strips. *Physical Review B*, 80(18):184517, 2009.

[95] T Fukunaga, R Inada, and A Oota. Field-free core, current distribution, and alternating current losses in self fields for rectangular superconductor tapes. *Applied physics letters*, 72(25):3362 3364, 1998.

[96] Manfred Daumling. Ac power loss for superconducting strips of arbitrary thickness in the critical state carrying a transport current. *Superconductor Science and Technology*, 11(6):590, 1998.

[97] E Pardo, DX Chen, A Sanchez, and C Navau. Alternating current loss in rectangular superconducting bars with a constant critical-current density. *Superconductor Science and Technology*, 17(1):83, 2004.

[98] W T Norris. Calculation of hysteresis losses in hard superconductors carrying ac: isolated conductors and edges of thin sheets. *Journal of Physics D: Applied Physics*, 3(4):489 507, apr 1970.

[99] Ernst Brandt. Superconductor disks and cylinders in an axial magnetic field. I. Flux penetration and magnetization curves. *Physical Review B*, 58(10):6506 6522, sep 1998.

[100] Ernst Brandt. Superconductor disks and cylinders in an axial magnetic field: II. Nonlinear and linear ac susceptibilities. *Physical Review B*, 58(10):6523 6533, sep 1998.

[101] E. Bartolomé, X. Granados, A. Palau, T. Puig, X. Obradors, C. Navau, E. Pardo, A. Sánchez, and H. Claus. Magnetization and critical current of finite superconducting YBa2Cu3O7 rings. *Physical Review B*, 72(2):024523, jul.

[102] Ernst Brandt. Square and Rectangular Thin Superconductors in a Transverse Magnetic Field. *Physical Review Letters*, 74(15):3025 3028, apr 1995.

[103] Th. Schuster, M.V. Indenbom, M.R. Koblischka, H. Kuhn, and H. Kronmuller. Observation of current-discontinuity lines in type-II superconductors. *Physical Review B*, 49(5):3443 3452, 1994.

[104] J. I. Vestgården, D. V. Shantsev, Y. M. Galperin, and T. H. Johansen. Flux distribution in superconducting films with holes. *Phys. Rev. B*, 77:014521, Jan 2008.

[105] A Gurevich and EA Pashitskii. Current transport through low-angle grain boundaries in high-temperature superconductors (vol b57, pg 13878, 1998). *PHYSICAL REVIEW B*, 63(13), 2001.

[106] Jørn Inge Vestgården and Tom Henning Johansen. Modelling nonlocal electrodynamics in superconducting films: The case of a concave corner. *arXiv preprint arXiv:1205.0338*, 2012.

[107] John W Barrett, Leonid Prigozhin, and Vladimir Sokolovsky. Transport current and magnetization problems for thin type-II superconducting films. *arXiv preprint arXiv:1305.2101*, 2013.

[108] Alex D Semenov, Gregory N Goltsman, and Alexander A Korneev. Quantum detection by current carrying superconducting film. *Physica C: Superconductivity*, 351(4):349 356, 2001.

[109] M Ohkubo. Superconducting detectors for particles from atoms to proteins. *Physica C: Superconductivity*, 468(15):1987 1991, 2008.

[110] PL Richards. Bolometers for infrared and millimeter waves. *Journal of Applied Physics*, 76(1):1 24, 1994.

[111] J Jaycox and M Ketchen. Planar coupling scheme for ultra low noise dc SQUIDs. *Magnetics, IEEE Transactions on*, 17(1):400 403, 1981.

[112] Claudia D Tesche and John Clarke. DC SQUID: noise and optimization. *Journal of Low Temperature Physics*, 29(3-4):301 331, 1977.

[113] DD Awschalom, JR Rozen, MB Ketchen, WJ Gallagher, AW Kleinsasser, RL Sandstrom, and B Bumble. Low-noise modular microsusceptometer using nearly quantum limited dc squids. *Applied physics letters*, 53(21):2108 2110, 1988.

[114] BY Zhu, F Marchesoni, VV Moshchalkov, and Franco Nori. Controllable step motors and rectifiers of magnetic flux quanta using periodic arrays of asymmetric pinning defects. *Physical Review B*, 68(1):014514, 2003.

[115] JE Villegas, Sergey Savel ev, Franco Nori, EM Gonzalez, JV Anguita, R Garcia, and JL Vicent. A superconducting reversible rectifier that controls the motion of magnetic flux quanta. *Science*, 302(5648):1188 1191, 2003.

[116] Clécio C de Souza Silva, Joris Van de Vondel, Mathieu Morelle, and Victor V Moshchalkov. Controlled multiple reversals of a ratchet effect. *Nature*, 440(7084):651 654, 2006.

[117] Werner Gillijns, AV Silhanek, VV Moshchalkov, CJ Olson Reichhardt, and C Reichhardt. Origin of reversed vortex ratchet motion. *Physical review letters*, 99(24):247002, 2007.

[118] Valery Dikovsky, Vladimir Sokolovsky, Bo Zhang, Carsten Henkel, and Ron Folman. Superconducting atom chips: advantages and challenges. *The European Physical Journal D*, 51(2):247 259, 2009.

[119] O Romero-Isart, C Navau, A Sanchez, P Zoller, and JI Cirac. Superconducting vortex lattices for ultracold atoms. *arXiv preprint arXiv:1302.3504*, 2013.

[120] T Yamamoto, M Neeley, E Lucero, RC Bialczak, J Kelly, M Lenander, Matteo Mariantoni, AD OConnell, D Sank, H Wang, et al. Quantum process tomography of two-qubit controlled-Z and controlled-NOT gates using superconducting phase qubits. *Physical Review B*, 82(18):184515, 2010.

[121] CQ Wang, YF Yu, and ZM Zhang. Quantum gate operations in hybrid superconducting circuit. *The European Physical Journal D*, 66(11):1 6, 2012.

[122] Jiansong Gao, Jonas Zmuidzinas, Benjamin A Mazin, Henry G LeDuc, and Peter K Day. Noise properties of superconducting coplanar waveguide microwave resonators. *Applied Physics Letters*, 90(10):102507 102507, 2007.

[123] Hasan Padamsee. Accelerating applications of RF superconductivity-Success stories. *Applied Superconductivity, IEEE Transactions on*, 15(2):2432 2439, 2005.

[124] Carles Navau, Du-Xing Chen, Alvaro Sanchez, and Nuria Del-Valle. Magnetic properties of a dc metamaterial consisting of parallel square superconducting thin plates. *Applied Physics Letters*, 94(24):242501 242501, 2009.

[125] Yasunori Mawatari, Carles Navau, and Alvaro Sanchez. Two-dimensional arrays of superconducting strips as dc magnetic metamaterials. *Physical Review B*, 85(13):134524, 2012.

[126] Fedor Gomory, Mykola Solovyov, Ján Šouc, Carles Navau, Jordi Prat-Camps, and Alvaro Sanchez. Experimental realization of a magnetic cloak. *Science*, 335(6075):1466 1468, 2012.

[127] John R Hull. Applications of high-temperature superconductors in power technology. *Reports on Progress in Physics*, 66(11):1865, 2003.

[128] P Tixador, X Obradors, R Tournier, T Puig, D Bourgault, X Granados, JM Duval, E Mendoza, X Chaud, E Varesi, et al. Quench in bulk hts materials-application to the fault current limiter. *Superconductor Science and Technology*, 13(5):493, 2000.

[129] F Gomory, M Vojenčiak, E Pardo, M Solovyov, and J Šouc. Ac losses in coated conductors. *Superconductor Science and Technology*, 23(3):034012, 2010.

[130] Nuria del Valle Benedí. *Magnetic Levitation of Superconductors with Translational Symmetry*. PhD thesis, 2009.

[131] T. H. Johansen and H. Bratsberg. Critical-state magnetization of type-II superconductors in rectangular slab and cylinder geometries. *Journal of Applied Physics*, 77(8):3945, apr 1995.

[132] Leonid Prigozhin. The Bean Model in Superconductivity: Variational Formulation and Numerical Solution. *Journal of Computational Physics*, 129(1):190 200, nov 1996.

[133] Alvaro Sanchez and Carles Navau. Magnetic properties of finite superconducting cylinders. i. uniform applied field. *Phys. Rev. B*, 64:214506, Nov 2001.

[134] Alvaro Sanchez, Carles Navau, Nuria Del-Valle, Du-Xing Chen, and John R. Clem. Self-fields in thin superconducting tapes: Implications for the thickness effect in coated conductors. *Applied Physics Letters*, 96(7):072510, 2010.

[135] C. Navau, A. Sanchez, E. Pardo, D.-X. Chen, E. Bartolomé, X. Granados, T. Puig, and X. Obradors. Critical state in finite type-II superconducting rings. *Physical Review B*, 71(21):214507, june 2005.

[136] Nuria Del Valle, Alvaro Sanchez, Enric Pardo, Du-Xing Chen, and Carles Navau. Optimizing levitation force and stability in superconducting levitation with translational symmetry. *Applied Physics Letters*, 90(4):042503, jan 2007.

[137] C. Navau, A. Sanchez, N. Del-Valle, and D.-X. Chen. Alternating current susceptibility calculations for thin-film superconductors with regions of different critical-current densities. *Journal of Applied Physics*, 103(11):113907, june 2008.

[138] O-A Adami, D Cerbu, D Cabosart, M Motta, J Cuppens, WA Ortiz, VV Moshchalkov, B Hackens, R Delamare, J Van de Vondel, et al. Current

crowding effects in superconducting corner-shaped al microstrips. *Applied Physics Letters*, 102(5):052603 052603, 2013.

[139] X Obradors, T Puig, A Pomar, F Sandiumenge, S Pinol, N Mestres, O Castano, M Coll, A Cavallaro, A Palau, et al. Chemical solution deposition: a path towards low cost coated conductors. *Superconductor Science and Technology*, 17(8):1055, 2004.

[140] DX Chen. High-field ac susceptometer using Helmholtz coils as a magnetizer. *Measurement Science and Technology*, 15(6):1195, 2004.

[141] D-X Chen, G Via, C Navau, N Del-Valle, A Sanchez, S-S Wang, V Rouco, A Palau, and T Puig. Perpendicular ac susceptibility and critical current density of distant superconducting twin films. *Superconductor Science and Technology*, 24(7):075004, jul 2011.

[142] E. H Brandt, M. V Indenbom, and A Forkl. type-II Superconducting Strip in Perpendicular Magnetic Field. *Europhysics Letters (EPL)*, 22(9):735 740, june 1993.

[143] Th. Schuster, H. Kuhn, E. Brandt, M. Indenbom, M. Klaser, G. Muller-Vogt, H.-U. Habermeier, H. Kronmuller, and A. Forkl. Current and field pattern in rectangular and inhomogeneous superconductors. *Physical Review B*, 52(14):10375 10389, oct 1995.

[144] Guillem Via, Carles Navau, and Alvaro Sanchez. Magnetic and transport currents in thin film superconductors of arbitrary shape within the london approximation. *Journal of Applied Physics*, 113(9):093905, 2013.

[145] K-H Muller and DN Matthews. A model for the hysteretic critical current density in polycrystalline high-temperature superconductors. *Physica C: Superconductivity*, 206(3):275 284, 1993.

[146] MN Kunchur and TR Askew. Hysteretic internal fields and critical currents in polycrystalline superconductors. *Journal of applied physics*, 84(12):6763 6767, 1998.

[147] A Palau, T Puig, X Obradors, E Pardo, C Navau, A Sanchez, A Usoskin, HC Frey-hardt, L Fernandez, B Holzapfel, et al. Simultaneous inductive determination of grain and intergrain critical current densities of $YBa_2Cu_3O_{7-x}$ coated conductors. *Applied physics letters*, 84(2):230 232, 2004.

[148] D.-X. Chen, C. Navau, N. Del-Valle, and A. Sanchez. Analytic expressions for critical-state ac susceptibility of rectangular superconducting films in perpendicular magnetic field. *Physica C: Superconductivity*, 470(1):89  94, 2010.

[149] D-X Chen and E Pardo. Power-law $E(J)$ characteristic converted from field-amplitude and frequency dependent ac susceptibility in superconductors. *Applied physics letters*, 88(22):222505 222505, 2006.

1. Perpendicular ac susceptibility and critical current density of distant superconducting twin films
D.-X. Chen, G. Via, C. Navau, N. Del-Valle, A. Sanchez, S.-S. Wang, V. Rouco, A. Palau, and T. Puig
*Supercond. Sci. Technol.*, 24(7):075004, jul 2011.

2. Waiting time dependence of $T_2$ of protons in water suspensions of iron-oxide nanoparticles: Measurements and simulations
D.-X. Chen, G. Via, F.-J. Xu, C. Navau, A. Sanchez, H.-C. Gu, J.S. Andreu, C. Calero, J. Camacho and J. Faraudo
*J. Appl. Phys.*, 110(7):075004, 2011.

3. Magnetic and transport currents in thin film superconductors of arbitrary shape within the london approximation
G. Via, C. Navau, and A. Sanchez
*J. Appl. Phys.*, 113(9):093905, 2013.

4. Transport currents in thin film superconductors of arbitrary shape within the critical-state approximation
G. Via, A. Sanchez, N. Del-Valle and C. Navau
*In preparation*

5. Hysteretic Jc effects due to Stray fields generated in hybrid superconducting films with magnetic nanorods
V. Rouco, A. Palau, C. Monton, X. Obradors, R. Cordoba, J.M. De Teresa, G. Via, C. Navau, N. del Valle, A. Sánchez and T. Puig
*In preparation*